学位論文（要約）

A study of dynamical characteristics of inertia-gravity waves in the Antarctic mesosphere by combination of high-resolution observations and modeling

（高解像度観測と数値モデルを組み合わせた南極中間圏重力波の力学特性に関する研究）

平成 29 年度 8 月　博士（理学）申請

東京大学大学院 理学系研究科

地球惑星科学専攻

澁谷 亮輔

Abstract

Gravity waves are atmospheric waves with a restoring force of buoyancy that transport momentum upward from the troposphere to the middle atmosphere. Since horizontal wavelengths of a significant part of gravity waves are shorter than typical resolutions of the present climate models, many climate models utilize parameterization methods to calculate momentum deposition by the unresolved gravity waves. All of these gravity wave parameterizations are based on several simplifications and assumptions on dynamics of gravity wave characteristics. However, owing to complex nature of gravity waves, it is still challenging to represent the effects of gravity waves by parameterizations correctly. Therefore, observational constraints on dynamical characteristics of gravity waves to the parameterizations are inevitably required. Recent studies indicate that parameterized gravity waves in climate models are not realistic in the Antarctic. In response to such recognitions for the importance of gravity waves in the Antarctic, several observational campaigns to examine the gravity waves in the lower Antarctic stratosphere have been performed.

In the Antarctic, on the other hand, it is still challenging to perform observations of the mesosphere from the ground under its harsh environment. Although gravity-wave resolving models which cover the middle-atmosphere have been recently utilized to elucidate the dynamics of the mesospheric gravity waves, only a few studies focus on dynamical characteristic of the gravity waves in the Antarctic mesosphere.

The purpose of this study is to elucidate the dynamical characteristics such as wave parameters, propagation and generation mechanisms by utilizing two novel research tools. One is the first Mesosphere-Stratosphere-Troposphere/Incoherent Scattering (MST/IS)

radar in the Antarctic which was recently installed at Syowa Station (39.6°E, 69.0°S) as a project named “Program of the Antarctic SYowa MST/IS radar”. The PANSY radar is designed to observe three-dimensional winds at high time and vertical resolutions in the troposphere, stratosphere and mesosphere, which is the only observational instrument to capture both fine vertical and temporal structures of mesospheric disturbances including vertical wind. Furthermore, a Non-hydrostatic ICosahedral Atmospheric Model (NICAM) is also used to examine three dimensional structures of mesospheric disturbances. In this study, the top of the NICAM is extended to an altitude of 87 km with a vertical grid spacing in the middle atmosphere of about 400 m. This is the first non-hydrostatic simulation which tries to examine the mesospheric gravity waves with a high-vertical-resolution model, since currently most mesospheric gravity wave permitting models are the hydrostatic general circulation model. Moreover, the largest advantage of this study is that dynamical characteristics of gravity waves simulated by the NICAM can be validated by the high-resolution PANSY radar observation.

However, such a high-top and high-vertical-resolution setting requires a large computational burden. Thus, as a preparation of the mesospheric gravity wave permitting simulations, regionally enhanced and quasi-uniform meshes in the Antarctic by a transformation method with icosahedral grids are newly developed. The target region composed of fine meshes are connected to an outer region with coarse meshes transformed by the Schmidt transformation in order to maintain an isotropy of grid shapes. To realize these requirements, the characteristic lengths of the spring connecting grid nodes are analytically determined. It is shown that fine and quasi-uniform meshes in the target region are successfully generated using the new transformation.

The first observation by a complete system of the PANSY radar was performed from

March 16–24, 2015. Over this period, strong polar mesosphere winter echoes were detected, which likely resulted from a quite strong magnetic storm event. At heights of 70-80 km, large-amplitude disturbances are observed by the PANSY radar. Estimated vertical wavelengths, wave periods and vertical phase speeds of the disturbances are approximately 13.7 km, 12.3 h and −0.3 m s^{-1}, respectively. Previous studies suggested that disturbances with a period of 12 h in the mesosphere are mainly due to the semi-diurnal migrating tides or the semi-diurnal non-migrating tides. However, the wave parameters obtained in this study are quite different from those of the semi-diurnal tides.

To examine spatial structures and generation mechanisms of the wave disturbances, a model simulation using the Non-hydrostatic Icosahedral Atmospheric Model (NICAM) is performed in which the newly developed grid configuration in Chapter 2 is applied. The target region is a region south of 30°S centered at the South Pole with a horizontal resolution of 36 km. The vertical grid spacing is 400 m at heights from 2.4 km to 80 km with a 7 km thick sponge layer above 80 km.

The NICAM successfully simulates the large-amplitude disturbances and with a period of quasi 12 h, which is consistent with the observations. By using time and spatial filters, amplitudes of the diurnal and semi-diurnal migrating tides and small-scale gravity waves are examined in the simulated wind fields. The small-scale gravity waves are defined as components with horizontal wavelengths smaller than 1000 km, as frequently examined by previous studies. Their amplitudes are much smaller than observations, suggesting that dominant wave structures in the mesosphere are not due to the migrating tides nor the small-scale gravity waves. The remaining component has quite a similar structure and amplitudes to those by the observations. Wave parameters, such as vertical wavelengths and wave periods, simulated by the model agree well with those estimated

by the observations. Moreover, the parameters of the simulated waves are consistent with the dispersion relation of the linear inertia-gravity wave. These results indicate that the disturbances with a period of quasi 12 h observed by the PANSY radar are attributable to large-scale inertia-gravity waves.

The generation and propagation processes of wave packets simulated at Syowa Station are examined by a backward ray tracing. The first case is a wave packet which appears at 0600 UTC 21 March at Syowa Station at a height of 70 km and propagates from the location of (~100°E, ~40°S) at a height of 23 km for 48 hours. It seems that the wave packet is captured over the tropospheric jet core at 0600 UTC 19 March. Moreover, it is shown by examining a residual from the nonlinear balanced equation that the tropospheric jet is significantly imbalanced around the region. Thus, the wave packet is likely generated by the spontaneous radiation mechanism around the tropospheric jet. The second case is a wave packet which appears at 0000 UTC 19 March at Syowa Station at a height of 70 km and whose amplitude becomes significantly weak around a height of 55 km. This feature indicates an existence of a wave source at this height. A longitude-height cross-section of the wave packet shows symmetric features above and below the core of the polar night jet at a height of 55 km. The energy flux diverges from the core of the polar night jet, suggesting that the wave packet is generated around the core of the polar night jet. For the spontaneous radiation of the inertia-gravity waves around the polar night jet, a generation mechanism associated with the semi-diurnal migrating tides is newly proposed. As vertical winds associated with a semi-diurnal migrating tide at the height of the core of the polar night jet are adiabatically present along the modulated θ surface, quasi 12 h inertia-gravity waves with $s = 2$ can be radiated by the spontaneous radiation. In addition, because of the horizontal shear of the background wind including

the migrating tides, the deformation process can occur which causes the horizontal wavelength of the radiated quasi 12 h inertia-gravity waves shorter than that of the semi-diurnal migrating tide.

Furthermore, a long-term simulation using the high-top non-hydrostatic general circulation model is carried out to analyze mesospheric gravity waves in five months from April to August 2016 when continuous observations were made by the full system of the PANSY radar. Successive runs lasting 7 days are made with the initial condition from the MERRA reanalysis data with an overlap of two days between the two consecutive runs to maintain long-term simulations sufficiently close to the reanalysis data. Analyses are made for the last five days for each run. It is confirmed by comparing with the PANSY radar observation that mesospheric wind fields simulated by NICAM are realistic, although the amplitudes of the wind disturbances seem to be slightly larger than radar observations. The latitude-height structure of the zonally-averaged zonal winds is also comparable to the MERRA reanalysis data.

Next, the frequency spectra of zonal, meridional and vertical wind fluctuations and temperature fluctuations are obtained for the period from June to August 2016. The power spectra of zonal and meridional wind fluctuations obey a power law with an exponent of approximately -5/3 in higher frequency region than the inertial frequency f (corresponding to (2π/12.7 h)), while that of vertical wind fluctuations has a flat structure (i.e., $\propto \omega^0$) at frequencies from (2π/2 h) to (2π/5 days). The power spectrum of the meridional wind fluctuations without the migrating tides has an isolated peak around frequencies slightly lower than f at latitudes from 30°S to 75°S. On the other hand, there are isolated spectral peaks of meridional wind fluctuations at frequencies of about (2π/8 h) for 78°S to 90°S. Moreover, the frequency spectra of vertical fluxes of zonal and

meridional momentum (Re$[U(\omega)W^*(\omega)]$, Re$[V(\omega)W^*(\omega)]$) are obtained for the time period of JJA 2016 in the altitude region of 70-75 km by the zonal average (using 1280 time series data at each grid point). It seems that Re$[U(\omega)W^*(\omega)]$ is mainly negative in the examined frequency range and has an isolated peak at a frequency slightly lower than f. On the other hand, Re$[V(\omega)W^*(\omega)]$ is positive around the inertial frequency f, while that is negative at frequency regions lower than f. Assuming upward energy propagating gravity waves, this result suggests that disturbances with frequencies higher than f propagate equatorward, while those with frequencies lower than f propagate poleward.

Last, the spatial structures of the kinetic and potential energies, momentum and energy fluxes of gravity waves defined by components with frequencies higher than (2π/30 h) are examined. The distribution of the momentum fluxes in the lower stratosphere are consistent with those shown by previous studies. In the upper stratosphere and the mesosphere, large kinetic and potential energies are distributed along the axis of the polar night jet. The zonal components of the vertical momentum fluxes are mainly negative and have maxima slightly poleward of the axis of the polar night jet. This fact indicates that the gravity waves propagate westward relative to the mean wind. The meridional components of the vertical momentum fluxes are negative along and equatorward of the jet axis and positive or almost zero poleward of the jet axis, suggesting the propagation of the gravity wave into the regions slightly poleward of the axis of the polar night jet.

Previous studies suggested that disturbances with a period of quasi 12 h are due to the semi-diurnal migrating/non-migrating tides. This study shows the possibility that such disturbances are due to quasi-inertial-period gravity waves with horizontal wavelengths larger than 1000 km. By comparing the frequency spectra in NICAM to observations, it

is indicated that the statistical behaviors of the mesospheric disturbances simulated in NICAM are quite realistic in the high latitudes of the Southern Hemisphere. Moreover, it is shown that the quasi-inertial-period gravity waves have a large negative zonal momentum flux in the mesosphere.

For future studies, statistical analyses about parameters of the mesospheric gravity waves including intermittencies are interesting by combination of the PANSY radar observations and the high-top NICAM simulations. The origins of the spectral peaks around the quasi inertial frequency should be elucidated using the outputs by the high-top NICAM simulations. Further model development is needed for simulations for the period when the polar mesosphere summer echoes are detected by the PANSY radar for an altitude range of 80-95 km than the current available model top of NICAM. Such a very high top model can cover the whole mesosphere and provides invaluable data to understand momentum budgets in the Antarctic mesosphere where gravity waves are expected to play a significant role and affect the momentum and energy budgets in the themosphere/ionosphere by propagating further upward.

要旨

大気重力波は浮力を復元力とする波動であり、大気下層から上方へ熱や運動量を輸送する性質を持つ。現在の気候モデルにおいて重力波の運動量輸送の効果はパラメタリゼーションにより表現されているが、用いられる様々な強い単純化の仮定により観測される重力波の活動度分布を完璧に再現することは出来ていない。特に南極域中層大気においては観測とパラメタリゼーションとの乖離が大きく、この領域の重力波の力学特性を調べることは喫緊の課題である。しかし南極域中間圏は観測の難しさから、重力波の仔細なパラメータ解析や発生・伝播過程の研究は限定的である。一方これらの解析に有用であると思われる重力波を陽に解像する大気モデルもまだ数が少なく、南極域中間圏の重力波に注目した研究もほとんどない。

そこで、本研究は 2 つの最新の手法を用いた南極域中間圏重力波の力学特性の解明を目的とする。1 つは 2011 年に昭和基地に設置された大型大気レーダー（PANSY レーダー）である。PANSY レーダーは対流圏から中間圏までの 3 次元風速の鉛直プロファイルを高分解能かつ高精度で連続観測することができるため、従来調べることのできなかった中間圏擾乱の細かい鉛直構造を捉えることが可能である。もう 1 つは非静力学正二十面体モデル NICAM である。本研究では NICAM のモデルトップを中間圏まで拡張することで、PANSY レーダーで観測された波構造の再現実験を行う。これは世界初の非静力学モデルによる中層大気のシミュレーションである。そして再現実験のデータを PANSY レーダーの観測データと比較検証しつつ解析することで、南極域重力波の力学特性の解明を試みる。

本研究が目指す高い鉛直分解能かつモデルトップを中間圏に置く数値実験設定は、多くの鉛直層を用いるため計算コストが高くなる。一方、南極域のように特定領域に着目する際、計算コストを抑えるため水平格子を対象領域に集中させて高解像度化するストレッチ格子が有効である。しかし、既存のストレッチ格子は高解像度領域での格子間隔が連続的に変化する構造を持ち、重力波の運動

量フラックスの推定を行う際にその空間分布を歪ませる危険性がある。そこで本研究はまず、対象領域内で格子間隔が一様均一となるような格子構造を考案した。また対象領域外の格子間隔の分布に Schmidt 変換を適用することで、対象領域の広さと格子集中による解像度向上率についての解析的な条件を求めた。さらに、求めた格子間隔をばね法の自然長として用いることで、実際に極域一様等方格子を作成した。

2015 年 3 月 16 日から 24 日にかけて、PANSY レーダーのフルシステムによる観測が初めて行われた。この期間、顕著な太陽フレアイベントが発生し、これに関連すると思われる強い中間圏エコーが観測された。このデータを解析したところ、振幅が 30 m/s を超える顕著な波型擾乱が現れていたことが分かった。この擾乱の構造は鉛直波長が約 14 km、対地周期が約 12 h, 鉛直位相速度が下向きに約 0.3 m/s であった。従来、中間圏における周期約 12 時間の大振幅波動は半日太陽非同期潮汐によると考えられていた。しかしその振幅は約 10 m/s、鉛直波長は約 40 km と報告されており、PANSY レーダーで観測された波構造とは異なる。

これらの擾乱の力学特性を調べるため、この期間を対象とし、高度領域を中間圏まで拡張した NICAM による再現実験を行った。この際、新たに開発した水平格子構造を適用した。水平格子間隔は南緯 30 度以南で約 35 km である。またモデルトップは 87 km であり、鉛直方向の解像度は地表付近およびモデル上端 7km のスポンジ層を除いて 400 m で一定とした。

再現された中間圏の風の場には、観測とよく似た周期約 12 時間前後の大振幅擾乱が見られた。これらの擾乱の特性を調べるため、まず 1 日及び半日周期潮汐波、周期 42 時間以上の成分、ならびに東西・南北に 1000km 以下の水平波長を持つ擾乱を取り出し、その振幅と位相構造を調べた。これらの波の振幅は高々 10 m/s と弱く、大振幅擾乱はこれらの波によるものではないことがわかった。一方、これらの波を取り除いた残差成分は観測された擾乱とよく似た大きな振幅と位相構造を持っていた。そこで、昭和基地上の中間圏に現れた残差成分の 5 つの波束に着目し、波の各パラメータを位相構造から直接推定した。得られた鉛直

波長は約 13 km、対地周期は約 12 時間であり、観測データを用いた解析結果とよく似ていた。さらに、水平波長は約 1500 km から約 2500 km と推定され、これらは慣性重力波の分散関係式と調和的であった。故に、中間圏の大振幅擾乱は大スケールの慣性重力波であった可能性が高いと結論できる。

次に、再現実験において昭和基地付近に現れていた波束の伝播を後方追跡することにより、波の発生源を調べた。まず 3 月 21 日 06UTC に見られた波束は、約 48 時間かけて高度 23km の (100°E, 40°S)付近から伝播したことが分かった。この時、高度 23km 付近において波束は中緯度ジェットのコアに捕捉されたような位相構造を持っていた。また、波束の近傍において中緯度ジェットはバランスから大きくずれていた。以上の特徴は、この波が中緯度ジェットの自発的調節によって発生した可能性を示唆している。次に、3 月 19 日 00UTC に見られた波束の伝播を追跡したところ、高度 55km 付近で振幅が急激に弱くなっていた。この時刻の擾乱の経度高度断面を調べたところ、潮汐波によって作られた東西風速の極大値を中心に波の位相の傾きが変わる対称的な構造が見られた。またエネルギーフラックスは高度 55km 付近から発散していた。これらの特徴は、この波束が極渦付近で発生した可能性を示唆している。さらに、極渦付近における周期 12 時間の重力波の発生を説明する新たな自発的放射メカニズムを提案した。周期 12 時間の重力波は、太陽同期半日潮汐波による θ 面の歪みに伴う断熱的な鉛直運動から準共鳴によって生じる。発生した周期 12 時間かつ波数 2 の重力波は太陽同期一日潮汐波により形成された背景風の水平シアにより変形され、3 月 19 日 00UTC に見られたように波長が約 2500 km 程度まで短くなったと考えられる。

さらに、NICAM を用いて PANSY フルシステムによる連続観測が行われた 2016 年 4 月から 8 月の 5 ヶ月間を対象とした長期シミュレーションを行った。現実大気に十分近い場から外的強制力なしに発生する重力波を長期間解析するため、MERRA 再解析データを初期値として 7 日間のシミュレーションを複数行った。この時、次に行うシミュレーションの期間は前のシミュレーション期間と 2 日分重なるようにした。このように作成した複数のデータのうち、それぞれの

データの後半の 5 日間を繋げることで一連の連続的なデータを作成した。NICAM によって再現された中間圏の風速場を調べたところ、PANSY レーダーによる観測と比べて擾乱の振幅が約 1.5 倍ほど大きいものの、位相構造を良く再現していた。また平均東西風の緯度高度断面は MERRA 再解析データと整合的であった。

次に得られたモデルデータを用いて、東西、南北、鉛直風擾乱の周波数パワースペクトルを計算し、2016 年 6 月から 8 月において平均した。東西、南北風擾乱のスペクトルは周期 12 時間にピークを持ち、これより高周波数領域では周波数の約-5/3 乗に比例する構造を持っていた。また鉛直風擾乱のスペクトルは周期 2 時間から 5 日間の間でフラット（つまり周波数の 0 乗に比例）な構造を持っていた。さらに、南北風擾乱から 1 日及び半日太陽同期潮汐を除いた擾乱のスペクトルの緯度構造を調べたところ、南緯 30 度から 75 度にかけて慣性周期よりもやや長い周期にピークを持っていることが分かった。一方、南緯 78 度から 90 度においては、周期約 8 時間にピークが見られた。また、鉛直運動量フラックスの東西・南北成分のスペクトルを調べたところ、鉛直運動量フラックスの東西成分は慣性周期よりもやや長い周期に負のピークを持っていた。一方、鉛直運動量フラックスの南北成分は慣性周期よりも短い周期領域で正、長い周期領域で負の値を持つことが分かった。

最後に、30 時間未満の周期成分として定義した重力波の運動エネルギー、ポテンシャルエネルギー、運動量フラックス、エネルギーフラックスの空間構造を調べた。運動量フラックスやエネルギーフラックスの大きな値は、極夜ジェットの軸に沿うようにして分布していた。鉛直運動量フラックスの東西成分は主に負であり、極夜ジェットのやや極側で負の極大値を取ることが分かった。鉛直エネルギーフラックスが極夜ジェットの軸に沿って正であることから、重力波は平均風に向かって西に伝播していることが示唆された。さらに鉛直運動量フラックスの南北成分は極夜ジェットの中心と赤道側で負、極域側で正であり、重力波が極夜ジェットのやや極側に集中するように伝播していることが示唆された。

極域中間圏における周期 12 時間前後の大振幅擾乱は、今まで潮汐波としての

み議論されてきた。本研究はこの擾乱が 1000 km 以上の水平波長を持つ準慣性周期の慣性重力波である可能性があることを明らかにした。また先行研究による中間圏の高解像度観測データと比較し、NICAM は中間圏擾乱の統計的振る舞いを良く再現することが分かった。また、準慣性周期の慣性重力波は特に大きな負の運動量フラックスを持つことが明らかになった。

将来研究としてまず、PANSY レーダーによる観測データを用いた擾乱の詳細なパラメータ解析を行い、NICAM による結果との比較を行う必要がある。また中間圏で見られた慣性周期付近のエネルギーピークの起源について明らかにしたい。さらに、PANSY レーダーにより夏期に観測される高度 80 km から 95 km の擾乱について解析するため、モデルトップをさらに高く設定できるよう開発を行う必要がある。このような非常に高いモデルトップを持つ大気モデルは熱圏を含む全大気をカバーするため、熱圏や電離圏の運動量・エネルギー収支の更なる理解にとっても非常に重要なデータが得られることが期待される。

Contents

List of Figure captions

- Figure 1.5 : Map of the Antarctic stations providing the MF radar wind data used in Murphy et al. (2006). Adapted from Murphy et al. (2006).
- Figure 1.6 : Vertical winds on 5 February at 14:00 UT and 2.6 × 10−4 hPa (maximum value is 7.3 m s^{-1}) simulated by the mesoscale resolving WACCM. Adapted from Liu et al. (2014).

- Figure 2.1: The reduction ratio as a function of the edge latitude ϕ_0. The cross-marks denote the points at which the reduction ratios are 0.5 and 0.25, respectively. The circle denotes the point at $\phi_0 = 40° \pi/180°$.
- Figure 2.2: The scatter plots of the normalized grid interval defined as $d * 2^m$ (d denotes the grid interval and m denotes g-level) as a function of the latitude in the result of our transformation (green cross marks), the Schmidt transformation with $\beta \sim 5.42$ (black cross marks), the input characteristic length (black solid line), and the theoretical grid interval of the transformation by Tomita (2008) (black dashed curve). The g-level is 7 ($\sim 4^7 \times 10$ grid points). The black circle and dot-and-dashed line at $\phi_0 = 40°$ denote the connection point to the Schmidt transformation.
- Figure 2.3: The stretched icosahedral grid by (a) the transformation with $\beta \sim 5.42$ in Tomita (2008) (b) the present transformation. The horizontal map of the normalized grid interval (c) with the same grid as (a), and (d) with the same grid as (b), respectively. The g-level is 7 in (c) and (d), while it is degraded from g-level 7 to 4 in (a) and (b) for simplicity.
- Figure 2.4: The scatter plots of the (a) smoothness and (b) isotropy at all grids as a function of the latitude in the present transformation (green cross marks) and the

transformation in Tomita (2008) (black cross marks). The g-level is 7 ($\sim 4^7 \times 10$ grid points).

- Figure 2.5: snapshots of horizontal maps of vertical gradient of vertical wind components at z =15.0 km at (a) 1200 UTC 8 April 2013 using the grid systems generated (a) by Tomita (2008) and (b) by our transformation.
- Figure 2.6: a histogram of the ratio of the simulated momentum fluxes using the grid system by our transformation to those using the grid system by Tomita et al. (2008) ($\overline{u'w'}/\overline{u'w'}_{\mathrm{Tomita}}$) as a function of latitude. The scatter plot (black cross marks) shows the ratio of the grid intervals of Tomita et al. (2008) to of our transformation (d_{Tomita}/d), while the scatter plot (white cross marks) shows $(d_{\mathrm{Tomita}}/d)^2$.

- Figure 3.1: A time-height section of echo power observed by the vertical beam of the PANSY radar in the year of 2016. The red arrow denotes the period when the PANSY radar performed the observation with the complete system. Adapted from Tsutsumi et al. submitted to SOLA.
- Figure 3.2: Monthly mean of PMWE occurrence rates as a function of altitudes. Colors indicate different UT (0800, 1000, 1200, and 1400 UT) in May, 2015. (g) Monthly mean of electron density profiles (solid) with standard deviations (broken) based on Ionospheric Model for the Auroral Zone [*McKinnell and Friedrich*, 2007]. Adapted from Nishiyama et al. (2015).
- Figure 3.3: (a) An illustration of the stretched grid (roughened up to g-level 3). (b) A horizontal map of a normalized grid interval defined as $d/\Delta x$, where d

denotes grid intervals and Δx denotes the grid interval of the original icosahedral grid.

- Figure 3.4: Time-altitude cross sections of eastward line of sight velocity components observed by the PANSY radar at Syowa Station (a) for the period from 17 March 2015 to 23 March 2015, (b) for the period from 21 March 2015 to 23 March 2015, and (c) opposite of westward line of sight velocity components observed by the PANSY radar for the period from 21 March 2015 to 23 March 2015. The dashed line in (b) and (c) denotes phase lines with the downward phase velocity of 0.3 m s^{-1}. The green arrows in (c) denotes the wave period of the disturbance. The contour intervals are 2 m s^{-1}.
- Figure 3.5: Time-altitude cross sections of (a) zonal wind components and (b) meridional wind components observed by the PANSY radar at Syowa Station for the period from 21 March 2015 to 23 March 2015. The contour intervals are 12 m s^{-1}.
- Figure 3.6: Zonal and meridional wind components observed by the PANSY radar on 23 March 2015 as a function of time at heights of (a) 70.8 km and (b) 72.0 km. Zonal and meridional wind components fitted sinusoidal functions using a nonlinear least squares method at the height of (c) 70.8 km and (d) 72.0 km. The circles denote the zonal wind components and the star marks denote the meridional components.
- Figure 3.7: A hodograph of the fitted horizontal wind components in the time region from 00 UTC 23 to 13 UTC 23 March at the height of (a) 70.8 km and (b) 72.0 km from the PANSY radar observation. Each mark is plotted at one hour interval.

- Figure 3.8: Time-altitude cross sections of eastward line of sight velocity components simulated by NICAM at Syowa Station (a) for the period from 17 March 2015 to 23 March 2015 and (b) for the period from 21 March 2015 to 23 March 2015 (contour interval 3 m s^{-1}). (c) Zonal wind components in eastward line of sight velocity components simulated by NICAM for the period from 21 March 2015 to 23 March 2015 (contour interval 18 m s^{-1}).
- Figure 3.9: Time-altitude cross sections of (a) anomalies of the zonal wind components from the time-mean components, (b) the diurnal and semi-diurnal migrating tidal components, (c) the planetary wave components, (d) small-scale gravity waves and (e) the remaining components. The contour intervals are 10 m s^{-1}. The data is from the NICAM simulation.
- Figure 3.10: Time-altitude cross section of the envelope function of the zonal wind components of the large-scale gravity waves simulated by NICAM (contour interval 10 m s^{-1}) .The figure from (i) to (v) denote the labels of the wave packet examined in Section 4.
- Figure 3.11: Hovmöller diagram of zonal wind components of the large-scale inertia-gravity waves simulated by NICAM at the height of 70 km at 69°S (contour interval 10 m s^{-1}). The figures (i), (ii) and (v) indicate the packets labeled in Fig.5.
- Figure 3.12: Composite maps of zonal wind components of the large-scale inertia-gravity waves simulated by NICAM. The height where the composites are taken is (a) 70 km, (b) 70 km, (c) 75 km, (d) 65 km, and (e) 72 km. The longitudinal location is depicted as the relative longitude from Syowa Station. The contour intervals are 10 m s^{-1}.

- Figure 3.13: Snapshots of the zonal wind components and their envelope function of the large-scale inertia-gravity waves (a) at the height of 70 km at 03 UTC 23 March 2015, corresponding to the packet (v), and (c) at the height of 70 km at 01 UTC 19 March 2015, corresponding to the packet (i). Hovmöller diagrams of the zonal wind components and their envelope function of the large-scale inertia-gravity waves at the height of 70 km at 69°S for the period (b) from 20 to 23 March and (d) from 17 to 20 March. The green dashed curves in (a) and (c) denote the cross section taken in (b) and (d), and vice versa. The green circles are locations of traced wave packets by the method discussed in the text. The contour intervals are 10 m s^{-1}. The data is from the NICAM simulation.
- Figure 3.14: Snapshots of the zonal wind components of the large-scale inertia-gravity waves tracing the packet (v) (a) at the height of 60 km at 23 UTC 22 March (contour interval 10 m s^{-1}), (b) at the height of 40 km at 08 UTC 22 March (contour interval 5 m s^{-1}), (c) at the height of 25 km at 16 UTC 21 March (contour interval 3 m s^{-1}) and (d) at the height of 23 km at 03 UTC 21 March (contour interval 2 m s^{-1}). Snapshots for the packet (i) (e) at the height of 63 km at 23 UTC 22 March, (f) at the height of 58 km at 15 UTC 18 March, (g) at the height of 53 km at 11 UTC 18 March (contour interval 5 m s^{-1}), (d) at the height of 48 km at 08 UTC 18 March (contour interval 3 m s^{-1}). The green circles are locations of traced wave packets by the method discussed in the text. The data is from the NICAM simulation.
- Figure 3.15: The ray path of (a, b) the packet (v) simulated by NICAM and (c, d) the packet (i) using the idealized ray tracing method (black thick line, colored circles) and the manual wave packet tracing method (colored star marks) in (a, c)

the latitude-height cross section and (b, d) the horizontal map. The contours in (a, c) denotes background zonal wind components averaged in the zonal direction and for the period from 17 March to 23 March.

- Figure 3.16: A snapshots of longitude-height cross sections of zonal wind components of the large-scale inertia-gravity waves (above the height of 19 km, the left color bar, contour interval 2 m s^{-1}) and the absolute values of the horizontal wind components (below the height of 18 km, the right color bar, contour interval 10 m s^{-1}) at 03 UTC 21 March at 40°S. The data is from the NICAM simulation.
- Figure 3.17: Snapshots of horizontal maps of (a) the absolute horizontal wind velocity and (b) the residual of the nonlinear balance equation (ΔNBE) at the height of 10 km at 03 UTC 21 March 2015. The vectors in (a) denote the directions and the magnitude of the horizontal winds. The contour intervals in (a) are 10 m s^{-1}. The data is from the NICAM simulation.
- Figure 3.18: (a) A longitude-height cross section of zonal wind components of the large-scale inertia-gravity waves $\sqrt{\rho_0}u'$ at 65°S at 15 UTC 18 March (contour interval 0.1 $Pa^{0.5}$), and (b) a line plot of the energy flux $\overline{p'w'}$ averaged from the longitude of -90°E to the longitude of 60°E denoted by black arrows. The thick black contours show background zonal wind components extracted by a lowpass filter with a cutoff wavelength of 4000 km. The thick contours denote 20 m s^{-1}, 30 m s^{-1} and 40 m s^{-1}, respectively. The data is from the NICAM simulation.
- Figure 3.19: (a) a schematic figure of longitudinal locations of anomalies of θ ($\delta\theta$) from the zonal mean due to the semi-diurnal tide, and associated vertical wind couplets denoted by large arrows at a height of the core of the polar night jet. (b) A trajectory of fluid parcel on a θ surface at the height of polar night jet. The thin

dashed arrow denotes a motion of the fluid parcel, and U denotes the magnitude of the background zonal wind.

- Figure 3.20: Schematic illustration of spontaneous GW radiation from a localized jet stream caused by the mountain-wave-like mechanism proposed by McIntyre (2009). The blue arrows show the vertical flow composed of the slaved components. Doppler-shifted GWs are radiated because of the quasi resonance with the slaved components (i.e., the vertical flow couplets) when the space–time scales of the GWs are partially comparable to those of the slaved components. These vertical flow couplets are a compensation flow for the strong localized jet and are produced by the vortical flow over the deformed potential temperature surfaces, which are also the slaved components. These potential temperature surfaces act as mountains, such as ones that generate orographic GWs. Adapted from Yasuda et al. (2016).
- Figure 3.21: (a) A hovmöller diagram of potential temperature (shade) and the vertical wind components (contour) due to the diurnal and semi-diurnal migrating tides at the height of 55 km at 65°S. The contour interval is 0.5×10^{-2} m s^{-1}. (b) A hovmöller diagram of potential temperature (shade) and the vertical wind components (black contour) of the large-scale inertia gravity waves, and the zonal wind component with $s = 1$ and $s = 2$ at the height of 55 km at 65°S. The black contour interval is 2.0×10^{-2} m s^{-1}, the red thin contour denotes 30 m s^{-1} and the red thick contour denotes 35 m s^{-1}. The data is from the NICAM simulation.
- Figure 3.22: Latitude-height cross sections of (a) the vertical fluxes of zonal momentum $\rho_0\overline{u'w'}$, (b) the vertical fluxes of zonal momentum $\rho_0\overline{v'w'}$, (c) the ratio of the Coriolis parameter to the intrinsic frequency $f/\widehat{\omega}$, (d) the kinetic

energies of the horizontal wind components and (e) the potential energies of the large-scale inertia-gravity waves, which are averaged in the zonal direction and for the period from 19 March to 21 March 2015. The contour interval is (a, b) 4.0 $\times$ 10^{-5} [Pa] and (c) 0.1, respectively. It should be noted that the color bar and the contour interval in (d) and (e) are log-scaled. The data is from the NICAM simulation.

- Figure 4.1: An illustration for the time integration method.
- Figure 4.2: Time-altitude cross sections of northward line of sight speeds (a) observed by the PANSY radar at Syowa Station (a) for the period from 10 to 20 May 2015, and (b) those simulated by NICAM in the same period. The contour intervals are 4 m s^{-1}. The black dotted vertical lines in (b) denotes the segments of the lasting five-day-simulation.
- Figure 4.3: Time-altitude cross sections of zonal winds (a) from the MERRA reanalysis data and (b) from NICAM simulations for the period from May 10 to May 20 2015 at a grid near Syowa Station. The contour intervals are 20 m s^{-1}. The vertical dotted lines denotes the segments of the continuous five-day-simulation by NICAM. (a) The 3-D assimilated fields of the MERRA reanalysis data for 1000 hPa to 0.1 hPa and the 3-D analyzed fields for 0.1 hPa to 0.01 hPa are drawn.
- Figure 4.4: Latitude-altitude cross sections of the zonal mean zonal winds (a) from MERRA and (b) from NICAM simulations in May 2016. The contour intervals are 20 m s^{-1}.
- Figure 4.5: Frequency power spectra of (a) zonal, (b) meridional and (c) vertical wind, and (d) temperature fluctuations averaged for the height region of 70–75 km

for JJA in NICAM at a grid point near Syowa Station. Vertical black dotted line indicates frequencies corresponding to the one day and half day. Red dotted line indicates the inertia-frequency at Syowa Station (~2π/12.7 h at 69°S). Error bars show intervals of the 90% statistical significance.

- Figure 4.6: Frequency power spectra of meridional wind [$(P_v(\omega))$] in JJA as a function of height (a) at a grid point near Syowa Station and (b) averaged zonally at 69°S. (c) $P_v(\omega)$ without diurnal and semi-diurnal migrating tides and semi-diurnal non-migrating tides with $s = 1$ [$(\widetilde{P_v}(\omega))$] averaged zonally at 69°S. Vertical black dotted line indicates frequencies corresponding to the one day and half day, and the inertia-frequency at Syowa Station (~2π/12.7 h at 69°S).
- Figure 4.7: Zonal mean frequency power spectra of meridional wind fluctuations without diurnal and semi-diurnal migrating tides and semi-diurnal non-migrating tides with $s = 1$ $(\widetilde{P_v}(\omega))$ averaged in JJA as a function of latitude at heights of (a) 25 km, (b) 40 km, and (c) 70 km. (d) Frequency spectra of meridional wind fluctuations averaged in June and July with horizontal wavelengths longer than 1000 km without the migrating tides at 70 km. Vertical black dotted lines indicate frequencies corresponding to the one day period and half day. A black thin curves indicate the inertial frequencies at each latitude.
- Figure 4.8: Frequency power spectra of temperature fluctuations without diurnal and semi-diurnal migrating tides and semi-diurnal non-migrating tides with $s = 1$ $(\tilde{P}_{tem}(\omega))$ averaged in JJA as a function of latitudes at heights of 70 km. Vertical black dotted line indicates frequencies corresponding to the one day period and half day. A black thin curve indicate the inertial frequencies at each latitude. The shade and contour are drawn in a logarithm scale.Figure 4.9: Frequency power spectra of

(a) zonal and (b) meridional components for the vertical momentum fluxes averaged for the height region of 70–75 km for JJA in NICAM at a grid point near Syowa Station and those without diurnal and semi-diurnal migrating tides and semi-diurnal non-migrating tides with $s = 1$. Vertical black dotted line indicates frequencies corresponding to the one day and half day. Red dotted line indicates the inertia-frequency at Syowa Station (~2π/12.7 h at 69°S).

- Figure 4.10: horizontal maps of U, $\overline{KE}$, $\overline{PE}$, $\overline{u'w'}, \overline{v'w'}$ and $\overline{u'v'}$ at heights of 25 km, 55 km and 70 km averaged in JJA. The unit of U, $\overline{KE}$ and $\overline{PE}$, and $\overline{u'w'}, \overline{v'w'}$ and $\overline{u'v'}$ is m s^{-1}, J/kg and m^2s^{-2}, respectively.
- Figure 4.11: latitudinal structures of $\rho_0\overline{u'w'}, \rho_0\overline{v'w'}$, $\overline{p'v'}$, $\overline{p'w'}$ and U averaged in June and July. The unit of $\rho_0\overline{u'w'}, \rho_0\overline{v'w'}$, $\overline{p'v'}$and $\overline{p'w'}$, and U is Pa, W m^{-2} and, respectively. The contour values in $\overline{p'w'}$ are multiplied by 10^2. The black curves denote the location of the axis of the polar night jet.

List of Table captions

- Table 1: The wave parameters of fluctuations in the mesosphere observed over Syowa Station (a) obtained by fitting to a sinusoidal function using a nonlinear least square method (b) estimated on the hypothesis that fluctuations are due to inertia-gravity waves, where α is the angle of $u_{\parallel}$ measured clockwise from the east.
- Table 2: The directly estimated wave parameters of packets simulated over Syowa Station
- Table 3: The results of the idealized ray tracing and the manual wave packet tracing

Chapter 1

General Introduction

本章に使用している他者の著作物（図表等）についてインターネット公表に対する著作権者からの許諾が得られていないため、本章については、非公開。

Chapter 2

A new transformation method for a quasi-uniform and fine grid system in a circular region using the spring dynamics

In this chapter, a new transformation method for a regionally enhanced and quasi-uniform grid system in a circular region is proposed. The target region covered by finer meshes are connected to an outer region with coarser meshes transformed by the Schmidt transformation in order to maintain an isotropy of grid shapes. To realize these requirements, characteristic lengths of the spring connecting grid nodes are determined by a mathematical formula. It is numerically confirmed that fine and quasi-homogeneous meshes in the target region are certainly generated using this grid transformation. Note that the results in this chapter have already been published as a paper in *Journal of the Meteorological Society of Japan* (Shibuya et al., 2016).

2.1 A short review for the previous stretched grid systems

Recent development of computational facilities has allowed numerical simulations by atmospheric general circulation models with a sufficiently fine horizontal resolution to resolve non-hydrostatic scale motions. In such high-resolution models, discretization of the governing equations on a polyhedral grid system using grid-point methods tends to be popular to because of its high computational performance on parallel computers. An icosahedral grid is one of them (e.g., Williamson 1968; Sadourny et al., 1968; Heikes and

Randall 1995) and employed for the NICAM used in the present study. Detailed descriptions of the dynamical core and recent developments of NICAM are given by Tomita and Satoh (2004), Satoh et al. (2008) and Satoh et al. (2014). Recently, Miyakawa et al. (2014) showed that NICAM predicted the Madden-Julian Oscillation (MJO) using an initial condition about one month before. The icosahedral grids have been recognized to be useful based on such a demonstration by high-resolution simulations.

However, if a target region is not global but limited locally, globally fine horizontal meshes are not necessary for the numerical simulation. In such a case, taking grids with fine meshes for the target region only should be a better choice, which can lead to a significant reduction of the computational burdens. Most previous studies used regional or nesting models for this purpose. However, regional and nesting models can suffer from serious problems owing to the existence of artificial boundaries. Special technical treatments are required so as to reduce numerical errors or to damp artificial reflections of waves at the boundaries. Such problems can be avoided by using a stretched grid transformation developed by Tomita (2008). In his study a transformation function is constructed based on the Schmidt transformation function and applied it to the icosahedral grids. This transformation allows us to gather grid points in a local region of interest and realize higher resolution simulation there. Because the resolution changes smoothly away from the central point, no lateral boundary condition is required in its grid transformation, which is an obvious advantage of this approach. This type of smooth transition is useful, especially for case studies that require high resolution in a limited region for a period shorter than a week (Uchida et al., 2016). For example, the stretched grid was used to examine the prediction skill of MJO during the CINDY2011/DYNAMO observation period (Nasuno et al., 2013) and to simulate the dynamics of multiple tropopause events

and inertia-gravity waves in the Antarctic detected by radiosonde and the PANSY radar observations (Shibuya et al., 2015).

However, the stretched grid by Tomita (2008) has a problem for simulating phenomena whose expressions strongly depend on the horizontal resolution, because the Tomita's stretched grid is composed of non-uniform meshes even in the target region. This feature becomes apparent when the stretching parameter, which is defined later, is large. Plougonven et al. (2013) compared two simulations of inertia-gravity waves with different resolutions and reported that when the horizontal resolution is doubled, wave amplitudes become almost twice as large, although phase structures do not depend much on the resolution. Aghedo et al. (2010) shows that passive tracer transports simulated by the ECHAM5 general circulation model depend strongly on the horizontal and vertical resolutions. Because the horizontal resolution inherently determines the finest scale of filament observed around internal barrier regions such as the tropopause and the edge of the polar vortex, the mixing processes resolved in the numerical model have a strong dependence on the grid resolution. Thus, to examine physical processes such as waves, transports and mixing processes having fine structures, quasi-uniform and regionally fine meshes around the target region are desirable.

Iga (2015) proposed a smooth and seamless grid system with several topologies based on a conformal mapping technique. This grid system has a fine and uniform resolution inside the target region and is applicable to both the equatorial and polar regions. However, in order to generate a fine and uniform grid in a circular region following Iga's method, the grid shape should be a polyhedral one (not the icosahedral one). This means that the Iga's grid system can not be directly applied to the NICAM, since the dynamical core of the NICAM is based on the icosahedral grid system. Thus,

the purpose of the present study is to develop a grid system with fine and quasi-homogeneous resolution in the target region while maintaining the icosahedral grid structure. The fine mesh region is connected to an outside coarse mesh region transformed by the Schmidt transformation. This grid system is generated by the spring dynamics method (Tomita et al, 2002). However, contrary to Tomita et al. (2002), the characteristic length of the spring connecting grid nodes depends on the latitude of the grid node. Moreover, it is found that the finest possible resolution inside the target region is specified by an analytical function of the target region area through a constraint among the horizontal resolutions, the target region area and the total number of points in the mesh, as shown later.

2.2 A standard grid generation method in NICAM

2.2.1 Icosahedral grid on a sphere

Icosahedral grids over the sphere are generated by dividing the original icosahedron recursively. In NICAM, the grid resolution generated by the *m*-th dividing operation is conventionally referred to as the "g-level *m*" (grid division level *m*) grid (Tomita et al., 2002). G-level 0 is the original icosahedron. By dividing each triangle into four small triangles, a higher-level mesh is obtained. The total number of node points is $N = 10 \cdot 4^m + 2$ for g-level *m*. The effective resolution is estimated by the square root of the averaged control volume area, $\sqrt{4\pi {R_E}^2 / N}$, where R_{E} is the Earth's radius. Throughout the rest of the paper, the unit sphere is assumed. It should be noted that the grid can simply be scaled to whatever radius sphere is needed by the model.

2.2.2 Spring dynamics

In NICAM, grid intervals are regularized by the spring dynamics method and are re-modified by the gravitational-centered relocation (Tomita et al., 2002), which guarantees the second-order accuracy of numerical differential operators in NICAM (Tomita et al., 2001). It is assumed that each grid point has its own mass M and that neighboring grid points are connected by a spring with the spring coefficient k and the characteristic length f. A damping force proportional to the velocity of the grid motion is also added to ensure that the system calms down to a quasi-steady state after a sufficient number of iterations. The equation of the grid point motion is described as

$$M\frac{d\overrightarrow{w_0}}{dt} = \sum_{i=1}^{n} k(d_i - f)\vec{e}_i - \alpha\overrightarrow{w_0}, \text{ and}$$
$$\frac{d\overrightarrow{r_0}}{dt} = \overrightarrow{w_0}, \tag{2.1}$$

where d_i is the distance between the point P_0 and P_i where P_i is one of grid points surrounding P_0, $\vec{e}_i$ is the unit vector in the direction from P_0 to P_i projected on the tangential plane at P_0, $\overrightarrow{w_0}$ is the velocity vector at P_0, $\overrightarrow{r_0}$ is the position vector of P_0, n is the number of mass points surrounding P_0, and α is a damping coefficient. When the grid system reaches the equilibrium state, the following relation is satisfied:

$$\sum_{i=1}^{n}(d_i - f)\vec{e}_i = 0, \tag{2.2}$$

because $d\overrightarrow{w_0}/dt = 0$ and $\overrightarrow{w_0} = 0$.

An initial location of grid points before the iterations of the spring dynamics should be carefully prepared to avoid the collapse of grid shapes. One of the technical way to prepare the initial grid location is as follows: First, the grid transformation with a low g-level (2 or 3) is conducted with the initial condition of the original icosahedron. The grid

configuration in a higher g-level can be sequentially generated with the initial grid location of the same grid configuration with the lower g-level, by making a new grid point at the midpoint of the grid point in the lower g-level.

The grid structure in the equilibrium state depends only on a constant characteristic length f. In this study, a dependence on latitude ϕ is added to f, that is, $f(\phi)$, so as to enable the variable-resolution system. This also means that the spring dynamics is expected to force the distance between two grid points to be close to the latitude-dependent characteristic length $f(\phi)$. The specific form of the function $f(\phi)$ is discussed in Section 2.3.

2.3 How to determine the characteristic spring length

2.3.1 A constraint on the cell area and total grid number over the sphere

In the following, the target region is set to a region around the North Pole whose perimeter is along a latitude ϕ_0 for simplicity. The effective grid resolution in the target region, dx_T, which is defined as the square root of the cell area, is determined by the number of cells (n) in the target region, because the grid shapes are designed to be quasi-uniform. Thus dx_T is given by

$$dx_T = \sqrt{\frac{2\pi(1-\sin\phi_0)}{n}} \tag{3}$$

Hereafter, the latitude ϕ_0 is referred to as the edge latitude. As discussed in Section 2.2.1, the unit sphere is assumed.

Outside the target region, the resolution is determined by a latitude-dependent length scale $f(\phi)$, that is used by the spring dynamics method as a characteristic length scale of the spring. Assuming a regular hexagon, the area of the cell is equal to $\sqrt{3}/2\ (f(\phi))^2$.

Hereafter $f(\phi)$ is referred to as "the grid interval function". Note that $f(\phi)$ is an arbitrary function that takes positive values for $-\pi/2 \leq \phi \leq \pi/2$.

An obvious constraint on the cell areas over the sphere is that the integration of all cell areas is equal to the area of the sphere. This constraint can be written as follows:

$$\int_{0}^{2\pi} \int_{-\pi/2}^{\pi/2} \frac{\cos\phi}{A(\phi)} d\phi d\lambda = N$$

where λ is longitude, ϕ is latitude, N is the number of grid points over the sphere and $A(\phi)$ is the cell area around a grid point (λ, ϕ).

If the number of cells n is specified in the target region, the grid interval function, $f(\phi)$, outside the target region, must satisfy the following equation

$$2\pi \int_{-\pi/2}^{\phi_0} \frac{\cos\phi}{\frac{\sqrt{3}}{2}(f(\phi))^2} d\phi = N - n. \quad (4a)$$

Additionally, to enforce a smooth connection between the target region ($\phi_0 \leq \phi \leq \pi/2$) and the outer region ($-\pi/2 \leq \phi \leq \phi_0$), the resolution at ϕ_0 should be equal to dx_T. This condition is written as

$$\sqrt{\frac{2\pi(1-\sin\phi_0)}{n}} = \sqrt{\frac{\sqrt{3}}{2}} f(\phi_0) \quad (4b)$$

Although $f(\phi)$ is an arbitrary function that satisfies Eq. (4a) and (4b) at this point, it is obviously desirable if $f(\phi)$ is chosen so that the quasi-isotropy of a grid system can be realized. A form of such $f(\phi)$ will be given in the next section.

2.3.2. Connection with the Schmidt transformation

As verified by Tomita (2008), the transformation that can maintain the isotropy of the grid is identical to the Schmidt transformation. This isotropic transformation is

introduced by

$$\phi = \sin^{-1}\left[\frac{\beta(1+\sin\Phi)/(1-\sin\Phi)-1}{\beta(1+\sin\Phi)/(1-\sin\Phi)+1}\right], \tag{5}$$

where Φ is the latitude of the original point before the transformation, ϕ is the latitude after the transformation, and β is the stretching parameter that enables the smooth transition of the horizontal resolution. The latitudinal change of the latitude interval by the transformation, $d\phi/d\Phi$, is interpreted as the reduction factor of the grid interval, and the resolution after the transformation, $G(\Phi)$, is derived analytically as

$$G(\Phi) = dx\frac{d\phi}{d\Phi} = dx\frac{2\sqrt{\beta}}{(\beta+1)+(\beta-1)\sin\Phi} \tag{6}$$

where dx is the grid interval before the transformation. It should be noted that Eq. (6) indicates the resolution as a function of the original latitude Φ. For example, $G(\Phi)|_{\Phi=0}$ gives the resolution not at the equator, but at the latitude to which the equatorial line is transformed, i.e., $\sin^{-1}\left(\frac{\beta-1}{\beta+1}\right)$. The inverse of the Schmidt transform is given by

$$\begin{aligned}\Phi &= \sin^{-1}\left[\frac{-(\beta+1)\sin\phi+(\beta-1)}{(\beta-1)\sin\phi-(\beta+1)}\right] \\ &\equiv S^{-1}(\phi)\end{aligned} \tag{7}$$

Thus, the resolution is derived as a function of the transformed latitude ϕ using Eq. (7),

$$G(S^{-1}(\phi)) = dx\frac{(\beta+1)-(\beta-1)\sin\phi}{2\sqrt{\beta}}. \tag{8}$$

It is easily verified by substituting $\phi = \pi/2$ into Eq. (8) that the grid resolution is changed by a factor of $1/\sqrt{\beta}$ at the center of the transformation. When $\beta > 1$, the refinement for $\phi > 0$ in the Northern Hemisphere is obtained, while $0 < \beta < 1$ makes the refinement for $\phi < 0$ in the Southern Hemisphere.

The Schmidt transformation is used as the grid interval function to obtain an isotropic grid structure outside of the target region. The Schmidt transformation needs the

same number of grid points outside the target region, $(N-n)$. In the target region, however, the Schmidt transformation needs a larger number of grid points (n'), than the number of grid points (n) used in the new transformation. This is because the grid intervals obtained by the Schmidt transformation in the target region are smaller than the proposed transformation . Thus the original grid resolution used in the Schmidt transformation, $dX = \sqrt{4\pi/(n' + (N-n))}$, is different from the quasi-homogeneous grid interval of the new method, $dx = \sqrt{4\pi/(n + (N-n))}$. The grid interval function outside the target region is obtained as follows:

$$\sqrt{\frac{\sqrt{3}}{2}} f(\phi) = dX \frac{(\beta+1)-(\beta-1)\sin\phi}{2\sqrt{\beta}}, \quad -\pi/2 \le \phi \le \phi_0 \tag{9}$$

By combining Eq. (4b) and Eq. (9), dX is determined, and the grid interval function is obtained as follows:

$$f(\phi) = \begin{cases} \sqrt{\frac{2}{\sqrt{3}}}\sqrt{\frac{2\pi(1-\sin\phi_0)}{n}}, & \text{for } \phi_0 \le \phi \le \pi/2 \\ \sqrt{\frac{2}{\sqrt{3}}}\sqrt{\frac{2\pi(1-\sin\phi_0)}{n}}\frac{(\beta+1)-(\beta-1)\sin\phi}{(\beta+1)-(\beta-1)\sin\phi_0}, & \text{for } -\pi/2 \le \phi \le \phi_0 \end{cases} \tag{10}$$

Three parameters of the transformation, β, n, and ϕ_0 in Eq. (10) are related through the constraint about the grid system over the sphere, Eq. (4a).

2.3.3. The mathematical constraints on ϕ_0, n, and β

Using $f(\phi)$ as defined by Eq. (10) and Eq. (4a)**,** a single equation about three unknowns, ϕ_0, n and β can be derived:

$$n\frac{\left((\beta+1)-(\beta-1)\sin\phi_0\right)^2}{1-\sin\phi_0}\int_{-\pi/2}^{\phi_0}\frac{\cos\phi}{\left((\beta+1)-(\beta-1)\sin\phi\right)^2}d\phi \qquad (11)$$
$$= N - n$$

Equation (11) is transformed into a function of β and ϕ_0 that gives the number of cells $n(\phi_0,\beta)$ in the target region, which is the number of cells in the target region subject to the constraint that β be a positive real value:

$$n(\phi_0,\beta)$$
$$= N\left[\int_{-\pi/2}^{\phi_0}\frac{\left((\beta+1)-(\beta-1)\sin\phi_0\right)^2\cos\phi}{(1-\sin\phi_0)\left((\beta+1)-(\beta-1)\sin\phi\right)^2}d\phi+1\right]^{-1} \qquad (12)$$

For a fixed ϕ_0, $n(\phi_0,\beta)$ increases monotonically with increasing β. Using this fact, an upper bound on the number of cells in the target region is placed by taking a limit $\beta\to\infty$:

$$n_{\lim} = \lim_{\beta\to\infty} n(\phi_0,\beta) = \frac{2N}{3+\sin\phi_0} \qquad (13)$$

Thus, $n_{\lim}$ is an upper bound on n:

$$n < \frac{2N}{3+\sin\phi_0} = n_{\lim} \qquad (14)$$

This condition also indicates that the minimal resolution in the target region is also bounded by

$$dx_T = \sqrt{\frac{2\pi(1-\sin\phi_0)}{n}} > \sqrt{\frac{2\pi(1-\sin\phi_0)}{n_{\lim}}} \qquad (15)$$

Substituting the definition of n_{lim} from Eq. (14) into (15), Eq. (14) becomes

$$dx_T > \sqrt{\frac{4\pi}{N}}\sqrt{\frac{3-2\sin\phi_0-\sin^2\phi_0}{4}} = dx_{T\min} \qquad (15)$$

This inequality indicates that the minimal resolution $dx_{T\min}$ is proportional to the

original resolution $\sqrt{4\pi/N}$ multiplied by the reduction factor $\sqrt{(3-2\sin\phi_0-\sin^2\phi_0)/4}$. Figure 2.1 shows the reduction factor as a function of the edge latitude ϕ_0. The reduction factor is one for $\phi_0 = -\pi/2$ corresponding to the original grid shape, and is zero for $\phi_0 = \pi/2$ corresponding to the case where all grid points are located at the pole. When ϕ_0 is set to as $\sin^{-1}\left(-1+\sqrt{3}\right)$ (approximately 47º) or $\sin^{-1}\left(-1+\sqrt{15/4}\right)$ (approximately 69.5°), the reduction factor becomes 0.5 or 0.25, respectively. This corresponds to the increase by one or two g-levels in the target region.

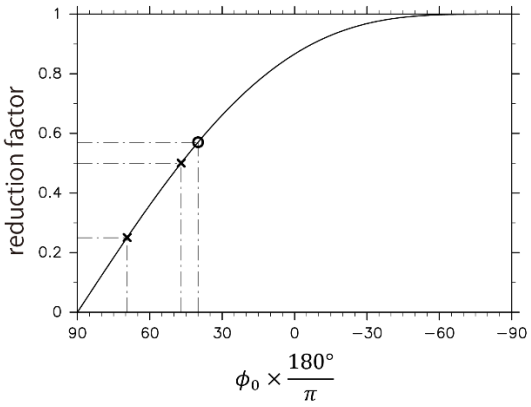

Figure 2.1:
The reduction ratio as a function of the edge latitude ϕ_0. The cross-marks denote the points at which the reduction ratios are 0.5 and 0.25, respectively. The circle denotes the point at $\phi_0 = 40° \pi/180°$.

For a given ϕ_0, a sufficiently large β is needed so that the number of the grid points in the target region n approaches n_{lim} (Eq. (13)). However, a typical β value where $dn/d\beta$ is close to zero, depends on the choice of ϕ_0 (not shown). Thus, in practice, it is better to choose the largest integer less than $0.99\, n_{\mathrm{lim}}$ as n, which gives $\sqrt{1/0.99}$ (~1.005) $dx_{T\,\mathrm{min}}$ in the target region. Last, after the dependent parameter β is solved numerically through Eq. (11), an ideal variable-resolution grid system is obtained using Eq. (10).

In summary, the quasi-homogeneous grid system in the target region is obtained

using only one parameter, ϕ_0 through Eq. (11) and (13), which is the edge latitude of the target region.

2.4. Results: Grid properties

The grid interval function given by Eq. (10) is used as the characteristic length in the spring dynamics described in Section 2.2.2. Hereafter, ϕ_0 is selected at 40°. In that case, $n = 0.99 \times n_{\mathrm{lim}} \sim 0.99 \times 0.55N$ and $\beta \sim 205.3$. In this section, the g-level of the grid system is taken to be 7 ($\sim 4^7 \times 10$ grid points).

The stretched grid transformed by the original method of Tomita (2008) is also generated with the same number of grid points in the target region and compared with the new method. The stretching parameter β in Tomita (2008) is approximately $\beta = 5.42$. After relocating the grid points near the North Pole using both transformations, all grids are rotated so that the center of the target region is located at the South Pole. This is because this study focuses on gravity waves in the Antarctic. Note that the transformation after the relocation to the South Pole corresponds to the Schmidt transformation with $\beta = 5.42^{-1}$.

2.4.1. Resolution

Figure 2.2 shows scatter plots of the normalized grid intervals, defined as $d * 2^m$ (d denotes the grid interval), for all grid cells as a function of the latitude. It is clear that the grid intervals of the new transformation (green cross marks) is quasi homogeneous compared with those of Tomita (2008) (black cross marks). The result of the new transformation accords well with the input characteristic length (Eq. (9)) (a thin black solid curve), although some discrepancies around pentagonal cells appear. This may be

partly explained by properties of the spring dynamics, which leads to smaller grid intervals around pentagons (see discussion in Tomita et al., 2002).

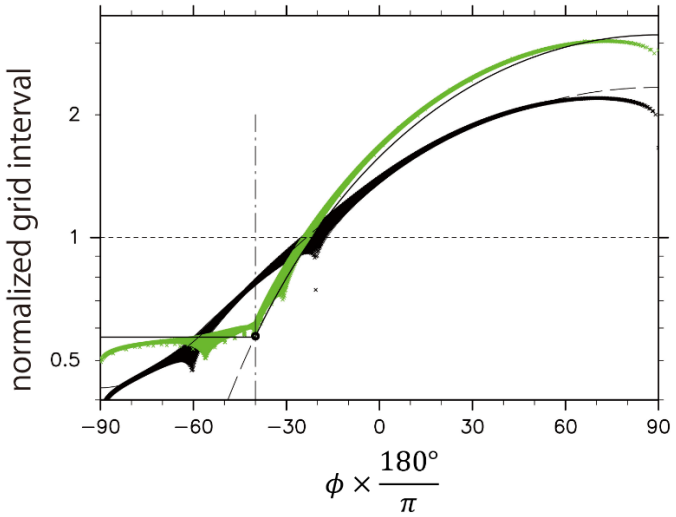

Figure 2.2: The scatter plots of the normalized grid interval defined as the grid interval $d * 2^7$ as a function of the latitude in the result of the new transformation (green cross marks), the Schmidt transformation with $\beta \sim 5.42$ (black cross marks), the input characteristic length (black solid line), and the theoretical grid interval of the Schmidt transformation (black dashed curve). The g-level is 7 ($\sim 4^7 \times 10$ grid points). The black circle and dot-and-dashed line at $\phi_0 = 40°$ denote the connection point to the Schmidt transformation.

Figure 2.3 shows the mesh structures and the horizontal maps of the normalized grid intervals. The grid intervals shown in Figs. 2.3c and 2.3d are averaged ones a particular point P_0 and adjacent points. Compared with the transformation by Tomita (2008), it is clear that the grid intervals of the new transformation in the target region are more homogeneous and coarse in the outer region. It should be noted that this feature is preferable to reduce the computational burden, since the new transformation does not require the model to use a small time step owing to a few small cells near the target center.

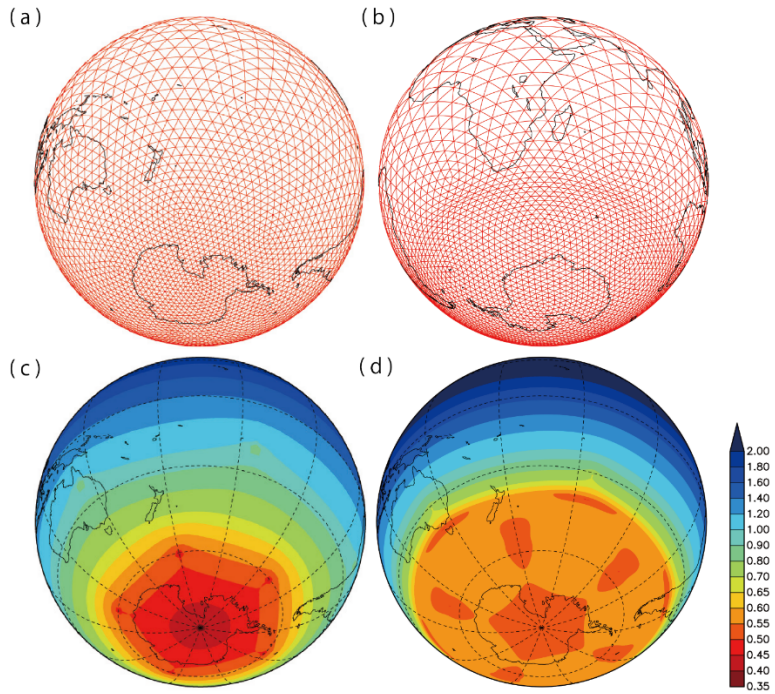

Figure 2.3: The stretched icosahedral grid by (a) the transformation with $\beta \sim 5.42$ in Tomita (2008) and by (b) the new transformation. The horizontal map of the normalized grid interval (c) for (a), and (d) for (b). The g-level is 7 in (c) and (d), while it is degraded from g-level 7 to 4 in (a) and (b) for easy visualization.

2.4.2. Smoothness and Isotropy

Next, the properties of the two grid systems are examined and compared in terms of the area uniformity and isotropy. The area uniformity is important to resolve such dynamical phenomena as waves and mixing processes, as discussed in Section 2.1. In this study, the area uniformity which is a measure of smoothness is defined locally by the variance of a grid area against the areas of surrounding grids:

$$S_0 = \frac{\sum_{i=1}^{N_s}(A_i - A_0)^2}{N_s {A_0}^2}$$

where A_0 is an area of a grid, A_i is that of a grid surrounding A_0, and N_s is the number of grids surrounding A_0. When the grid areas are completely uniform, the area uniformity S_0 is zero. It should be noted that S_0 is normalized by the square of its own

grid area because the variance of the area $\sum_{i=1}^{N_s}(A_i - A_0)^2$ depends on the grid area itself in the same configuration.

Figure 2.4a shows the area uniformity S_0 for the transformation by Tomita (2008) and that for the present transformation. It is clear that S_0 is lower (i.e., the smoothness is higher) in the target region for the new transformation than that by Tomita (2008), although it is possible outside the target region. The local maxima are observed at the pentagonal grids in both transformations.

The isotropy is also an important component for grid configuration because the break of the isotropy causes the dependence of minimal resolvable scales on axis directions (Miura and Kimoto 2005). Miura and Kimoto (2005) defined the isotropy of the icosahedral grid I_0 as

$$I_0 = \frac{\sum_{i=1}^{N_s}(l_i - l_0)^2}{N_s {l_0}^2},$$
$$l_0 = \frac{\sum_{i=1}^{N_s} l_i}{N_s}$$

where l_i is one edge length of a cell and l_0 is the average of edge lengths surrounding a grid. When the grid shapes are completely isotropic, the isotropy I_0 is zero. Since the transformation by Tomita (2008) is based on the Schmidt transformation, which is one of theoretical isotropic transformations, the isotropy of the meshes by Tomita (2008) is likely regarded as the reference of an isotropic transformation.

Figure 2.4b shows a scatter plot of the isotropy I_0 of the grid shapes for the two methods. The isotropy I_0 in the new transformation is maximized around the edge latitude $\phi_0 = -40°$, which is absent for the method by Tomita (2008). The distortion of the grid shape around the edge latitude can be also found in Figure 2.3b. As seen in Figure 2.4b, such distorted cells are located inside the target region with a width of about

$15°$ from the edge latitude. This fact suggests that the target region should be designed broader than the region of interest. At other latitudes, I_0 for the new transformation is about 3.0×10^{-3}, while I_0 corresponds to Tomita (2008)'s method is about 1.5×10^{-3}. Because $\sqrt{I_0}$ corresponds a ratio of a standard deviation of edge lengths of a cell to the mean edge length, a cell with $I_0 = 3.0 \times 10^{-3}$ (1.5×10^{-3}) has surrounding edge lengths with a standard deviation of about $5.5\ \%$ $(3.9\ \%)$ of the mean edge length. Thus the meshes by the new transformations are regarded as almost isotropic grid shapes, except near the edge latitude.

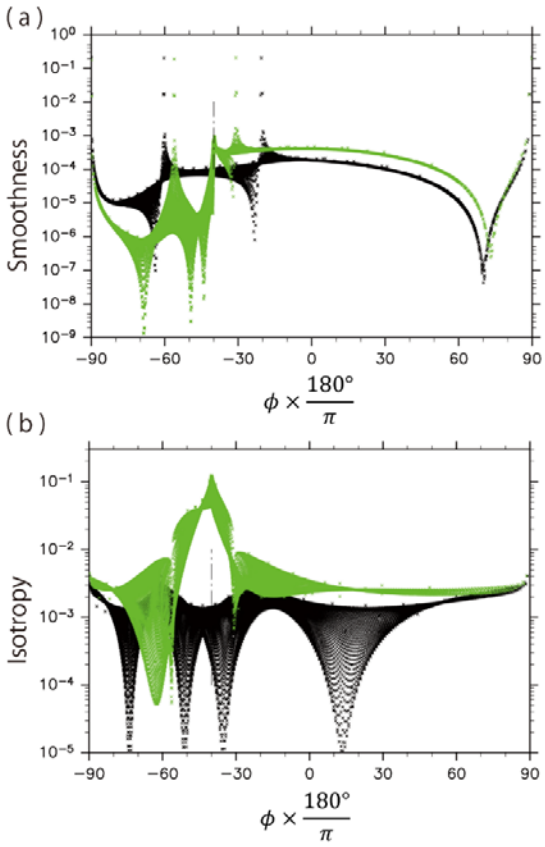

Figure 2.4:
The scatter plots of the (a) smoothness and (b) isotropy at all grids as a function of the latitude in the present transformation with $\phi_0 = -40°$ (green cross marks) and the transformation in Tomita (2008) (black cross marks). The g-level is 7 ($\sim 4^7 \times 10$ grid points).

2.4.3. Numerical simulation

In this subsection, a pairs of simulations are conducted for a realistic atmospheric condition using NICAM with the two grid systems shown in Figs. 2.3a and 2.3b. The

initial condition and model configuration are the same as Shibuya et al. (2015) except the horizontal grids: the model top is 53 km and the number of vertical levels is 243 ($\Delta z = 150$ m up to z = 20 km). Simulations were performed for a time period from 0000 UTC 7 April to 0000 UTC 9 April 2013. As discussed in Shibuya et al. (2015), gravity wave packets were observed both over the Antarctic continent and the Southern ocean during this period.

Figures 2.5a and 2.5b show snapshots of horizontal maps of $\partial w/\partial z$ (negative horizontal wind divergence) at z =15.0 km at 1200 UTC 8 April 2013 using the grid system by Tomita (2008) and that by the new transformation, respectively. Geographical locations and phase structures of gravity waves observed on the map are quite similar for the two simulations. Next, simulated momentum fluxes $\overline{u'w'}$ are calculated as a function of latitude for the period from 0000 UTC 8 April to 0000 UTC 9 April for more strict comparison. The gravity wave components denoted by primes are obtained are extracted by a high-pass filter with a cutoff wavelength of 1000 km, and $\overline{u'w'}$ are obtained.

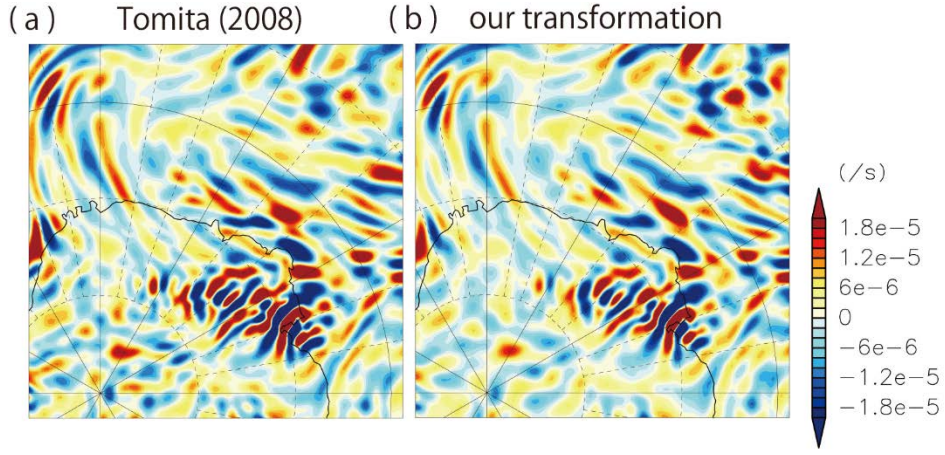

Figure 2.5: Snapshots of $\partial w/\partial z$ at z =15.0 km at (a) 1200 UTC 8 April 2013 using the grid systems generated (a) by Tomita (2008) and (b) by the new transformation.

Figure 2.6 shows a histogram of the ratio of the estimated momentum fluxes using the grid system by the new transformation $(\overline{u'w'})$ to those using the grid system by Tomita et al. (2008) $(\overline{u'w'}_{\mathrm{Tomita}})$ as a function of latitude. Black cross marks in Figure 2.6 denote the ratio of grid interval of Tomita (2008) (d_{Tomita}) to that of the new transformation (d). In the high-latitude region ($\phi < -60°$), $\overline{u'w'}_{\mathrm{Tomita}}$ is larger than $\overline{u'w'}$, while $\overline{u'w'}_{\mathrm{Tomita}}$ are smaller than $\overline{u'w'}$ in the mid-latitude region ($\phi > -60°$). Their features are consistent with the inverse ratio of the grid intervals (d_{Tomita}/d), as discussed in the previous studies (e.g., Plougonven et al., 2013). It should be noted that the center of the histogram of the ratio, $\overline{u'w'}/\overline{u'w'}_{\mathrm{Tomita}}$, approaches to unity at 60°S, where d_{Tomita} is equal to as d. Thus, $\overline{u'w'}_{\mathrm{Tomita}}$ tends to be over-(under-)estimated in the high-(mid-)latitude region as expected. This fact suggests that the new transformation gives meaningful spatial distribution of the momentum fluxes in the target region.

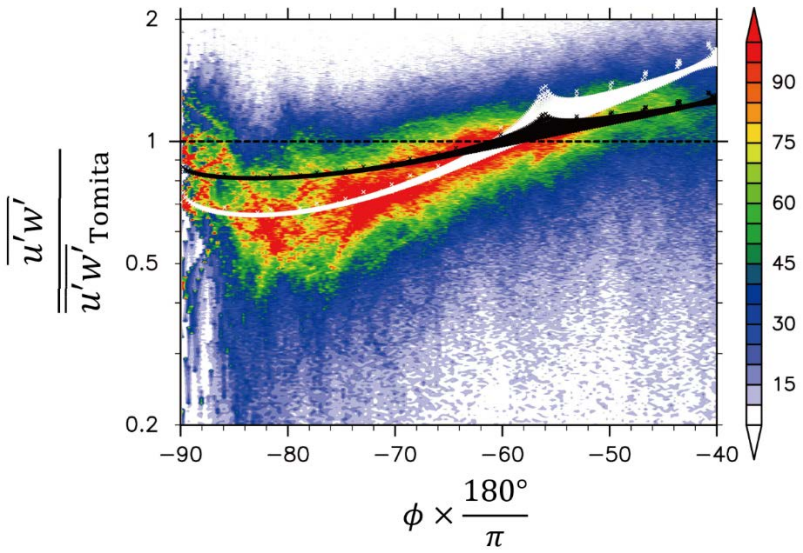

Figure 2.6: A histogram of the ratio of the simulated momentum fluxes using the grid system by the new transformation to those using the grid system by Tomita et al. (2008) $(\overline{u'w'}/\overline{u'w'}_{\mathrm{Tomita}})$ as a function of the latitude. Black cross marks denote the ratio of the grid intervals of Tomita et al. (2008) to those of the new transformation (d_{Tomita}/d), while White cross marks denote $(d_{\mathrm{Tomita}}/d)^2$.

Interestingly, the dependence of the momentum flux on the grid interval is much larger in the high-latitude region than in the mid-latitude region. The dependence at the high-latitude region is roughly described by $(d_{\mathrm{Tomita}}/d)^2$, which is more severe than reported by the previous studies (e.g. Plougonven et al., 2013). Further studies are needed to examine such quantitative dependence of the momentum flux on the grid interval.

2.5. Summary and concluding remarks

A new grid transformation with a fine and quasi-uniform grid system in a target region has been proposed for a reduction of the computational burdens. Unlike nesting models or regional models, the grid system by the new transformation does not have the problem of artificial wave reflection at the domain boundaries. Moreover, the quasi-uniform shape of the meshes in the target region is desirable for simulations of waves and mixing processes whose behaviors strongly depend on the model resolution. It should be noted that this transformation can be applied to other grid systems using the spring dynamics.

The Schmidt transformation is chosen as a latitudinal function of the resolution in the outer region so as to make the grid shapes as isotropic as possible. To realize this requirement, a constraint regarding the area of the target region, the number of grids in the target region, and the parameter of the Schmidt transformation is derived. As a result, it is shown that only one parameter that stands for the area of the target region need to be specified to determine the resolution function in the new transformation, provided that the condition that the grid resolution in the target region is as fine as possible.

By substituting the resolution function into the characteristic length in the spring

dynamics, the fine and quasi-homogeneous grids are successfully generated in the target region. Next, the obtained grid system is compared with that from the transformation in Tomita (2008). It is shown that the meshes by the new transformations are almost isotropic grid shapes, except near the edge latitude. Last, simulations using both transformation under a realistic atmospheric condition show the magnitudes of the momentum flux of gravity waves are strongly dependent on the grid intervals, suggesting that this transformation is quite useful for the study of spatial distributions of the momentum fluxes.

Chapter 3

Quasi-12 h inertia-gravity waves in the lower mesosphere observed by the PANSY radar at Syowa Station (39.6 °E, 69.0 °S)

In this chapter, data from the first observation by a complete system of the PANSY radar in March 16–24, 2015 are examined. During this observation period, strong wave-like wind disturbances propagating phases downward are observed in the mesosphere. The zonal wind amplitude is about 30 m s^{-1}. Observed vertical wavelengths and wave periods are 13 km and about 12 h, respectively. To explore dynamics of the wave disturbances, a model simulation is performed using a high-top NICAM employing the newly-developed stretched grid system described in Chapter 2. Strong wind disturbances with wave periods of 10–13 h in the mesosphere similar to the PANSY radar observations are successfully simulated. Based on the analysis using time and special filters, it is inferred that the wind disturbances in the mesosphere are not due to semi-diurnal tides, but due to inertia-gravity waves with horizontal wavelengths longer than 1000 km. Furthermore, the propagation and generation mechanisms of the inertia-gravity waves are discussed. Note that the results in this chapter have already been published as a paper in *Atmospheric Chemistry and Physics* (Shibuya et al., 2017).

3.1. A review for dominant mesospheric disturbances

Disturbances with a wave period of 12 h in the polar mesosphere have been examined by many previous studies (e.g., Murphy et al., 2006; Akmaev et al., 2016). There are several explanations for the existence of the disturbances with a period of 12 h.

past studies (e.g., Theon et al., 1967; Hook, 1970) and some resent studies (Fraser and Khan, 1990; Fisher et al., 2002) considered that these disturbances are attributable to semi-diurnal migrating tides. Waterscheid et al. (1986) and Collins et al. (1992) attributed these disturbances to a “pseudo-tide” related to gravity-wave momentum deposition modulated by the semi-diurnal migrating tide. Hagan and Forbes (2003) considered the atmospheric response to the zonally asymmetric latent heat release in the troposphere. Talaat and Mayr (2011) showed that internal oscillations may be caused by parameterized gravity waves in the model. Other studies (Hernandez et al., 1993; Forbes et al., 1995, 1999; Fritts et al, 1998; Portnyagin et al. 1998; Yamashita et al., 2002; Wu et al., 2003, Aso 2007, Murphy et al., 2009) suggested that these oscillations are due to semi-diurnal non-migrating tides with a zonal wavenumber s = 1 generated by nonlinear interactions between s = 1 stationary planetary waves and the semi-diurnal migrating tides. Mayr et al. (2005a, b) emphasized the importance of gravity wave filtering effects on the nonlinear interactions. Riggin et al. (1999) showed based on radar observations conducted at McMurdo (77.8^{o}S) and Halley (75.8^{o}S) that the zonal wavenumber of the 12 h waves is close to two in the winter and is one in the summer. Wu et al. (2002) suggested that s = 1 semi-diurnal non-migrating tides are significant at latitudes of higher than 78°S and that a mixture of semi-diurnal migrating tides and s = 1 semi-diurnal non-migrating tides appears in the latitude region between 68°S and 78°S.

Recently, the first observation with a complete system of the PANSY radar was performed for March 16–24, 2015. During the observation period, strong wave-like disturbances with a wave period of about 12 h were detected at heights of 70-80 km in the mesosphere. In Sections 3.3 and 3.4, dynamical characteristics of the wave-like disturbances such as wave parameters, generation and propagation mechanisms of such

disturbances were examined by using the PANSY radar data and the high-top NICAM.

3.2. Methodology

3.2.1. The PANSY radar observations

As described in Section 1.4, the PANSY (Program of the Antarctic Syowa) radar is the first MST/IS radar in the Antarctic that was installed at Syowa Station (39.6°E, 69.0°S). A pulse-modulated monostatic Doppler radar system is employed with an active phased array consisting of 1045 crossed-Yagi antennas. The PANSY radar observes backscatter echo from turbulence in the troposphere, stratosphere and mesosphere. Echoes detected by the PANSY radars result from coherent scattering owing to quite weak fluctuations in the refractive index at the Bragg scale (i.e., a half of wavelength of a launched radio wave) which is a few meters for the VHF band for monostatic radars like the PANSY radar. The scattering occurs owing to temperature and water vapor fluctuations by turbulence in the troposphere, by temperature fluctuations by turbulence in the lower stratosphere, and electron density fluctuations by turbulence in the mesosphere. The mesosphere echoes are sometimes enhanced by particle precipitation from the space. It should be noted that an observation gap exists in a height region from ~ 30 km to ~ 60 km, due to a shortage of backscatter in this height region (Sato et al., 2014).

The height region where the scattering occurs in the mesosphere depends on the season. Figure 3.1 shows a time-height section of echo powers observed by the vertical beam of the PANSY radar in the year of 2016. In the winter season, from the middle of March to the end of October, the echoes are detected at altitudes of about 60-80 km, while in the summer season, from the beginning of November to the end of February, the echoes

are detected at altitudes of about 80-100 km. The echoes in the winter (summer) seasons are called as the Polar Mesosphere Winter (Summer) Echo (or PMWE (PMSE) for short). A detailed mechanism of PMWE has not yet been well known (e.g., Zeller et al., 2006; Kirkwood, 2007), although that of PMSE is related to the polar mesospheric clouds appearing in the summer polar region (e.g., Rapp and Lübken, 2003; Rapp et al., 2008). Figure 3.2a shows that the occurrence rate of PMWE observed by the PANSY radar in May 2015 at each local time (Nishiyama et al., 2015). It is clear that the PMWEs are frequently observed only during daytime, likely because the mesosphere is sufficiently ionized by solar radiation and have the large electron density (Fig. 3.2b). Note that the largest occurrence rate is at most 20% at altitudes from 70 km to 80 km. Nevertheless, wind estimation is possible for the polar mesosphere with the aid of strong PMSE/PMWE particularly in daytime.

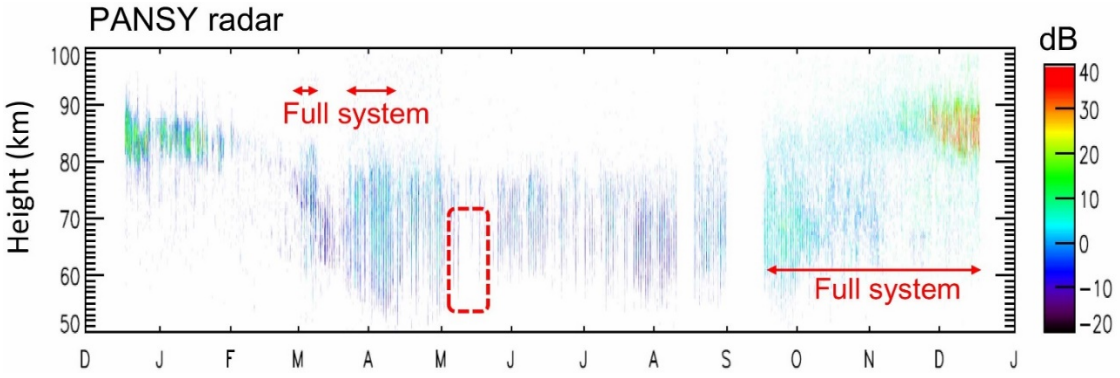

Figure 3.1: A time-height section of echo power observed by the vertical beam of the PANSY radar in the year of 2016. The red arrow denotes the period when the PANSY radar performed the observation with the complete system. Adapted from Tsutsumi et al. in press.

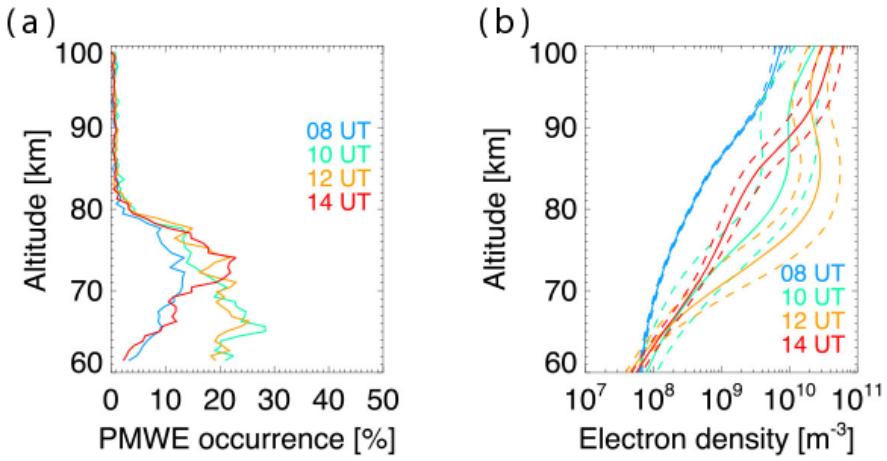

Figure 3.2: Monthly mean of PMWE occurrence rates as a function of altitudes. Colors indicate different UT (0800, 1000, 1200, and 1400 UT) in May, 2015. (g) Monthly mean of electron density profiles (solid) with standard deviations (broken) based on Ionospheric Model for the Auroral Zone (McKinnell and Friedrich, 2007). Adapted from Nishiyama et al. (2015).

Line-of-site wind speeds are estimated from the Doppler shift of the echoes by fitting the echo spectra into a Gaussian shape with a least squares method at a high time and vertical resolution of Δt = ~1 min and Δz = 150 m in the troposphere and lower stratosphere, and of Δt = ~1 min and Δz = 600 m in the mesosphere. The accuracy of line-of-sight winds is about 0.1 m s^{-1}. The PANSY radar data used in this study are line-of-sight winds for five beams pointing to the vertical and tilted east, west, north and south at a zenith angle of θ =10°. Vertical wind components are directly estimated from the vertical beam. Zonal (meridional) wind components are obtained using a pair of line-of-sight winds of the east and west beams (the north and south beams). For example, line-of-sight winds of the east and west beams, $V_{\pm\theta}$, are composed of zonal and vertical components of the wind velocity vectors $(u_{\pm\theta}, w_{\pm\theta})$ in the target volume ranges:

$$V_{\pm\theta} = \pm u_{\pm\theta} \sin\theta + w_{\pm\theta} \cos\theta. \quad (3.1)$$

By assuming that the wind field is homogeneous at each height, i.e., $u_{+\theta} = u_{-\theta} \equiv u$ and $w_{+\theta} = w_{-\theta} \equiv w$, zonal wind components are estimated as:

$$u = \frac{V_{+\theta} - V_{-\theta}}{2 \sin \theta}. \tag{3.2}$$

The vertical flux of zonal momentum is directly estimated from variances of line-of-sight wind fluctuations (Vincent and Reid, 1983):

$$\overline{V_{\pm\theta}'^2} = \overline{u_{\pm\theta}'^2} \sin^2 \theta + \overline{w_{\pm\theta}'^2} \cos^2 \theta \pm \overline{u_{\pm\theta}' w_{\pm\theta}'} \sin 2\theta \tag{3.3}$$

By assuming that the flux and variance fields are homogeneous ($\overline{u_{+\theta}'^2} = \overline{u_{-\theta}'^2} \equiv \overline{u'^2}$, $\overline{w_{+\theta}'^2} = \overline{w_{-\theta}'^2} \equiv \overline{w'^2}$ and $\overline{u_{+\theta}' w_{+\theta}'} = \overline{u_{-\theta}' w_{-\theta}'} \equiv \overline{u'w'}$), the vertical flux of zonal momentum $\overline{u'w'}$ is obtained:

$$\overline{u'w'} = \frac{\overline{V_{+\theta}'^2} - \overline{V_{-\theta}'^2}}{2 \sin 2\theta}. \tag{3.4}$$

This assumption is less strict than that used for the *u* and *w* estimation. Thus, the momentum flux estimation based on MST radars is quite accurate. The meridional wind component v and the vertical flux of meridional momentum $\overline{v'w'}$ can be estimated in a similar manner from a pair of line-of-sight winds of the north and south beams.

Continuous observations by the PANSY radar started with a partial system on April 30, 2012. The first observation with the complete system of the PANSY radar observation was performed for March 16–24, 2015. See Sato et al. (2014) for further details of the PANSY radar and for a list of future studies to be conducted based on this system. For the March 16–24, 2015 period, strong polar mesosphere winter echoes were observed by the PANSY radar. These echoes likely resulted from the largest magnetic storm event occurring during the solar cycle 24 (“St. Patrick’s day storm”, Kataoka et al., 2015; Jacobsen and Andalsvik 2016; Cherniak and Zakharenkova 2016). This means that a larger number of observational data in the mesosphere can be utilized in this period. In Section 3.3, wind disturbances observed in this time period are closely examined.

3.2.2. Numerical setup for NICAM

The simulation was performed using the Non-hydrostatic Icosahedral Atmospheric Model (NICAM), which is a global cloud resolving model (Satoh et al., 2008, Satoh et al., 2014). Numerical settings used in this study are described below.

3.2.2.1. Horizontal and vertical coordinate system

As shown in Chapter 2, resolutions of horizontal icosahedral grids are represented by g-level m (grid division level m). By dividing each triangle into four small triangles recursively, one-higher resolution is obtained. The total number of grid points is $N_{\mathrm{g}} = 10 \cdot 4^m + 2$ for g-level m. The actual resolution corresponds to the square root of the averaged control volume area, $\Delta x \equiv \sqrt{4\pi R_E^2 / N_g}$, where R_{E} is the Earth's radius. A g-level 7 grid is used in this study (Δx~ 56 km).

The grid configuration developed in Chapter 2 is used in Chapter 3. The target region for a given g-level is a region south of 30°S centered at the South Pole. Figure 3.3a shows an illustration of the stretched grid which is roughened up to g-level 3. Figure 3.3b shows a horizontal map of a normalized grid interval defined as $d(\lambda, \phi)/\Delta x$, where d denotes grid intervals as a function of the longitude, λ, and the latitude, ϕ. In this case, the horizontal resolution in the target region is roughly 36 km.

To simulate structures of disturbances from the troposphere to the mesosphere, the vertical grid spacing is set to 400 m at heights from 2.4 km to 80 km. It should be noted that, according to Watanabe et al. (2015), gravity wave momentum flux is not heavily dependent on model vertical spacing in the middle atmosphere when $\Delta z < 400$ m. The number of vertical grids is 217. To prevent unphysical wave reflections at the top of the

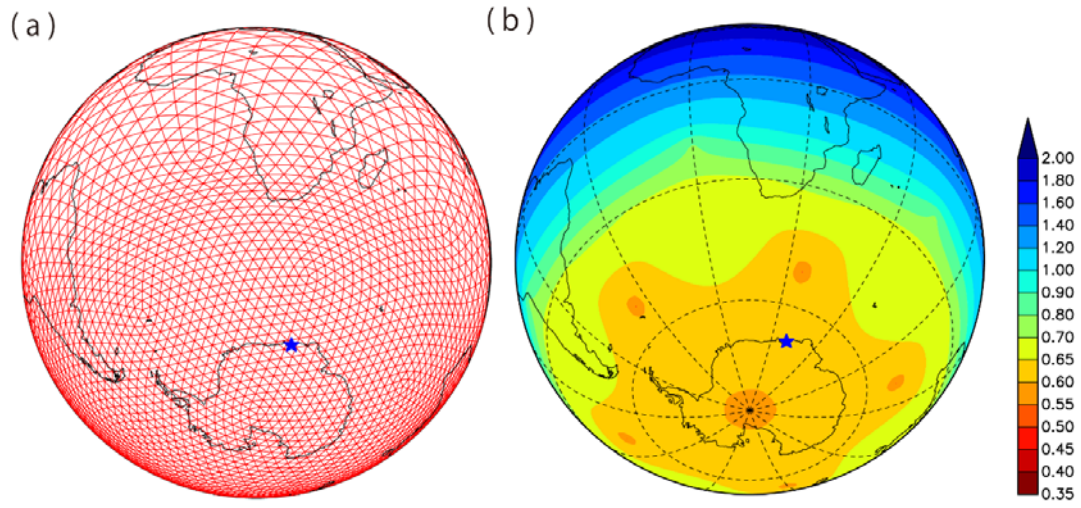

Figure 3.3: (a) An illustration of the stretched grid (roughened up to g-level 3). (b) A horizontal map of a normalized grid interval defined as $d/\Delta x$, where d denotes grid intervals and Δx denotes the grid interval of the original icosahedral grid.

boundary, a 7 km thick sponge layer is set above z = 80 km. The second-order Laplacian horizontal hyper-viscosity diffusion and Rayleigh damping for the vertical velocity are used for the sponge layer. An *e*-folding time of the ∇^2 horizontal diffusion for the $2\Delta x$ wave at the top of the model is 4 s, and an *e*-folding time of the Rayleigh damping for the vertical velocity for the top of the model is 216 s. The diffusivity level gradually increases from the bottom to the top of the sponge layer. It is confirmed that little wave reflection near the sponge layer occurs under this setting (not shown).

3.2.2.2. Initial condition and other physical schemes

MERRA reanalysis data based on the Goddard Earth Observing System Data Analysis System, Version 5 (GEOS-5 DAS; Rienecker et al. 2011) are used as the initial condition. In the MERRA reanalysis data, the following two types of 3-D fields are provided: one set is produced through the corrector segment of the Incremental Analysis Update (IAU, Bloom et al., 1996) cycle (1.25° × 1.25° and 42 vertical levels whose top is 0.1 hPa) and the other pertains to fields resulting from Gridpoint Statistical

Interpolation analyses (GSI analysis, e.g., Wu et al., 2002) on the native horizontal grid and on native model vertical levels (0.75° × 0.75° and 72 vertical levels whose top is 0.01 hPa). We use the former 3-D assimilated fields for 1000 hPa to 0.1 hPa and the latter 3-D analyzed fields for 0.1 hPa to 0.01 hPa for the initial condition of the NICAM simulation to prepare realistic atmospheric fields in the mesosphere for 0000 UTC on March 17, 2015. The latter 3-D analyzed fields are only used at above 0.1 hPa, as variables of vertical pressure velocity, cloud liquid water and ice mixing ratios are not included. Vertical pressure velocities, cloud liquid water and ice mixing ratios above 0.1 hPa are set to zero. The initial conditions for the land and ocean schemes are made from the NCEP FNL (Final) Operational Global Analysis in the Global Data Assimilation System (NCEP GDAS).

A time integration is performed until 0000 UTC on March 24. The time step is 15 seconds. As part of the boundary layer scheme, MYNN level 2 (Nakanishi and Niino, 2004) is used. No cumulous or gravity wave parameterization is employed. The model output is recorded every 1 hour. The sea surface temperature is nudged to NCEP GDAS in the simulation period. Note that this model does not use the nudging method as an external forcing for the atmospheric component.

3.3. Observational results

Figure 3.4a shows the time-height section of the line-of-sight wind speed observed by the east beam of the PANSY radar. In the lower stratosphere, wavy structures with short vertical wavelengths are clearly seen. Shibuya et al. (2015) showed that such a structure observed in May of 2013 by the PANSY radar at Syowa Station was due to inertia-gravity waves with a vertical wavelength of about 2 km. In the mesosphere, strong echoes (PMWE) were detected in a height region of 60-80 km over this time period. These

PMWEs were likely initiated by increased ionization during the largest magnetic storm event occurring on March 17-18, 2015 (Kataoka et al. 2015; Jacobsen and Andalsvik 2016; Cherniak and Zakharenkova 2016). In this period, the polar night jet was in the phase of formation over Syowa Station near the stratopause (at the height of about 55 km, not shown). As shown in Figure 3.4a, strong wave-like disturbances were observed in the mesosphere. Figures 3.4b and 3.4c, respectively show line-of-sight wind speeds of the east and west beams at heights of 65 - 80 km for 00 UTC on March 21 to 00 UTC on March 24. In Figures 3.4b and 3.4c, it is clear that phases of dominant disturbances propagate downward; a vertical phase speed (broken line) and an observed period (a green

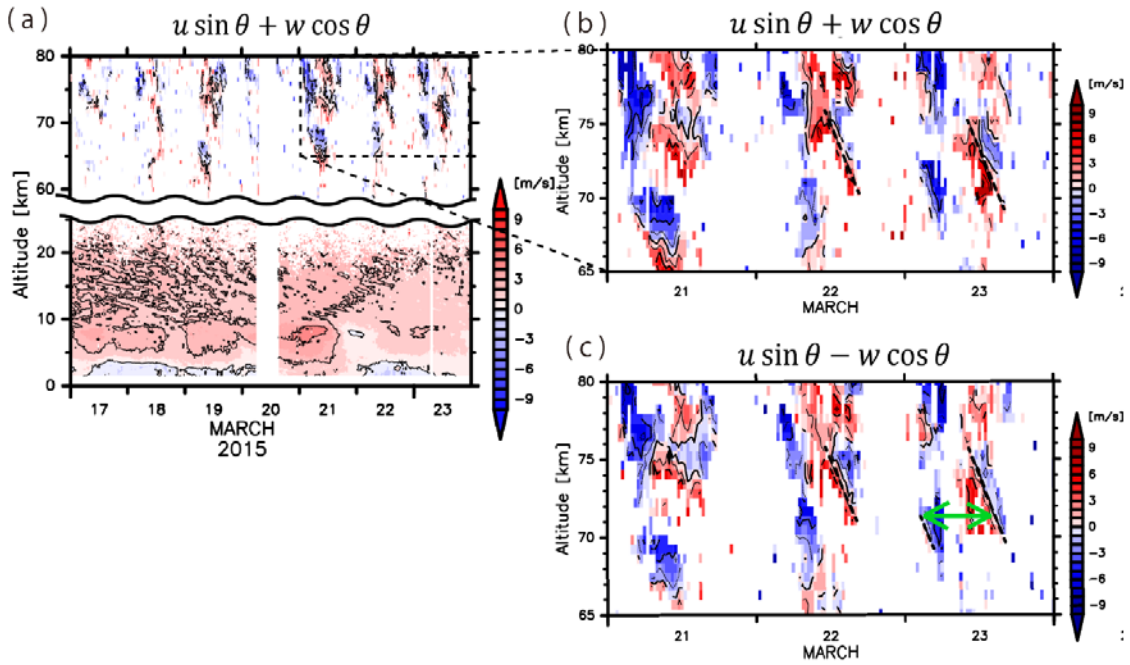

Figure 3.4: Time-altitude cross sections of eastward line of sight velocity components observed by the PANSY radar at Syowa Station (a) for the period from March 17 2015 to March 23 2015, (b) for the period from March 21 2015 to March 23 2015, and (c) opposite of westward line of sight velocity components observed by the PANSY radar for the period from March 21 2015 to March 23 2015. The dashed line in (b) and (c) denotes phase lines with the downward phase velocity of 0.3 m s^{-1}. The green arrows in (c) denotes the wave period of the disturbance. The contour intervals are 2 m s^{-1}.

arrow) are about −0.3 m s^{-1} and 12.3 h, respectively, indicating that the vertical wavelength is ~ 13.8 km.

As the zenith angle of tilted beams of the PANSY radar is θ =10°, locations of the observation points by the symmetric beams around the zenith in the mesosphere are separated by approximately 25 km at a height of 70 km. Figures 3.5a and 3.5b show time-height sections of estimated zonal and meridional wind components by the dual beam method (Eq. (3.2)). Clear phase lines with downward phase velocities are also observed at heights around 70 km. To examine wave parameters of the dominant disturbance, zonal (u') and meridional (v') wind fluctuations were fitted to sinusoidal functions at heights of 73.2 km, 73.8 km and 74.4 km for March 22 and at heights of 70.8 km, 71.4 km and 72.0 km for March 23 as follows:

$$\begin{aligned} u' &= \hat{u}\sin(\omega t + \theta_u) + u_\mathrm{o} \\ v' &= \hat{v}\sin(\omega t + \theta_v) + v_\mathrm{o}, \end{aligned} \tag{3.5}$$

where $\hat{u}$ and $\hat{v}$ are the amplitudes of u' and v', respectively, ω is the observed wave frequency, t is time, θ_u and θ_v are phases for u' and v', and u_o and v_o are offsets for u' and v', respectively. Parameters ($\hat{u}$, $\hat{v}$, ω, θ_u, θ_v, u_o and v_o) are determined using a nonlinear least square method so that the residual $\sqrt{(u'_\mathrm{obs} - u')^2 + (v'_\mathrm{obs} - u')^2}$ is smallest. Figure 3.6 shows a time series of observed u' and v' and results of the fitting at 70.8 km and 72.0 km for March 23. It is confirmed that the observed wind fluctuations have a sinusoidal form with a period of about 12 h, and the fitting was successfully performed. Moreover, it is seen that phases for u' and v' at 72.0 km are advanced compared to those at 70.8 km. This means that the vertical wavenumber is negative both for u' and v'. Using these phase differences, vertical wavenumbers for u' and v' are estimated, respectively. Table 1a summarizes parameters such as wave frequencies, vertical

wavenumbers and vertical phase speeds estimated from u' and v'. The estimated period ranges from 11.0 h to 13.8 h, which is close to 12 h. The estimated vertical wavelengths are 12.0 km and 8.5 km for u' and v' for March 22 and are 15.4 km and 12.3 km for u' and v' for March 23, respectively. Thus, the vertical phase speeds are −0.26 m s^{-1} and −0.19 m s^{-1} for u' and v' for March 22 and −0.35 m s^{-1} and −0.28 m s^{-1} for u' and v' for March 23, respectively. Although the estimates based on v' for March 22 are slightly different, the vertical phase speeds and observed periods agree well with the rough estimation denoted by broken lines and the green arrow in Figs. 3.4b and 3.4c, respectively (approximately −0.3 m s^{-1} and 12.3 h). Moreover, the amplitudes of the wave disturbances are larger than 30 m s^{-1} (summarized in Table 1b).

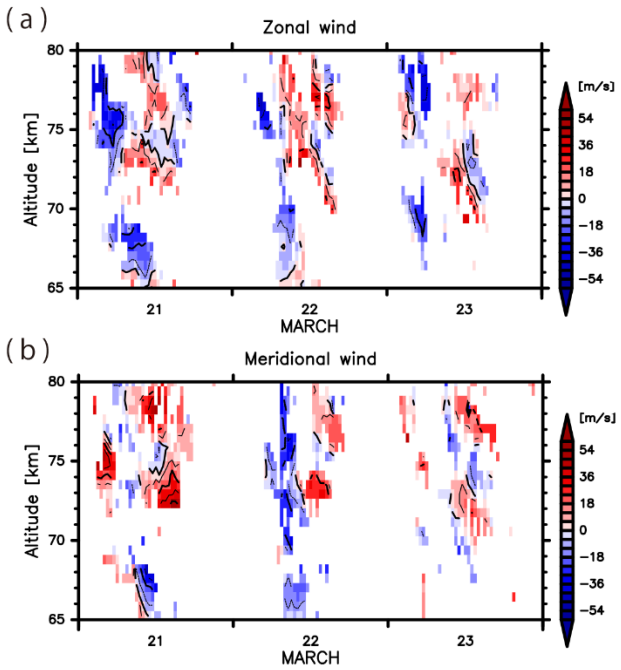

Figure 3.5:
Time-altitude cross sections of (a) zonal wind component and (b) meridional wind component observed by the PANSY radar at Syowa Station for the time period from March 21, 2015 to March 23, 2015. The contour intervals are 12 m s^{-1}.

As described in Section 3.1, previous studies suggested that quasi 12 h disturbances observed in the mesosphere are mainly due to the semi-diurnal migrating tides or the semi-diurnal non-migrating tides. According to Murphy et al. (2006), who examined a climatology of tides in the Antarctic mesosphere using MF radars, the amplitude and

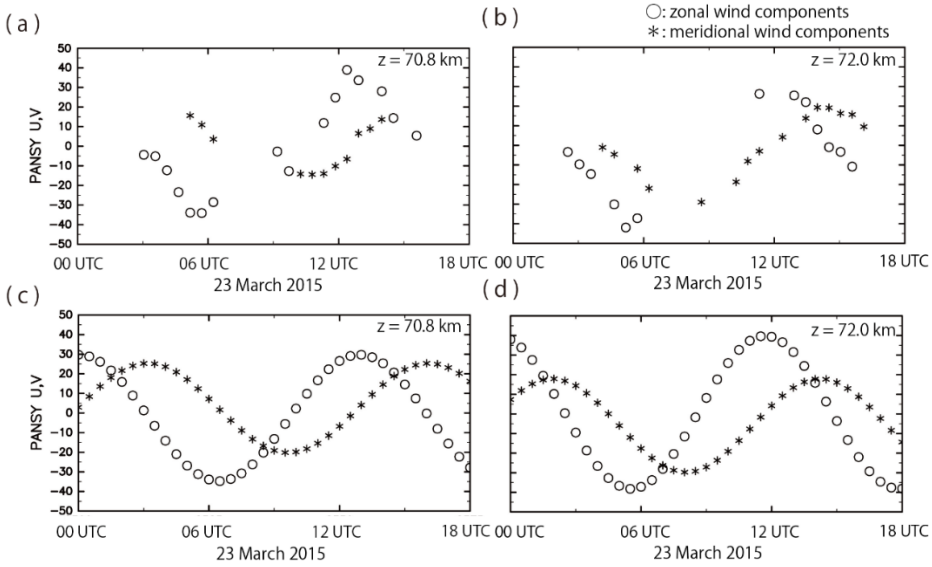

Figure 3.6: Zonal and meridional wind components observed by the PANSY radar on March 23 2015 as a function of time at heights of (a) 70.8 km and (b) 72.0 km. Zonal and meridional wind components fitted sinusoidal functions using a nonlinear least squares method at the height of (c) 70.8 km and (d) 72.0 km. The circles denote the zonal wind components and the star marks denote the meridional components.

vertical wavelength of the zonal wind component of the semi-diurnal migrating tide is about 4 m s^{-1} and 18 km at heights of 80-86 km in March, respectively, while that of the semi-diurnal non-migrating tides with $s = 1$ is about 10 m s^{-1} and 40 km, respectively. The wave parameters obtained in this study are quite different from those of the semi-diurnal tides. Thus, in this study, under the working hypothesis that wind disturbances observed in the mesosphere are due to inertia-gravity waves, wave parameters are estimated using a hodograph in time (e.g., Hirota and Niki 1986; Sato 1994).

The linear theory of inertia-gravity waves indicates that the hodograph has an elliptical shape (e.g., Shibuya et al., 2015). The lengths of major and minor axes of the hodograph ellipse correspond to the amplitudes of horizontal wind components which are parallel ($u_{\parallel}$) and orthogonal ($u_{\perp}$) to the horizontal wavenumber vector ($\overrightarrow{k_{\mathrm{h}}}$), respectively.

Table 1: The wave parameters of wind fluctuations in the mesosphere observed by the PANSY radar at Syowa Station (a) obtained by fitting to a sinusoidal function using a nonlinear least squares method (b) estimated on the hypothesis that fluctuations are due to inertia-gravity waves, where α is the angle of $u_{\parallel}$ measured clockwise from the east. The error bar is based on the uncertainty by using a nonlinear least square method.

Table 1a

Time and height locations	ω (s^{-1})	m (m^{-1}) from v'	C_{p_z}(m s^{-1}) from u'	m (m^{-1}) from v'	C_{p_z}(m s^{-1}) from v'
3/22 73.2 km	1.42×10^{-4} (12.3 h)	-5.24×10^{-4} (12.0 km)	-0.26	-7.42×10^{-4} (8.47 km)	-0.19
3/22 73.8 km	1.27×10^{-4} (13.7 h)				
3/22 74.4 km	1.59×10^{-4} (11.0 h)				
3/23 70.8 km	1.35×10^{-4} (12.9 h)	-4.08×10^{-4} (15.4 km)	-0.34	-5.11×10^{-4} (12.3 km)	-0.28
3/23 71.4 km	1.35×10^{-4} (12.9 h)				
3/23 72.0 km	1.42×10^{-4} (12.3 h)				

Table 1b

Time and height locations	u' (m s^{-1})	v' (m s^{-1})	$\lvert 2\pi/k_h \rvert$ (km)	α (degree)	$\frac{f}{\widehat{\omega}}$
3/22 73.2 km	28.5 ± 2.8	21.3 ± 2.8	1775 (1207 ~ 2797)	12° (7° ~ 32°)	0.72 (0.57 ~ 0.85)
3/22 73.8 km	30.3 ± 4.5	27.0 ± 4.5	3238 (1577 ~ 3407)	18° (5° ~ 77°)	0.86 (0.63 ~ 0.87)
3/22 74.4 km	28.3 ± 5.9	29.3 ± 5.9	1790 (1118 ~ 1793)	48° (17° ~ 75°)	0.76 (0.59 ~ 0.76)
3/23 70.8 km	32.2 ± 4.8	22.8 ± 4.8	1785 (990 ~ 7778)	2° (1° ~ 52°)	0.56 (0.41 ~ 0.97)
3/23 71.4 km	28.7 ± 6.1	22.1 ± 6.1	1454 (870 ~ 1523)	14° (11° ~ 61°)	0.63 (0.41 ~ 0.65)
3/23 72.0 km	39.0 ± 8.0	23.8 ± 8.0	1150 (570~ 1914)	14° (10° ~ 47°)	0.70 (0.32 ~ 0.74)

The components of $u_{\parallel}$ and $u_{\perp}$ are written using the zonal (u') and meridional (v') wind fluctuations:

$$u_{\parallel} = u' \cos\alpha + v' \sin\alpha$$
$$u_{\perp} = -u' \sin\alpha + v' \cos\alpha, \tag{3.6}$$

where α is the angle of $u_{\parallel}$ measured clockwise from the east. Based on the polarization relation, the intrinsic frequency $\hat{\omega}$ can be determined from the ratio of lengths of the major to minor axes:

$$\hat{\omega} = \left| \frac{u_{\parallel}}{u_{\perp}} f \right|, \tag{3.7}$$

where f denotes the inertial frequency. The intrinsic frequency is taken to be positive without losing generality (e.g., Sato et al., 1997). Moreover, negative vertical wavenumbers estimated in Table 1a indicate upward energy propagation of inertia-gravity waves.

The horizontal wavenumber $|\overrightarrow{k_h}|$ can be indirectly estimated using the dispersion relation of inertia-gravity waves, though an ambiguity for 180° remains in the direction of the horizontal wavenumber vector. For hydrostatic inertia-gravity waves, the dispersion relation in a uniform background field is written as follows:

$$|\overrightarrow{k_h}| = \sqrt{\frac{(\hat{\omega}^2 - f^2)m^2}{N^2}}, \tag{3.8}$$

where N is the Brunt-Väisälä frequency. Here, as a typical value for the mesosphere, N^2 = 3.0×10^{-4} s^{-2} was used. The zonal and meridional wavenumbers (k, l) are estimated as $k = \pm|\overrightarrow{k_h}| \cos\alpha$, and $l = \pm|\overrightarrow{k_h}| \sin\alpha$, respectively. The plus-minus sign here denotes the 180^{o} ambiguity of the wavenumber vector.

Figure 3.7 shows hodographs of the fitted sinusoidal fluctuations at heights of 70.8 km and 72.0 km for March 23. The intrinsic frequency and zonal and meridional wavenumbers are estimated from Eqs. (3.7) and (3.8), respectively. Table 1b presents the amplitudes of zonal and meridional wind fluctuations estimated by the fitting and wave parameters by the hodograph analysis. Wavenumber vectors point eastward (or westward) or northeastward (or southwestward). Parameter $f/\hat{\omega}$ ranges from 0.6 to 0.85.

Horizontal wavelengths of the best fitted parameters are longer than 1100 km, indicating that these fluctuations are likely due to relatively large-scale inertia-gravity waves. Thus, the applied assumption on the homogeneity of observed winds by dual beams (Section 3.2.1) is justified, if the working hypothesis is valid. Uncertainties of estimated wind amplitude and other related wave parameters are also estimated using residuals of the nonlinear least squares fitting and on the assumption that the uncertainties in the estimates of the zonal and meridional wind amplitude are the same. It seems that the estimated horizontal wavelength at a height of 70.8 km for March 23 has a relatively large uncertainty ($\left|2\pi/\overrightarrow{k_h}\right| = 990 \sim 7778$ km). However, it should be noted that the case for the largest horizontal wavelength corresponds to a case with $\hat{\omega} \sim f$ (i.e. close to the inertial oscillation) and hence its ambiguity is large for the wavelength ($\left|\overrightarrow{k_h}\right| \sim 0$). Note that the working hypothesis that wind disturbances are due to inertia-gravity waves will be validated by comparing estimated wave parameters from the PANSY radar with those from the numerical simulation using the NICAM shown in Section 3.4.

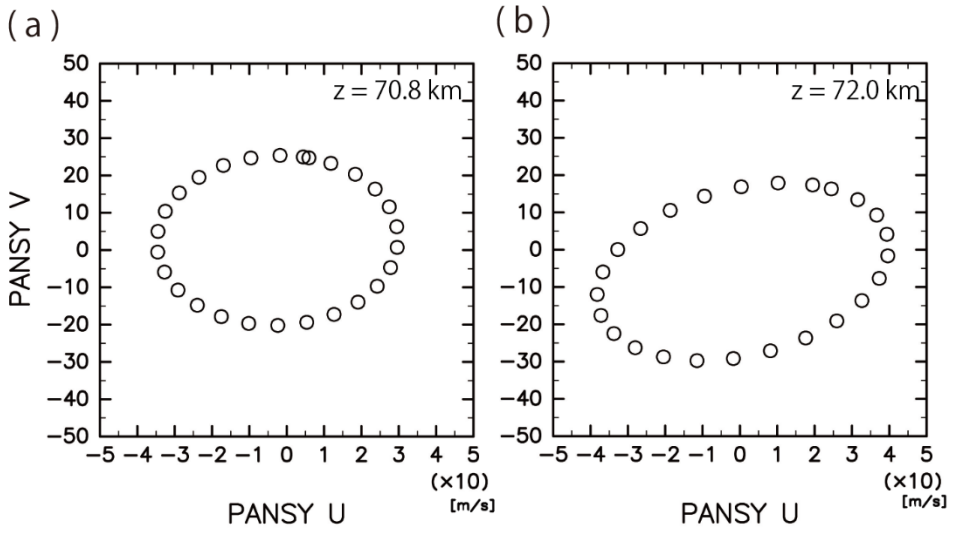

Figure 3.7 : A hodograph of the fitted horizontal wind components in time from 00 UTC 23 March to 13 UTC 23 March at the height of (a) 70.8 km and (b) 72.0 km from the PANSY radar observation. Each mark is plotted at one hour interval.

3.4. Numerical experiment results

3.4.1. Simulated wave structures

To examine spatial structures and generation mechanisms of the inertia-gravity waves, a model simulation based on the NICAM was performed. Figure 3.8a shows the time-height section of the line-of-sight speed of the east beam of the PANSY radar. ($u \sin\theta + w \cos\theta$, where $\theta = 10°$) at a grid point near Syowa Station from 00 UTC on March 17 to 00 UTC on March 24, 2015. By comparing wind fields simulated by the NICAM with those by the observations (Fig. 3.4), it is shown that the model successfully simulated disturbances with a period of several days in the troposphere, although phases of these disturbances vary slightly from observations near the end of the simulation. In the lower stratosphere, a wavy structure with vertical wavelengths shorter than about 2 km, which was observed by the radar from 00 UTC on March 17 to 00 UTC on March 20, is hardly seen in Fig. 3.8a. This feature may be attributable to the large vertical spacing ($\Delta z = 400$ m) of the model compared to such a short vertical wavelength. From the middle stratosphere to the mesosphere, downward-propagating disturbances with large amplitudes are dominant, which is consistent with the radar observations. Figures 3.8b and 3.8c show simulated line-of-sight wind speed of the east beam and the zonal wind for the same time and height sections as in Figs. 3.4b and 3.4c, respectively. The magnitude of the maxima of the zonal wind components are also comparable to the estimated amplitudes of the observed disturbances in Section 3.3; for example, a magnitude of a maximum of the zonal wind component at a height of about 70 km for 12 UTC on March 23 is approximately 30 m s^{-1}, which agrees with the amplitude of the disturbances estimated by the observations (Figs. 3.6a and 3.6c).

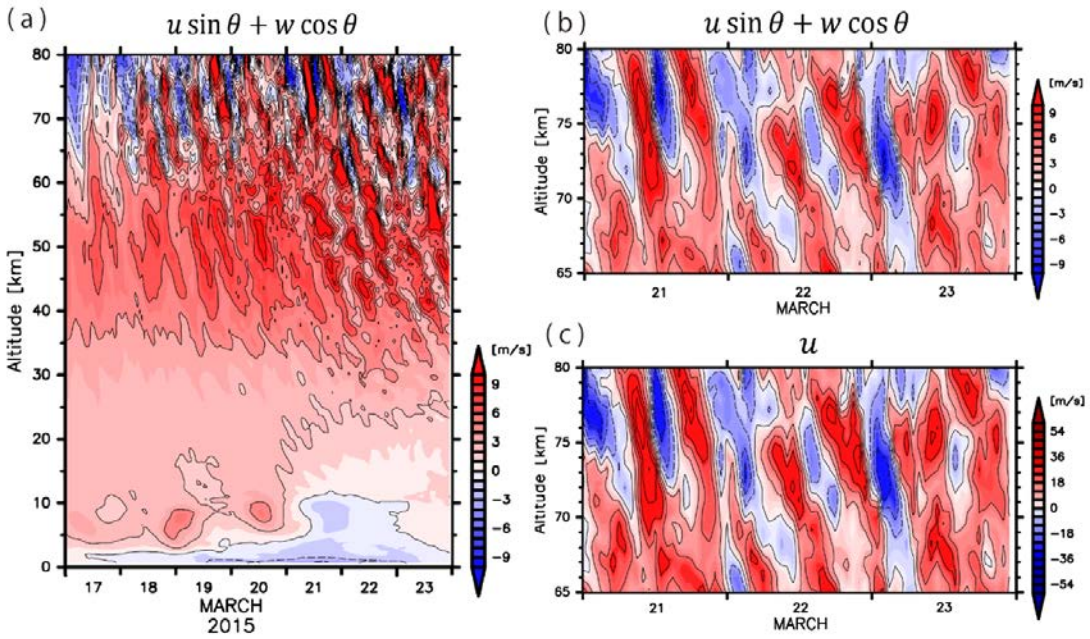

Figure 3.8: Time-altitude cross sections of eastward line of sight wind speeds simulated by NICAM at a grid point near Syowa Station (a) for the period from 17 March to March 23, 2015 and (b) for the period from March 21 to March 23, 2015 (contour interval 3 m s^{-1}). (c) Zonal wind components in eastward line of sight wind speeds simulated by NICAM for the period from March 21 to March 23, 2015 (contour interval 18 m s^{-1}).

Figure 3.9a shows the time-height section of anomalies of zonal wind components from the time average at each height. As is shown in Fig. 3.8b, wave-like structures for the observation period of about 12 h seem dominant in the mesosphere which is consistent with the radar observation (Fig. 3.4b). First, diurnal and semi-diurnal migrating tidal components are examined, which are defined as components with wave period $\tau = 24$ h and zonal wavenumber $s = 1$ and $\tau = 12$ h and $s = 2$, respectively. Figure 3.9b shows the time-height section of diurnal and semi-diurnal migrating components of zonal winds. Surprisingly, these components are not dominant even in the mesosphere. Figure 3.9c shows the time-height section of zonal winds of planetary waves, which are defined as components with $\tau \geq 42$ h. The planetary waves do not seem to be dominant in the mesosphere. Moreover, the amplitude of small-scale gravity waves is examined, which

are defined as components with horizontal wavelengths of less than 1000 km, as occasionally shown by previous studies (e.g., Geller et al., 2013). In this study, a spatial filter is applied to wind data gridded in the x-y coordinate centered at the South Pole as projected by the Lambert azimuthal equal-area projection. Figure 3.9d shows the time-height section of zonal wind components of the small-scale gravity waves. Although these small-scale gravity waves sometimes have amplitudes that exceed 20 m s^{-1} in the mesosphere, the dominant wave structures shown in Fig. 3.9a are not fully explained.

The remaining component is shown in Fig. 3.9e. This component has a quite similar structure and amplitude to the unfiltered anomalies shown in Fig. 3.9a. These results suggest that dominant wave structures in the mesosphere are not due to migrating tides, planetary waves or small-scale gravity waves, but due to the remaining component. The remaining component has horizontal wavelengths greater than 1000 km and wave periods of less than 42 h. Characteristics of the remaining component are further examined in terms of horizontal and vertical wavenumbers and intrinsic and observed (ground-based) wave frequencies.

It is seen that in Figure 3.9e that there are several wave packets with large amplitudes over Syowa Station. The envelope function of the wave packets is examined using an extended Hilbert transform method proposed by Sato et al. (2013). The extended Hilbert transform $H[a(x,t)]$ is a fluctuation field composed of a Fourier component of a particular fluctuation field $a(x,t)$ whose phase is shifted by $-\pi/2$ radians. An envelope function $A_{\mathrm{env}}(x,t)$ of $a(x,t)$ is obtained using $a(x,t)$ and $H[a(x,t)]$ as follows:

$$A_{\mathrm{env}}(x,t) = \sqrt{a(x,t)^2 + H[a(x,t)]^2}. \qquad (3.9)$$

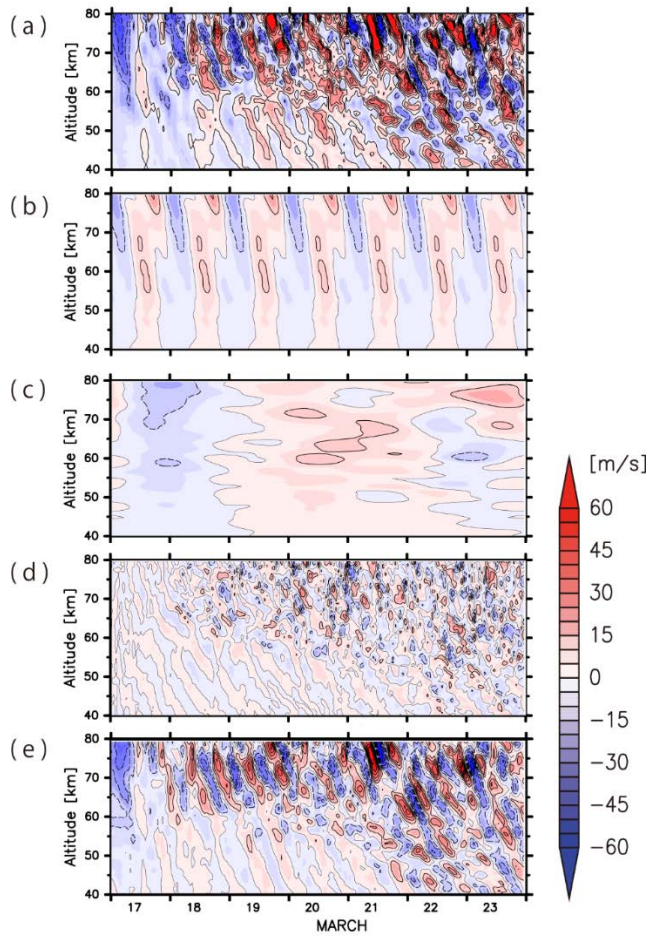

Figure 3.9:
Time-altitude cross sections of (a) anomalies of the zonal wind components from the time-mean components, (b) the diurnal and semi-diurnal migrating tidal components, (c) the planetary wave components, (d) small-scale gravity waves and (e) the remaining components. The contour intervals are 10 m s^{-1}. The data is from the NICAM simulation.

The extended Hilbert transform must be applied in one direction in time or space where waves are fluctuating (including at least more than two wave crests). In this study, envelope functions are estimated using the extended Hilbert transform in the time direction.

Figure 3.10 shows the envelope functions calculated using the extended Hilbert transform applied to the remaining components shown from the phase structure of the disturbances observed in Fig. 3.9e. Several large-amplitude wave packets are identified and labeled as (i) to (v) for further wave parameter estimation. The observed wave period and the vertical wavelength of each packet are estimated directly from phase structure of the disturbances observed in Fig. 3.9e. The zonal wavelengths and zonal phase speeds are directly estimated using Hovmöller diagrams. Figure 3.11 shows the Hovmöller diagram

at a height of 70 km at 69°S. A lot of wave packets appear not only over Syowa Station throughout the simulation period. However, disturbances with relatively long wavelengths seem dominant only during the initial day of the time integration. It is clear that most waves propagate westward. At a longitude of ~40°E (green dashed line) where Syowa Station is located, some dominant wave packets are found as shown in Fig. 3.10, such as packets (i) for March 19, (ii) March 20 and (v) March 22.

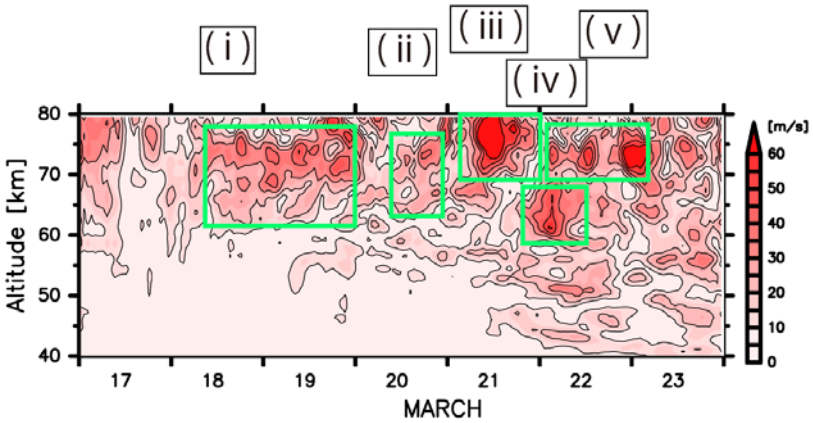

Figure 3.10: Time-altitude cross section of the envelope function of the zonal wind components of the large-scale gravity waves simulated by NICAM (contour interval 10 m s^{-1}) .The figure from (i) to (v) denote the labels of the wave packet examined in Section 4.

In addition, to examine horizontal structures of the wave packets, composite maps of zonal wind components are created. The composite is calculated for the time period denoted by green rectangles in Fig. 3.10. For each wave packet, the locations with the local maxima of the zonal wind components near Syowa Station along a latitude of 69°S are chosen as reference points for the composite. In other words, horizontal maps of zonal wind wave components are moved in the zonal direction and are then averaged. Thus, this composite shows an averaged phase structure of zonal wind wave components near Syowa Station. The results are shown in Figs. 3.12a to 3.12e for packets (i) to (v), respectively. It seems that wave structures are evident for all packets near Syowa Station.

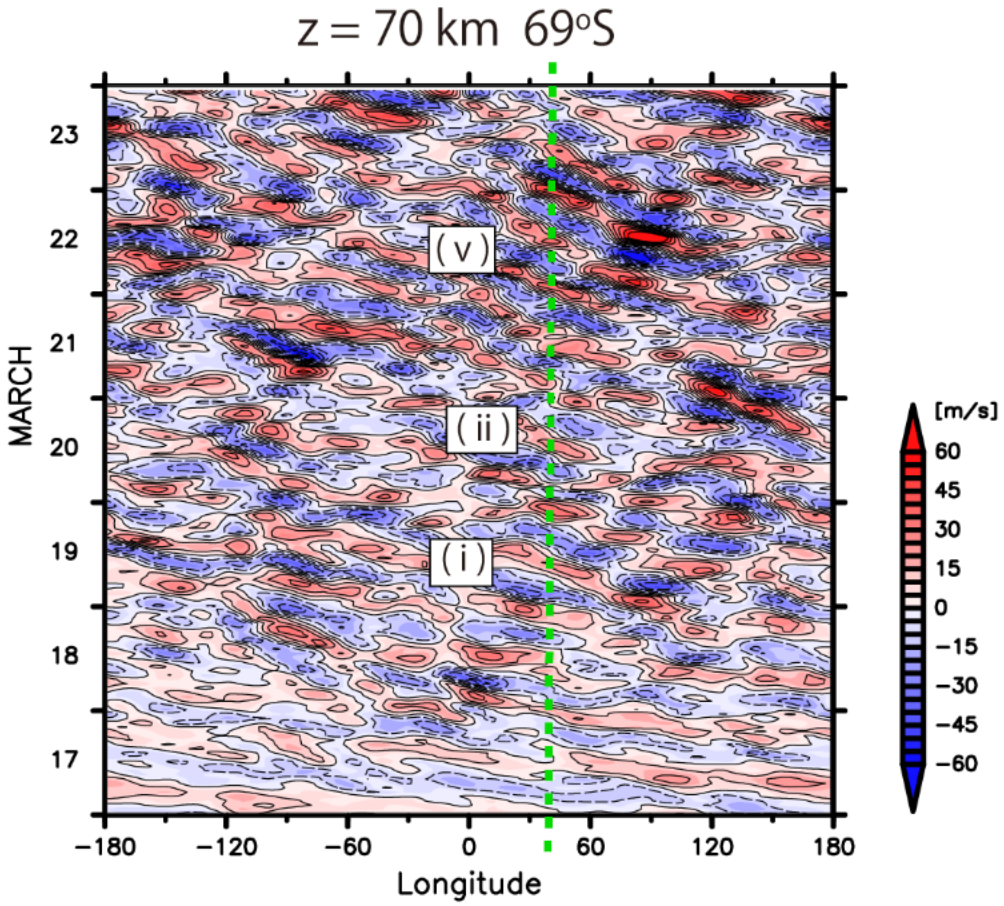

Figure 3.11: Hovmöller diagram of zonal wind components of the large-scale inertia-gravity waves simulated by NICAM at the height of 70 km at 69°S (contour interval 10 m s-1). The figures (i), (ii) and (v) indicate the packets labeled in Fig.3.7.

From features observed in the time-height section, the Hovmöller diagram and the composite maps of zonal wind components, we directly estimated wave parameters of horizontal wavelengths, vertical wavelengths, observed frequencies, zonal phase speeds, vertical phase speeds and intrinsic frequencies, which are summarized in Table 2.

The vertical phase speeds, observed wave periods and vertical wavelengths obtained from the model simulation data agree quite well with those obtained from the PANSY radar observations. Moreover, directly estimated zonal and meridional wavenumbers from the simulation (Table 2) also agree quite well with those indirectly estimated from the PANSY radar observations using polarization and dispersion relations of inertia-

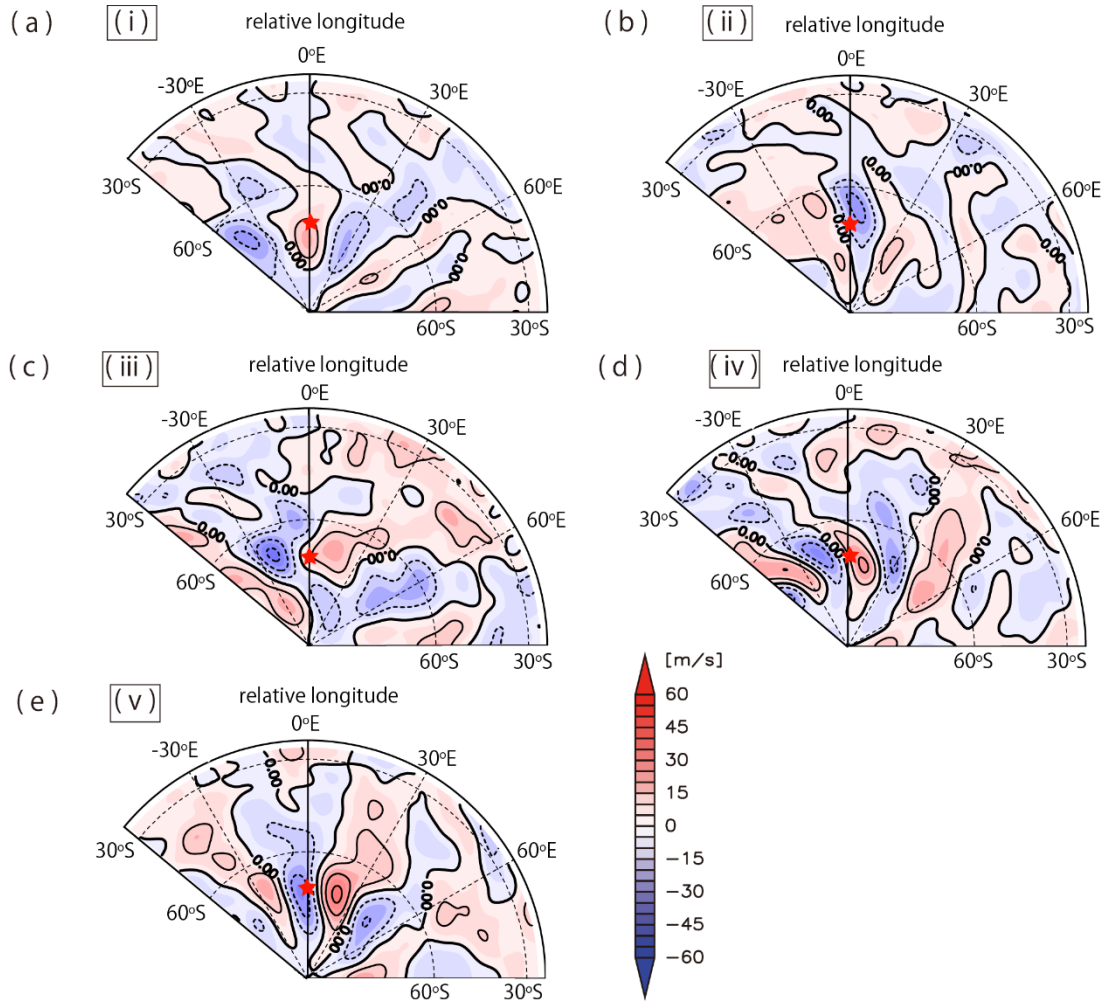

Figure 3.12: Composite maps of zonal wind components of the large-scale inertia-gravity waves simulated by NICAM. The height where the composites are taken is (a) 70 km, (b) 70 km, (c) 75 km, (d) 65 km, and (e) 72 km. The longitudinal location is depicted as the relative longitude from Syowa Station. The contour intervals are 10 m s^{-1}. The red star makes denote the location of Syowa Station.

gravity waves (Tables 1a and 1b). In addition, it is important to note that wave parameters (ω, $\vec{k}$ and m) of packets (i) to (v) are consistent with the dispersion relation of the hydrostatic inertia-gravity waves:

$$\hat{\omega}^2 = (\omega - \vec{U}\cdot\vec{k})^2 = f^2 + \frac{N^2|\vec{k}|^2}{m^2}, \qquad (3.10)$$

where ω is the observed frequency, $\vec{k} = (k, l)$ and m are horizontal and vertical components for the wavenumber vector, respectively, and $\vec{U}$ is the background

horizontal wind vector. Here the β effect is neglected for simplicity, since the wave packets have narrower spatial structures in the latitudinal direction, and the latitudinal dependence of f in the polar region is relatively small. Intrinsic frequencies $\hat{\omega}$ obtained from the model simulation using Eq. (6) also agree with those obtained from the PANSY radar observation. From these results, it is concluded that dominant disturbances with a period of quasi 12 h observed in the mesosphere are likely attributable to large-scale inertia-gravity waves. It should be noted that the background winds in this calculation are the zonal mean winds averaged between one day before and after the time when the center of the wave packet crosses over Syowa Station.

Table 2: The directly estimated wave parameters of simulated packets

Wave packets	k (m^{-1})	l (m^{-1})	m (m^{-1})	ω (s^{-1})	C_{p_x} (m s^{-1})	C_{p_z} (m s^{-1})	$\frac{f}{\hat{\omega}}$
	$\lvert k_h \rvert$ (m^{-1})						
(i) z = 70 km 3/18 12 UTC ~ 3/19 24 UTC	-2.48×10^{-6} (2530 km)	~ 0	3.96×10^{-4} (15.8 km)	1.42×10^{-4} (12.3 h)	−57.3	−0.36	0.763
	2.48×10^{-6} (2530 km)						
(ii) z = 70 km 3/20 05 UTC ~ 3/21 01 UTC	-3.18×10^{-6} (1980 km)	-0.98×10^{-6} (6440 km)	4.10×10^{-4} (15.3 km)	1.47×10^{-4} (11.8 h)	−4.62	−0.36	0.704
	3.33×10^{-6} (1887 km)						
(iii) z = 75 km 3/21 03UTC ~ 3/22 03 UTC	-2.79×10^{-6} (2250 km)	-2.48×10^{-6} (2530 km)	3.92×10^{-4} (16.0 km)	1.99×10^{-4} (8.8 h)	−71.3	−0.51	0.617
	3.73×10^{-6} (1685 km)						
(iv) z = 65 km 3/21 21UTC ~ 3/22 09 UTC	-3.35×10^{-6} (1880 km)	-2.78×10^{-6} (2530 km)	4.63×10^{-4} (13.57 km)	1.46×10^{-4} (11.9 h)	−43.5	−0.32	0.617
	4.35×10^{-6} (1444 km)						
(v) z = 72 km 3/22 02 UTC ~ 3/23 02 UTC	-3.78×10^{-6} (1660 km)	-0.82×10^{-6} (7660 km)	4.52×10^{-4} (13.9 km)	1.59×10^{-4} (11.0 h)	−42.1	−0.35	0.653
	3.87×10^{-6} (1625 km)						

3.4.2. Wave propagation and generation mechanism

In this section, the origins of the dominant disturbances with a period of quasi 12 h

in the mesosphere over Syowa Station are examined using simulation data. The disturbances with a period of quasi 12 h are extracted by applying a bandpass filter with cutoff wave periods of 6 h and 24 h to the remaining components. Hereafter, these disturbances are referred to as “quasi 12 h inertia-gravity waves”.

Case studies are conducted for wave packets (i) and (v), as they show clear wave structures at the height of 70 km where clear inertia-gravity waves were detected by the PANSY radar. The propagation of wave packets identified using the extended Hilbert transform method is manually traced. Three-dimensional locations of the wave packets are determined by the maxima of the envelope function for each time. Hereafter, this method is referred to as the “manual wave packet tracing”. The advantage of this method is that a specific location of a possible wave source can be directly examined.

The approach of the manual wave packet tracing is described below and is applied to packet (v) as an example. Figures 3.13a and 3.13b show horizontal maps of zonal wind components of the large-scale inertia-gravity waves and their envelope functions for 03 UTC on March 23 and a Hovmöller diagram at 69°S. Significant wave disturbances with large amplitudes are observed near Syowa Station corresponding to packet (v). The location of the center of packet (v) (green circles in Figs. 3.13a and 3.13b) is estimated in the following: First, the time when the envelope function of packet (v) takes its local maximum in the Hovmöller diagram (Fig. 3.13b) is determined. Second, the location where the envelope function has its local maximum in the horizontal map is regarded as the packet (v) location at that time (Fig. 3.13a). At one lower height, the time and location at which the center of packet (v) pass through the height surface are determined by those at which the envelop function takes a maximum for several hours before the time when the center of packet (v) pass through one higher level. By repeating this procedure with

$\Delta z = 1$ km, the temporal and spatial locations of packet (v) are manually estimated. If packet (v) is not dissipated, the propagation of packet (v) can be traced by the temporal and spatial location of the center of packet (v) at the height. Note that the meridional propagation of packet (v) can be also detected by this method. Such a manual packet tracing method is applied to the other wave packets. Figures 3.13c and 3.13d show the results for packet (i).

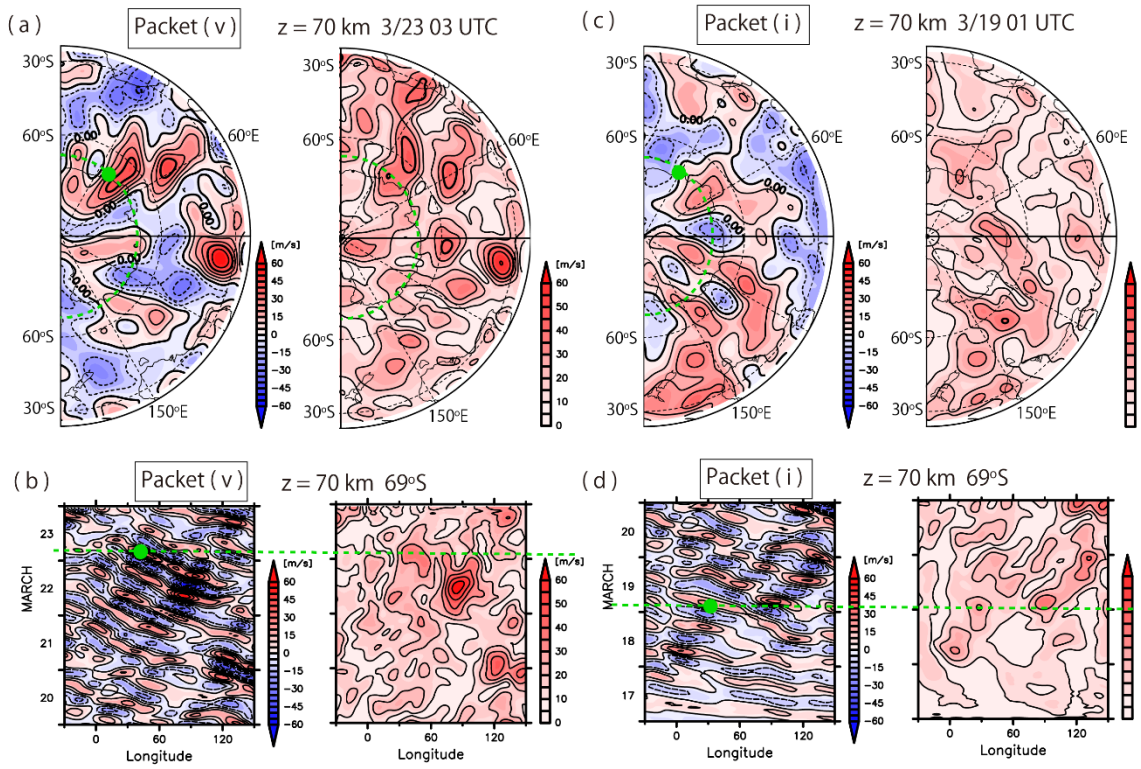

Figure 3.13: Snapshots of the zonal wind components and their envelope function of the quasi 12 h inertia-gravity waves (a) at a height of 70 km at 03 UTC 23 March 2015, corresponding to packet (v), and (c) at the height of 70 km at 01 UTC 19 March 2015, corresponding to packet (i). Hovmöller diagrams of the zonal wind components and their envelope function of the large-scale inertia-gravity waves at a height of 70 km at 69°S for the period (b) from March 20 to 23 and (d) from March 17 to 20. The green dashed curves in (a) and (c) denote the cross section taken in (b) and (d), and vice versa. The green circles are locations of traced wave packets determined by the method discussed in the text. The contour intervals are 10 m s^{-1}. The data is from the NICAM simulation.

Figures 3.14a-d show the time and spatial locations of packet (v) at heights of 60 km, 40 km, 25 km and 23 km, respectively. It appears that the location of packet (v) is successfully traced backward from a height of 70 km to 23 km, suggesting that packet (v) observed over Syowa Station in the mesosphere propagated from somewhere in the troposphere or the lower stratosphere below a height of 23 km. At heights of 25 km to 23 km, the vertical propagation of packet (v) is quite slow at roughly (100°E, 40°S) compared to that in the upper stratosphere and mesosphere.

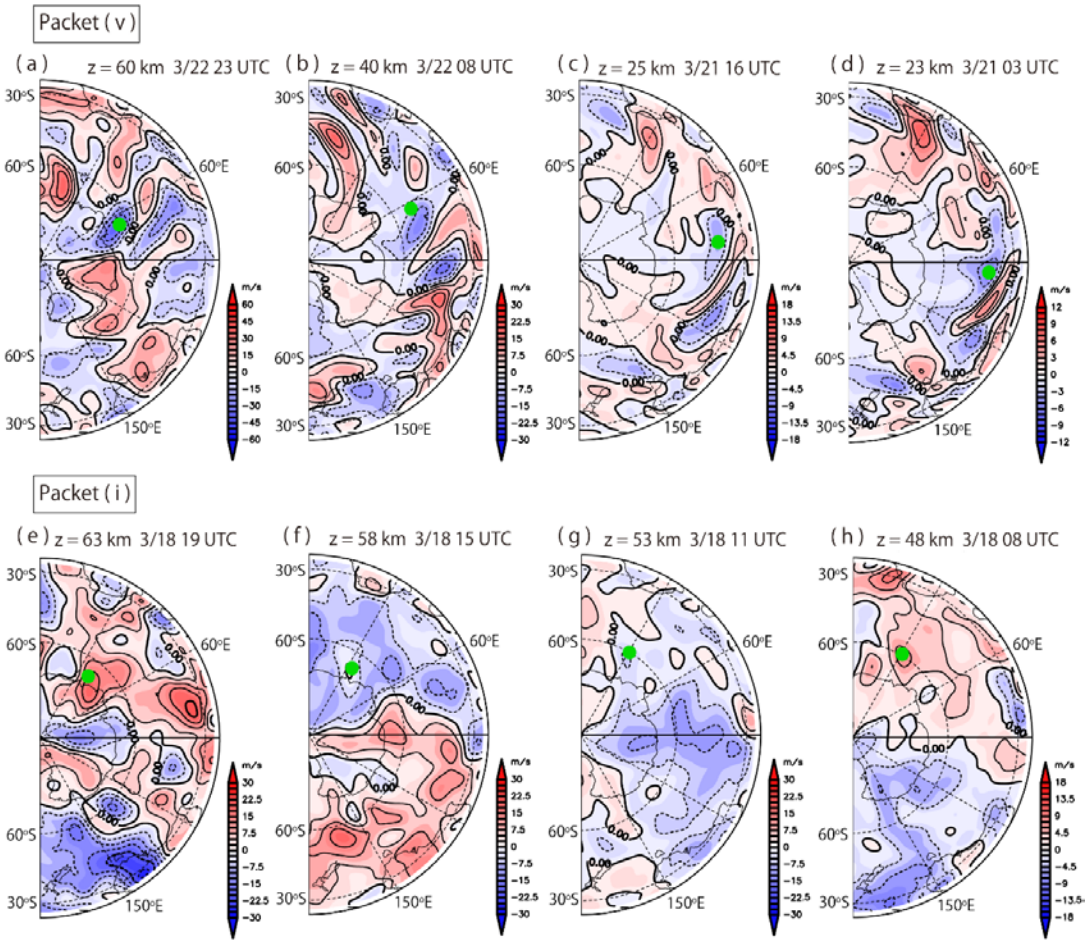

Figure 3.14: Snapshots of the zonal wind components of the quasi 12 h inertia-gravity waves tracing packet (v) (a) at the height of 60 km at 23 UTC 22 March (contour interval 10 m s^{-1}), (b) at the height of 40 km at 08 UTC 22 March (contour interval 5 m s^{-1}), (c) at the height of 25 km at 16 UTC 21 March (contour interval 3 m s^{-1}) and (d)

at the height of 23 km at 03 UTC 21 March (contour interval 2 m s^{-1}). Snapshots for packet (i) (e) at the height of 63 km at 23 UTC 22 March, (f) at the height of 58 km at 15 UTC 18 March, (g) at the height of 53 km at 11 UTC 18 March (contour interval 5 m s^{-1}), (d) at the height of 48 km at 08 UTC 18 March (contour interval 3 m s^{-1}).The green circles are locations of traced wave packets determined by the method discussed in the text. The data is from the NICAM simulation.

Figures 3.14e to 3.14 g show the times and spatial locations of packet (i) at heights of 63 km, 58 km, 53 km and 48 km, respectively. At heights of 70 km, 63 km and 58 km, the green circles seem to trace the same wave structures. However, packet (i) can not be traced below a height of 53 km and the wave structure becomes obscure at heights of 53 km and 48 km.

To confirm the validity of the manual wave packet tracing results, a backward ray tracing analysis which includes the time variation of the background wind is conducted (e.g., Eckermann and Marks, 1996). The wave parameters of packets (i) and (v) shown in Table 2 are used as initial parameters for the ray tracing analysis. As the background wind for the quasi 12 h inertia-gravity waves, wind components with horizontal wavelengths larger than 5000 km and with wave period longer than 24 h are used. Note that the diurnal migrating tide is included in the background wind fields. Figure 3.15 and Table 3 summarize the manual packet and ray tracing results. The time and spatial locations of packet (v) detected by the manual packet tracing agree well with those obtained by the idealized ray tracing. This result supports the validity of the manual wave packet tracing method based on the extended Hilbert transform and the ray tracing based on the inertia-gravity wave theory. On the other hand, the slow propagation in the lower stratosphere detected by the manual packet tracing is not represented well by the ray tracing. The time and spatial locations of packet (i) detected by the manual packet tracing agrees well with

those by the ray tracing results at above 58 km (the red and yellow marks) where clear wave structures are detected in the horizontal map. However, the locations of packet (i) at below 53 km (green and light blue marks) does not agree with those of the ray tracing analysis. It is considered that the disagreement is related to the disappearance of the clear wave structure below heights of 53 km. The disappearance of the wave packet (i) is closely related to a generation mechanism of packet (i) closely discussed later. During the propagation, it is shown in Table 3b that the zonal (meridional) wavelengths increases (decreases) due to the spatial structure of the background atmospheric fields such as winds and static stability, while the observed frequencies and the vertical wavenumber do not change largely.

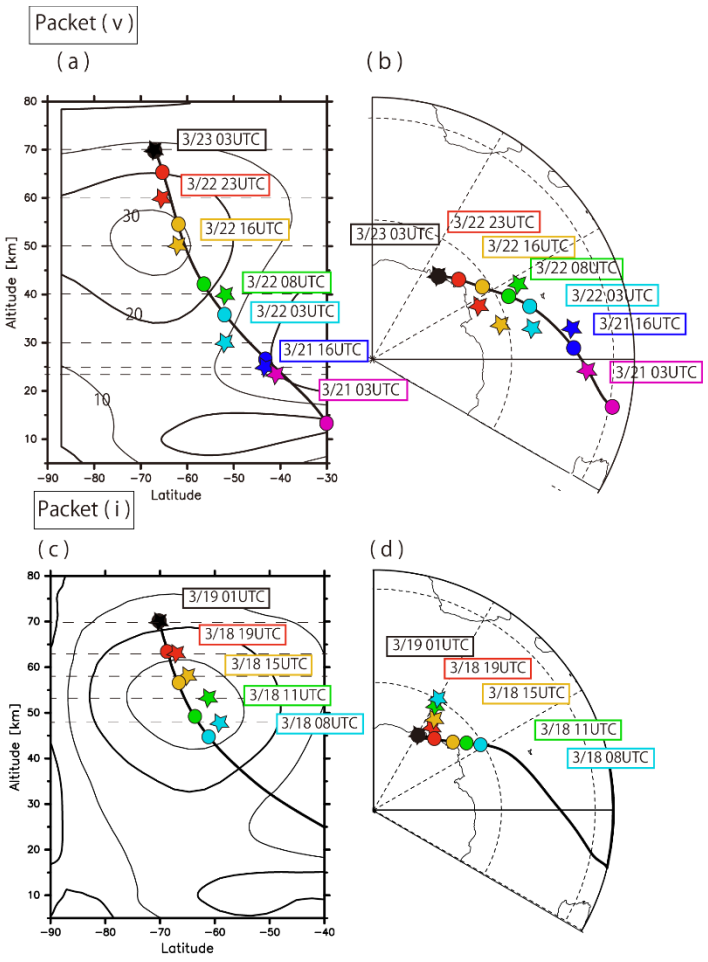

Figure 3.15:
The ray path of (a, b) packet (v) simulated by NICAM and (c, d) packet (i) using the ray tracing method (black thick line, colored circles) and the manual wave packet tracing method (colored star marks) in (a, c) the latitude-height cross section and (b, d) the horizontal map. The contours in (a, c) denotes background zonal wind component.

Source of the quasi 12 h inertia-gravity waves can be located at any altitude along the ray above the lowest traceable altitude. Thus, possible sources of packets (i) and (v) are further examined along the ray shown in Fig. 3.15. First, the ray of packet (v) in the lower stratosphere is examined. Figure 3.16 shows the longitude-height section of

Table 3a: The locations of the wave packet estimated by the manual wave packet tracing and the ray tracing

		Manual wave packet tracing			Ray tracing		
		Longitude [^{o}E]	Latitude [^{o}S]	Altitude [km]	Longitude [^{o}E]	Latitude [^{o}S]	Altitude [km]
Packet (v)	3/23 03 UTC	40	67	70.0	40.0	67.0	70.0
	3/22 23 UTC	68	66	60.0	45.9	65.5	66.0
	3/22 16 UTC	75	62	50.0	56.3	62.0	54.5
	3/22 08 UTC	63	52	40.0	66.8	56.3	41.7
	3/22 03 UTC	84	53	30.0	72.9	52.5	36.5
	3/21 16 UTC	80	43	25.0	87.6	43.1	26.7
	3/21 03 UTC	95	41	23.0	100.2	28.2	6.4
Packet (i)	3/19 01 UTC	30	70	70.0	30.0	70.0	70.0
	3/18 19 UTC	32	67	63.0	39.7	68.5	63.1
	3/18 15 UTC	33	66	58.0	47.0	66.7	56.3
	3/18 11 UTC	30	62	53.0	53.5	63.7	49.7
	3/18 08 UTC	30	59	48.0	57.7	61.0	44.6

Table 3: The wave parameter of the packets during the propagation estimated by the ray tracing

	Altitude [km]	k (m^{-1})	l (m^{-1})	m (m^{-1})	$\hat{\omega}$ (s^{-1})	ω (s^{-1})
Packet (v)	70.0	-3.78×10^{-6}	-0.82×10^{-6}	-3.96×10^{-6}	2.29×10^{-4}	1.59×10^{-4}
	66.0	-3.42×10^{-6}	-1.12×10^{-6}	-3.36×10^{-6}	2.34×10^{-4}	1.69×10^{-4}
	54.5	-2.93×10^{-6}	-1.40×10^{-6}	-2.78×10^{-6}	2.48×10^{-4}	1.78×10^{-4}
	41.7	-2.36×10^{-6}	-1.49×10^{-6}	-3.32×10^{-6}	2.17×10^{-4}	1.68×10^{-4}
	36.5	-2.08×10^{-6}	-1.43×10^{-6}	-3.47×10^{-6}	1.98×10^{-4}	1.66×10^{-4}
	26.7	-1.72×10^{-6}	-1.47×10^{-6}	-3.38×10^{-6}	1.78×10^{-4}	1.65×10^{-4}
P	70.0	-2.48×10^{-6}	~ 0	-3.43×10^{-6}	1.86×10^{-4}	1.42×10^{-4}

	63.1	-2.24×10^{-6}	-0.58×10^{-6}	-2.92×10^{-6}	1.96×10^{-4}	1.61×10^{-4}
	56.3	-1.98×10^{-6}	-0.92×10^{-6}	-2.53×10^{-6}	2.05×10^{-4}	1.58×10^{-4}
	49.7	-1.76×10^{-6}	-1.13×10^{-6}	-2.64×10^{-6}	2.01×10^{-4}	1.51×10^{-4}
	44.6	-1.59×10^{-6}	-1.23×10^{-6}	-2.99×10^{-6}	1.84×10^{-4}	1.49×10^{-4}

background winds below z = 18 km and of the quasi 12 h inertia-gravity waves above z = 19 km at 40°S for 03 UTC on March 21. At a roughly 100°E longitude, the quasi 12 h inertia-gravity waves appear to be captured over the core of the tropospheric jet stream. This feature is quite similar to the gravity waves generated by the spontaneous radiation from the large-scale jet around the tropopause (e.g., O'Sullivan and Dunkerton, 1995; Plougonven and Synder 2007; Yasuda et al., 2015a, b). The long propagation time in the lower stratosphere may be related to the wave capture mechanism (Bühler and McIntyre, 2005; Shibuya et al., 2015), which is closely discussed later.

To explore such a possibility, a horizontal map of the residual of the nonlinear balance equation (ΔNBE; Zhang et al., 2001), which is an index showing the degree of flow imbalance, is examined. Here, ΔNBE is defined as follows:

$$\Delta NBE = 2J(u,v) + f\varsigma - \alpha\nabla^2 P \qquad (3.11)$$

where ς, α, and P denote the relative vorticity, specific volume and pressure level, respectively. The Jacobian term is $J(u,v) = \partial u/\partial x \times \partial v/\partial y - \partial v/\partial x \times \partial u/\partial y$. To exclude possible contaminations of ΔNBE by small-scale gravity waves, a low-pass filter is applied in the zonal and meridional directions with a cutoff length of 1000 km in advance. Figure 3.17a and Figure 3.17b show horizontal maps of the absolute value of

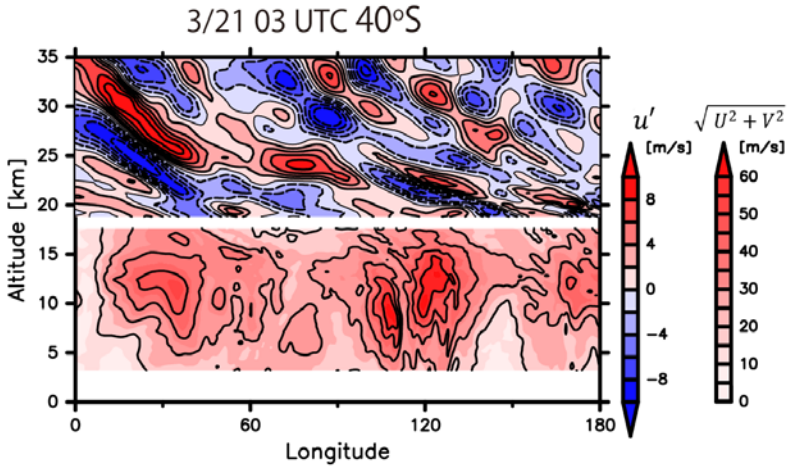

Figure 3.16: A snapshots of longitude-height cross sections of zonal wind components of the quasi 12 h inertia-gravity waves (above the height of 19 km, the left color bar, contour interval 2 m s^{-1}) and the absolute values of the horizontal wind components (below the height of 18 km, the right color bar, contour interval 10 m s^{-1}) at 03 UTC 21 March at 40°S. The data is from the NICAM simulation.

the horizontal wind and ΔNBE at a height of 10 km for 03 UTC on March 21. The absolute value of the horizontal wind is also denoted by thick contours. It is clear that ΔNBE is large around the tropospheric jet meandering around (110°E, 40°S) where packet (v) was located. This feature suggests not only that the imbalance in the tropospheric jet was significant, but also that packet (v) may have been generated by the spontaneous radiation mechanism. Furthermore, since the spatial scale of the meandered jet seems comparable to that of packet (v), the background field used in the ray tracing method may not include this structure. This is likely the reason that the wavenumber vector of packet (v) in the ray tracing analysis is not strongly deformed in the lower stratosphere (Table 2). In other words, this means that the WKB approximation used in the ray tracing analysis is not valid for the atmospheric fields during the spontaneous radiation process as discussed in Yasuda et al. (2015), which is one of the limitation of the ray tracing analysis. Figure 3.17c shows horizontal maps of the absolute value of the horizontal wind at a height of 300 hPa for 03 UTC on March 21 from the MERRA

reanalysis data. The meandering of the tropospheric jet stream around (110°E, 40°S) is also observed in the same time period in the MERRA reanalysis data, although the meandering seems slightly weaker. It is confirmed that the meandering of the tropospheric jet was associated with a cyclonic disturbance which was quasi-stationary around (110°E, 40°S) over 2 days (not shown).

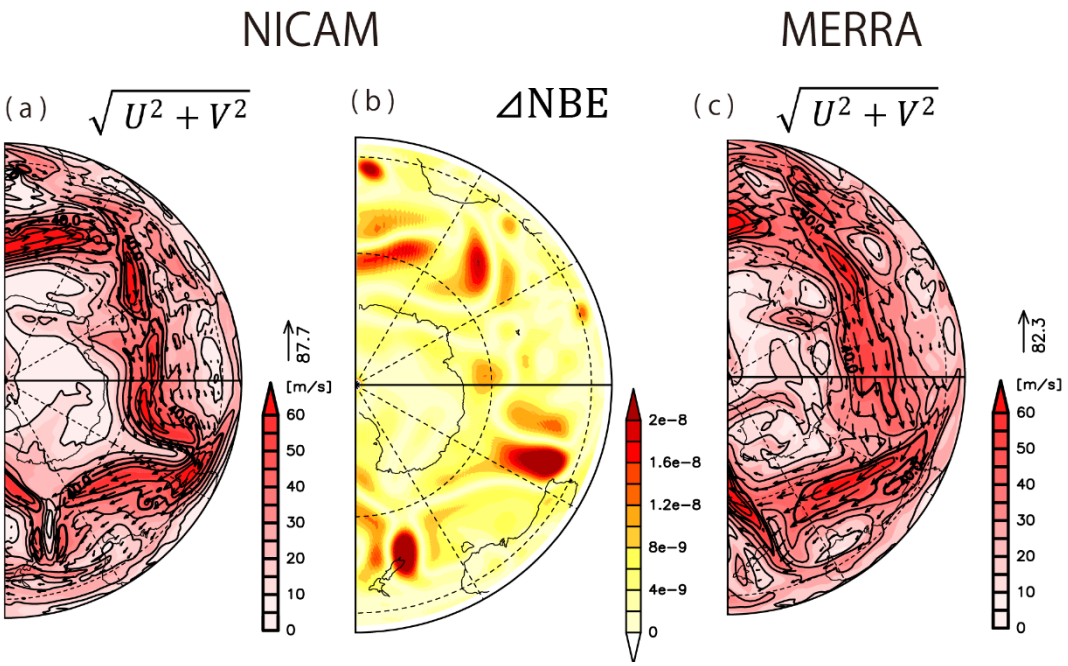

Figure 3.17: Snapshots of horizontal maps of (a) the absolute horizontal wind velocity and (b) the residual of the nonlinear balance equation (ΔNBE) at a height of 10 km from the NICAM simulation and (c) the same as (a) at a height of 300 hPa from the MERRA reanalysis at 03 UTC 21 March 2015. The vectors in (a) denote the directions and the magnitude of the horizontal winds. The contour intervals in (a) are 10 m s^{-1}.

Next, a possible generation mechanism for packet (i) is examined. The disappearance of the clear wave structure at a height of 53 km (Figs. 3.14f and 3.14g) may indicate that the source of packet (i) is present at this height. A plausible generation mechanism of inertia-gravity waves in the upper stratosphere is spontaneous radiation

from the polar night jet (e.g., Sato and Yoshiki, 2008). It is also worth noting that observational studies show high percentages of downward gravity wave propagation in the polar stratosphere compared to those at low and middle latitudes (e.g., Yoshiki and Sato, 2000; Guest et al., 2000; Moffat-Griffin et al., 2013; Murphy et al., 2014; Mihalikova et al., 2016). To confirm this possibility, fluctuation characteristics and background zonal winds of the upper stratosphere are examined. Figure 3.18 shows a longitude-height cross-section of zonal wind fluctuations weighted by square root of atmospheric density ($\sqrt{\rho_0}u'$) and the background zonal wind at 15 UTC on March 18 at 65°S. The background zonal wind is obtained using a low-pass filter with a cutoff zonal wavelength of approximately 5000 km.

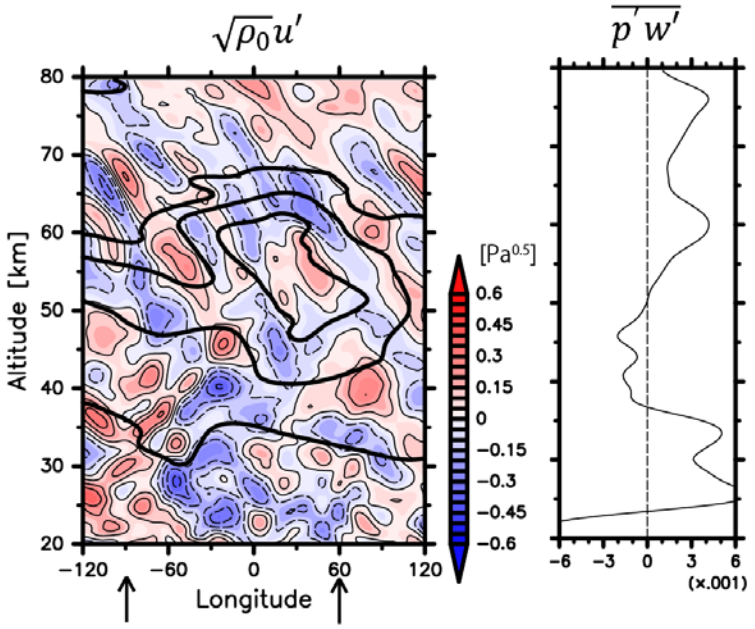

Figure 3.18: (a) A longitude-height cross section of zonal wind components of the quasi 12 h inertia-gravity waves $\sqrt{\rho_0}u'$ at 65°S at 15 UTC 18 March (contour interval 0.1 Pa$^{0.5}$), and (b) a line plot of the energy flux $\overline{p'w'}$ averaged over a longitude region from 90°W to 60°E denoted by black arrows. The thick black contours show background zonal wind components extracted by a lowpass filter with a cutoff wavelength of 5000 km. The thick contours denote 20 m s^{-1}, 30 m s^{-1} and 40 m s^{-1}, respectively. The data is from the NICAM simulation.

Interestingly, it seems that quasi 12 h inertia-gravity waves show symmetric phase structures above and below the core of the polar night jet at a height of 50 km. The height at which packet (i) becomes obscure roughly corresponds to the core of the polar night jet (Figs. 3.14f and 3.14g). This result suggests that the quasi 12 h inertia-gravity waves are generated at a height close to the core of the polar night jet. To confirm this, the vertical profile of the energy flux $\overline{p'w'}$ is examined (Fig. 3.18b). The average was taken for the longitudinal region spanning from -90°E to 60°E. The energy flux is upward above and downward below the core of the polar night jet. This result supports the hypothesis that packet (i) was generated at a height close to the core of the polar night jet.

This symmetric phase structure observed in Fig. 3.18a is similar to the structures from the theoretical studies of spontaneous radiation of inertia-gravity waves from a balanced flow (e.g., Yasuda et al., 2015b: their Figure 6). Hereafter the previous theoretical studies about the spontaneous radiation of inertia-gravity waves are shortly reviewed. Yasuda et al. (2015a, b) proposed a quasi-resonance of gravity waves and a secondary circulation slaved to a balanced flow as the spontaneous radiation mechanism. The quasi-resonance occurs when ground-based wave periods of radiated gravity waves are comparable to the time scale of the slaved motion due to a significant Doppler shift by the strong balanced flow. Figure 3.19 shows the schematic illustration for the spontaneous radiation of gravity waves in Yasuda et al. (2016). In Fig. 3.19, the red arrow denotes the strong localized jet and the blue arrows denote vertical compensation flow at the entrance and exit region of the jet. The vertical flow couplets are slaved components and are produced by the vortical flow over the deformed potential temperature surfaces (the blue curves), which are also the slaved components. Doppler-shifted gravity waves

are radiated because of the quasi resonance with the slaved components (i.e., the vertical flow couplets) when the space–time scales of the GWs are partially comparable to those of the slaved components. These potential temperature surfaces act as mountains, such as ones that generate orographic GWs. At the timing of the spontaneous radiation, the vertical flow couplets are considered to be both the slaved components and radiated gravity waves.

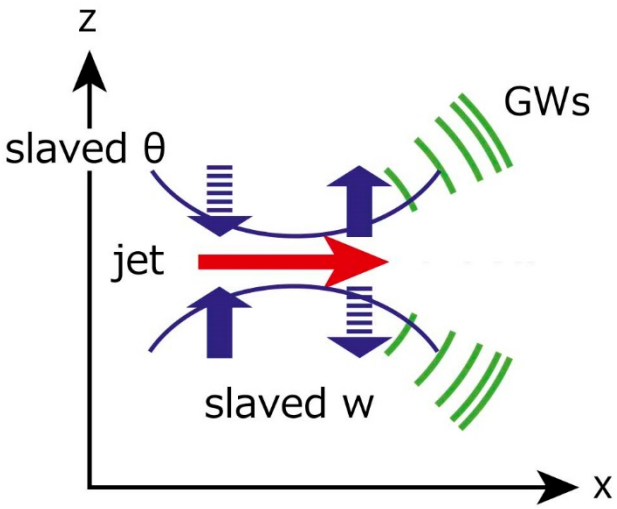

Figure 3.19: Schematic illustration of spontaneous gravity wave (GW) radiation from a localized jet stream caused by the mountain-wave-like mechanism proposed by McIntyre (2009). The blue arrows show the vertical flow composed of the slaved components. Doppler-shifted GWs are radiated because of the quasi resonance with the slaved components (i.e., the vertical flow couplets) when the space–time scales of the GWs are partially comparable to those of the slaved components. These vertical flow couplets are a compensation flow for the strong localized jet and are produced by the vortical flow over the deformed potential temperature surfaces, which are also the slaved components. Adapted from Yasuda et al. (2016).

As a quantitative condition for the spontaneous radiation of the gravity waves, a time-scale in which a fluid particle travels over a descent-ascent couplet structure (i.e., half of an intrinsic period of a radiated gravity wave; $\hat{\tau}$) needs to be shorter than half of

the inertial period $\left(\pi/f\right)$. This corresponds to the condition that the Lagrangian Rossby number (R_{Lagr}) is greater than unity, which was discussed in McIntyre (2009):

$$R_{\mathrm{Lagr}} = \frac{\pi}{\hat{\tau} f} = \frac{\frac{\pi}{f}}{\hat{\tau}} > 1. \tag{3.12}$$

Gravity waves generated by the spontaneous radiation mechanism initially have a large spatial scale comparable to the jet structure (blue arrows in Fig. 3.19). The wavelength of the radiated gravity waves gradually decreases through a deformation process by the background wind. This process is referred to as "the wave capture process" (Bühler and McIntyre, 2005). The theoretical explanation is based on the ray tracing equation with the WKB approximation, which describes the time-evolution of a phase and amplitude of a slowly varying wave packet. The time-evolution of the $\vec{k}$ along the group velocity ray is derived:

$$\frac{d_g \vec{k}}{dt} = -\frac{\partial \Omega}{\partial x}, \tag{3.13}$$

where $\vec{U}$ denotes the background wind velocity, Ω denotes the absolute frequency function defined as $\Omega = \hat{\omega} + \vec{k} \cdot \vec{U}$ and d_g/dt denotes the time derivative along the ray defined as $\partial/\partial t + \overrightarrow{c_g} \cdot \vec{\nabla}$. Assuming that the explicit dependence of Ω on x and t is contained entirely in the background wind $\vec{U}(x,t)$ and the background vertical wind velocity is negligible, the time evolution of the horizontal wavenumber vector $\overrightarrow{k_H} = (k,l)$ is decoupled from that of the vertical wavenumber m:

$$\frac{d_g}{dt}\begin{pmatrix} k \\ l \end{pmatrix} = -\begin{pmatrix} U_x & V_x \\ U_y & V_y \end{pmatrix}\begin{pmatrix} k \\ l \end{pmatrix}, \tag{3.14}$$

and

$$\frac{d_g m}{dt} = -U_z k - V_z l. \tag{3.15}$$

In the case that the background wind is non-divergent such as the geostrophic flow ($U_x + V_y = 0$) and steady, the long-time behavior of $\overrightarrow{k_H}$ is explained by the exponential growth following the eigenmode of the matrix:

$$\overrightarrow{k_H}(t) \propto \left(-V_x, U_x + \sqrt{D}\right) \exp \sqrt{D}t, \tag{3.16}$$

where $\sqrt{D}$ is the eigenvalue of the horizontal background gradient tensor and D is the determinant of the matrix, $D = {U_x}^2 + V_x U_y$. The long-time behavior of m is diagnostically determined by that of $\overrightarrow{k_H}$:

$$m(t) \propto -\frac{U_z k(t) + V_z l(t)}{\sqrt{D}}. \tag{3.17}$$

Thus, the horizontal wavenumber vector tends to be infinity at the exponential rate $\sqrt{D}$ in the case of $D > 0$ and $-V_x \neq 0$ or $U_x + \sqrt{D} \neq 0$, and so does the vertical wavenumber. Because the intrinsic group velocity $\widehat{C_g}$ decreases with the wavenumber, the wave packet begins to move with (be captured by) the local background flow. This is the reason why such deformation process is called the "wave capture" process. In Fig. 3.19, the wavelength of the radiated gravity waves gradually decreases near the exit region of the jet stream by the wave capture process under the strong shear of the background wind. According to the ray-tracing equation, the amplitude of the fluctuations also grows exponentially under the conservation of the wave action of the packet, which leads to wave dissipations at the exit region of the jet by non-conservative processes such as instabilities. In realistic atmospheric situations, however, it has been reported that parts of the radiated gravity waves propagate away from the jet core in the middle of the wave capture process (e.g., Shibuya et al., 2015) under an unsteady background flow.

Thus, at present, it is considered that the spontaneous radiation of the gravity waves occurs i) when the spatial and time scales of the gravity waves with the Doppler shift are partially comparable to those of the slaved components and ii) with $R_{\mathrm{Lagr}} > 1$. In

addition, the radiated gravity waves are deformed iii) under a large shear of the background wind. The typical baroclinic lifecycle experiment matches these conditions (Plougonven and Snyder, 2005). The amplitude of the radiated gravity waves increases under a larger local Rossby number, R_o (Sugimoto and Plougonven, 2016). Yasuda et al. (2015a, b) also showed that the source term formula of radiated gravity waves by the quasi-resonance obtained by the renormalization method is equal to ΔNBE.

However, a large ΔNBE was not observed in the upper stratosphere and mesosphere for the case examined in the present study. The polar night jet around an approximate height of 55 km did not have the strength and/or did not meander enough to cause a large ΔNBE (not shown). Thus, a different mechanism needs to be considered to explain the spontaneous radiation of quasi 12 h inertia-gravity waves in the upper stratosphere and mesosphere.

Taking into account the fact that the time variation of the westerly jet around 55 km is mainly caused by migrating tides, we propose a new mechanism for the spontaneous radiation in the upper stratosphere and mesosphere. Figure 3.20 shows the schematic illustration. Figure 3.20a shows anomalies of θ from the zonal mean and vertical wind fluctuations associated with a semi-diurnal migrating tide at the height of the core of the polar night jet in the longitudinal direction. As vertical winds are adiabatically present along the modulated θ surface, a mountain-wave-like generation that was discussed in the previous studies may occur. In this case, the vertical winds oscillate with a period of 12 h due to the time variation of the θ surface associated with the semi-diurnal migrating tide. An intrinsic period $\hat{\tau}$ for this case is calculated as $\hat{\tau} = {}^{L}/_{(U + C_{\mathrm{tide}})}$, where L is a half-length of the latitude circle, U is a speed of the zonal wind and C_{tide} is a ground-

based phase speed of the semi-diurnal tide. Since L/C_{tide} is 12 h, $\hat{\tau} = L/(U + C_{\mathrm{tide}})$ is less than a 12 h in the westerly background wind ($U > 0$). In addition, a half of the inertial period $\left(\pi/f\right)$ should be longer than 12 h by its definition, indicating that $R_{\mathrm{Lagr}} = \frac{\pi}{\hat{\tau} f}$ is always greater than unity in $U > 0$. Thus, the necessary conditions for the spontaneous radiation of quasi 12 h inertia-gravity waves are satisfied around the jet core, suggesting that quasi 12 h inertia-gravity waves with $s = 2$ and the zonal phase speed of C_{tide} can be radiated. In this case, the deformation of the θ surface is not caused by the slaved components of the large-scale balanced flow, and hence ΔNBE does not need to be large.

In addition, because the horizontal shear along the polar vortex is mainly caused by the migrating tides, the region where the horizontal shear is large also propagate westward with the zonal phase speed of C_{tide}. Thus, it is suggested that the deformation of the wavenumber vector occurs at a fixed phase of the $s = 2$ gravity wave with C_{tide} at the beginning of the wave capture. When the horizontal wavelength of the $s = 2$ gravity waves becomes shorter than that of the semi-diurnal migrating tide during the wave capture process, the zonal phase speed becomes slower than C_{tide} and hence the wave packet can be radiated from the strong-shear region migrating with C_{tide}. In such case, the horizontal wavelength does not become much shorter as in the wave capture process around the tropopause, since the wave packet may not stay for so long a time period as to be deformed around the strong-shear region migrating with the fast time-scale in the mesosphere.

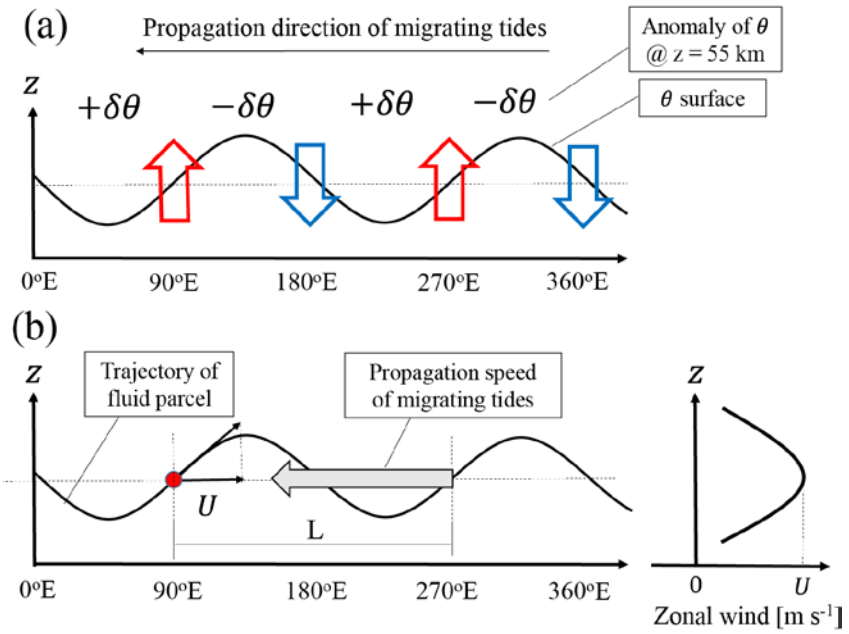

Figure 3.20: (a) a schematic figure of longitudinal locations of anomalies of θ ($\delta\theta$) from the zonal mean due to the semi-diurnal tide, and associated vertical wind couplets denoted by large arrows at a height of the core of the polar night jet. (b) A trajectory of fluid parcel on a θ surface at the height of polar night jet. The thin dashed arrow denotes a motion of the fluid parcel, and U denotes the magnitude of the background zonal wind.

Next, it is confirmed if the patterns of θ anomalies and vertical velocities associated with the migrating tides are seen in the simulation data. Figure 3.20a shows the Hovmöller diagram of θ anomalies and vertical wind fluctuations associated with the diurnal and semi-diurnal migrating tides at a height of 55 km at 65°S. The phase relation of θ and vertical velocities is consistent with an adiabatic process, which supports the scenario shown in Fig. 3.20a. The θ anomalies associated with the semi-3.21b shows the Hovmöller diagram of θ and vertical wind components of the quasi 12 h inertia-gravity waves, overlaid by the background zonal wind. Note that the background zonal wind is largely modulated by the migrating tides. It is interesting that packet (i) seems to be generated near 30°E at about 12 UTC when the packet is located downstream

of the zonal wind maxima. The source location and generation timing of packet (i) is consistent with the estimation using the manual packet tracing method. This fact suggests that the deformation process occurs in association with the horizontal wind shear caused by the migrating tides. Next, the stretching rate $\sqrt{D}$ (and hence e-folding time) in Eq. (3.17) is estimated at downstream of the zonal wind maxima. The e-folding time is about 1 day at the time periods from 17 to 18 May, This means that the gravity waves with $s = 2$ is deformed to those with the zonal wavelength of 2500 km about during 1 day, which seems a realistic time-scale for the deformation of packet (i). Thus, the proposed mechanism (Fig. 3.20) is the most likely mechanism of packet (i) generation.

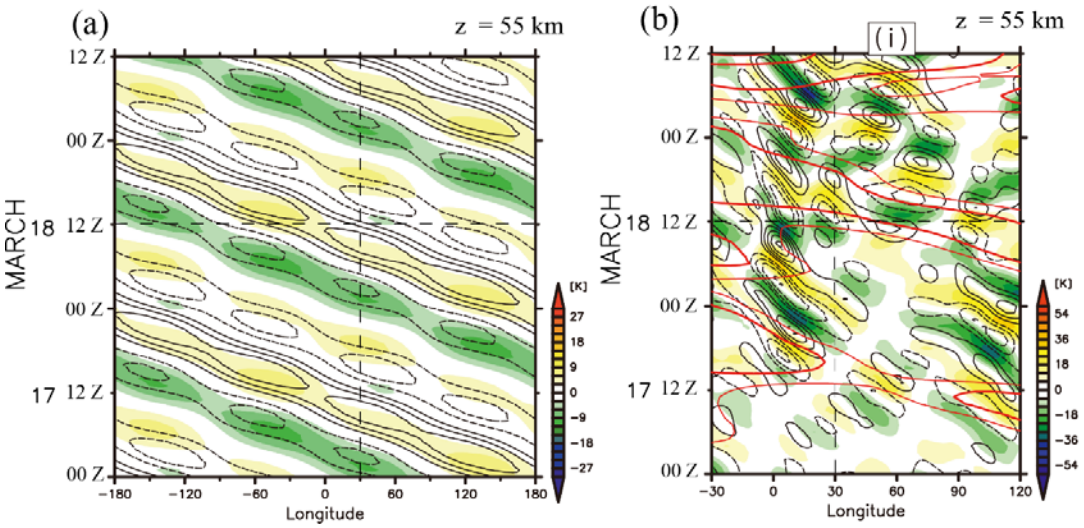

Figure 3.21: (a) A Hovmöller diagram of potential temperature (color shade) and the vertical wind components (contour) due to the diurnal and semi-diurnal migrating tides at the height of 55 km at 65°S. The contour interval is 0.5×10^{-2} m s^{-1}. (b) A Hovmöller diagram of potential temperature (shade) and the vertical wind components (black contour) of the large-scale inertia gravity waves, and the zonal wind component with $s = 0$, $s = 1$ and $s = 2$ (red contour) at the height of 55 km at 65°S. The black contour interval is 2.0×10^{-2} m s^{-1}, the red thin contour denotes 30 m s^{-1} and the red thick contour denotes 35 m s^{-1}. The data is from the NICAM simulation.

We also examined sources of other wave packets (ii), (iii) and (iv) and of other wave packets that are dominant at different longitudes (Fig. 3.11). The results suggest that these

wave packets were also generated by spontaneous radiation from the upper tropospheric jet stream or from the polar night jet stream (not shown in detail).

3.5. Discussion

As is shown in Section 3.4, wave structures with large amplitudes in the lower mesosphere (below 80 km) with the ground-based period of quasi 12 h are likely due to quasi 12 h inertia-gravity waves. Their horizontal wavelengths range from 1500 km to 2500 km as shown in Table 2. This conclusion is largely different from the suggestions made in previous studies, namely migrating $(s = 2)$ semi-diurnal tides, non-migrating $(s = 1)$ semi-diurnal tides or gravity-wave momentum deposition modulated by the migrating semi-diurnal tides. This difference can be attributed to the analysis techniques in which disturbances with a period of 12 h are examined. In many previous studies, disturbances with a period of 12 h were extracted by making a monthly mean climatology wind field from long-term time series, since they were thought of as the semi-diurnal tides (e.g., Murphy et al., 2006). It is thought that quasi 12 h inertia-gravity waves were averaged out during such an averaging process. On the other hand, Riggin et al. (1999) examined amplitudes and phases of disturbances with a period of 12 h from MF radar data by using a singular value decomposition (SVD) sinusoidal fit with a Gaussian localizing window having its width of ± 3 periods (i.e., 3 days for 12 h waves). The amplitudes of the disturbances with a period of 12 h were frequently larger than 20 m s^{-1} at a height of 90 km during October to early March. They also examined spatial phase differences of the disturbances with a period of 12 h at two different observational stations. It was shown that the large-amplitude disturbances with a period of 12 h during October to early March were not fully explained by the semi-diurnal migrating or non-migrating tides. Thus, the quasi 12 h inertia-gravity waves examined in the present study likely

contributed to such structures observed at the different stations.

Inertia-gravity waves with horizontal wavelengths longer than 1000 km in the mesosphere have been reported in several studies (Li et al., 2007; Lu et al., 2009, Nicolls et al., 2010; Chen et al., 2013). For example, Nicolls et al. (2010), using the Poker Flat Incoherent Scatter Radar system, found large-amplitude coherent wave packets with wave periods of roughly 10.5 h and horizontal wavelengths of 700-1600 km in the mesosphere. Nicolls et al. (2010) discussed a jet stream adjustment around the tropopause as a potential source. Chen et al. (2013) also estimated a source for one inertia-gravity wave with a horizontal wavelength of 2200 km, a period of 7.7 hour and a vertical wavelength of 22 km, which was observed in the Antarctic mesopause region based on Fe lidar and MF radar measurements. They heuristically traced the inertia-gravity wave back to a region of an unbalanced flow in the stratosphere (z ~ 43 - 46 km). However, no previous studies have directly examined sources of these large-scale inertia-gravity waves in the mesosphere using a numerical model. The present study first examined the propagation of such inertia-gravity waves and generation by spontaneous radiation from the polar night jet and/or the tropopausal jet by a combination of high-resolution observation data and numerical simulation outputs.

Recently, Sato et al. (2017) showed using continuous observations of polar mesosphere summer echo data observed by the PANSY at heights from 81–93 km over three summer seasons that zonal (meridional) momentum flux spectra at the summer mesosphere over Syowa Station are mainly positive (negative), and an isolated peak of the momentum fluxes is observed near a period of 12 hour. The sign of momentum flux suggests that gravity waves propagate from low to high latitudes assuming upward energy propagation. Yasui et al. (2016) also suggested that gravity waves in the summer

mesosphere may originate from the tropical convections using the MF radar observation at Syowa Station. Sato et al. (1999) indicated that such meridional propagation of the inertia-gravity waves from the low latitude region and the presence of Jone's critical-level filtering may explain the isolated energy peak near the inertial period (near a period of 12 hour at Syowa Station). The tide-related spontaneous radiation mechanism proposed in this study implies frequent generations of quasi 12 h inertia-gravity waves in the stratosphere and hence may also be responsible to the spectral peak at ~12 h. Further studies are needed to examine many case studies of the tide-related spontaneous radiation events both by the observation and by numerical models.

We have further examined vertical fluxes of zonal and meridional momentum associated with quasi 12 h inertia-gravity waves $\rho_0\overline{u'w'}$ and $\rho_0\overline{v'w'}$. The overbar denotes zonal mean. Figures 3.22a and 3.22b show latitude-height sections of $\rho_0\overline{u'w'}$ and $\rho_0\overline{v'w'}$, respectively, which are averaged for March 19 - 23, 2015. Large negative $\rho_0\overline{u'w'}$ and $\rho_0\overline{v'w'}$ values are distributed at ~40°S in the lower stratosphere. The signs of $\rho_0\overline{u'w'}$ and $\rho_0\overline{v'w'}$ are consistent with parameters estimated from PANSY radar observations and from the numerical simulation. Moreover, the slanted structures of the momentum flux distribution are seen both in $\rho_0\overline{u'w'}$ and $\rho_0\overline{v'w'}$. The structures are quite similar to the propagation path of packet (v) as discussed in Section 4.2. Such a slanted structure is likely formed from the meridional propagation of inertia-gravity waves, which is numerically shown and theoretically discussed by Sato et al. (2009) and Sato et al. (2012) in terms of refraction and advection by the background wind.

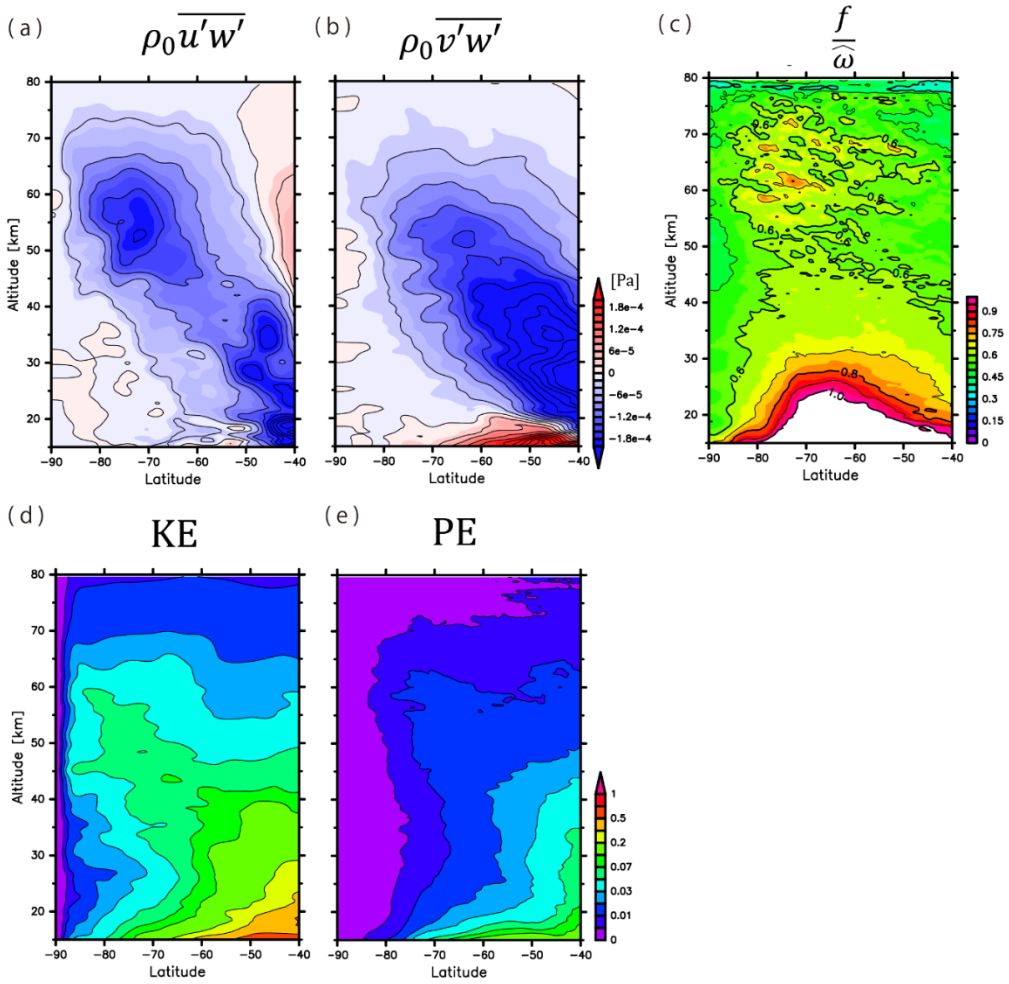

Figure 3.22: Latitude-height cross sections of (a) the vertical fluxes of zonal momentum $\rho_0\overline{u'w'}$, (b) the vertical fluxes of zonal momentum $\rho_0\overline{v'w'}$, (c) the ratio of the Coriolis parameter to the intrinsic frequency $f/\hat{\omega}$, (d) the kinetic energies of the horizontal wind components and (e) the potential energies of the quasi 12 h inertia-gravity waves, which are averaged in the zonal direction and for the period from March 19 to March 21 2015. The contour interval is (a, b) 4.0 $\times$ 10^{-5} [Pa] and (c) 0.1, respectively. It should be noted that the color bar and the contour interval in (d) and (e) are log-scaled. The data is from the NICAM simulation.

Interestingly, large negative $\rho_0\overline{u'w'}$ value is distributed at ~75°S in the mesosphere, showing a negative peak. The latitude-height structure of $\rho_0\overline{u'w'}$ distribution due to small-scale gravity waves does not have such a peak in the mesosphere (not shown). This result suggests that parts of quasi 12 h inertia-gravity waves are generated in the upper

stratosphere as discussed in Section 4.2. In contrast, such a feature is not observed in $\rho_0\overline{v'w'}$, although a small negative local maximum is present at heights of 50 km to 55 km at approximately 60°S. This result implies that wavenumber vectors of inertia-gravity waves in the mesosphere tend to move eastward, consistent with the results of parameter estimation in Section 4.1.

Next, the energy density of the quasi 12 h inertia-gravity waves is examined by dividing the total energy density into three components: horizontal wind kinetic energy ($\overline{KE}$), vertical wind kinetic energy ($\overline{VE}$) and potential energy ($\overline{PE}$):

$$\overline{KE} = \frac{1}{2}\rho_0\left(\overline{u'^2} + \overline{v'^2}\right), \tag{3.18}$$

$$\overline{VE} = \frac{1}{2}\rho_0\overline{w'^2}, \tag{3.19}$$

And

$$\overline{PE} = \frac{1}{2}\rho_0\frac{g^2}{N^2}\overline{\left(\frac{T'}{T}\right)^2}. \tag{3.20}$$

According to the linear theory of hydrostatic inertia-gravity waves, the ratio of $\overline{VE}$ to $\overline{PE}$ has the following relation (from the thermodynamic equation) (e.g., Wang et al., 2005; Geller and Gong 2010, Geller et al., 2013);

$$\frac{\overline{VE}}{\overline{PE}} = \frac{\hat{\omega}^2}{N^2}. \tag{3.21}$$

Thus, $|f/\hat{\omega}|$ can be estimated as follows:

$$\left|\frac{f}{\hat{\omega}}\right| = \left|\frac{f}{N}\right|\sqrt{\frac{\overline{PE}}{\overline{VE}}}. \tag{3.22}$$

Note that these relations (Eq. (3.21) and Eq. (3.22)) is derived based on the assumption of the monochromaticity. Figure 3.22c shows the latitude-height section of $|f/\hat{\omega}|$. In the mesosphere, $|f/\hat{\omega}|$ ranges from 0.6 to 0.8 at ~70°S, which agrees quite well with estimates from the hodograph analysis (Tables 1 and 2). The fact that $|f/\hat{\omega}|$ has higher

values than 0.6 indicates that the quasi 12 h inertia-gravity waves are almost hydrostatic. Note that the value of $|f/\hat{\omega}|$ is larger than 1.0 in the lower stratosphere, which is inconsistent with the linear theory of inertia-gravity waves. This may be explained by the fact that the quasi 12 h inertia-gravity wave components defined in Section 3.4.1 can be contaminated balanced motions such as baroclinic waves in the lower stratosphere.

Figures 3.22d and 3.22e show latitude-height sections of $\overline{KE}$ and $\overline{PE}$ for the quasi 12 h inertia-gravity waves. The slanted structures as observed in Figs. 3.22a and 3.22b are also shown in Figs. 3.22d and 3.22e. It should be noted that the ratio of the Coriolis parameter to the intrinsic frequency $(f/\hat{\omega})$ can also be obtained from $\overline{KE}$ and $\overline{PE}$ as follows:

$$\left|\frac{f}{\hat{\omega}}\right| = \sqrt{\frac{\frac{\overline{KE}}{\overline{PE}} - 1.}{\frac{\overline{KE}}{\overline{PE}} + 1}}. \tag{3.23}$$

It is confirmed that $(f/\hat{\omega})$ values obtained by Eq. (3.23) are consistent with the result obtained from Eq. (3.22) (not shown).

Last, the zonal momentum deposition due to the quasi 12 h inertia-gravity waves is estimated using the wave parameter in Table 2. The zonal pseudomomentum flux is calculated as (Fritts and Alexander, 2003):

$$F_{px} = \bar{\rho} C_{gz} \frac{E}{\hat{\omega}} k = \bar{\rho}\left(1 - \frac{f^2}{\hat{\omega}^2}\right)\overline{u'w'}. \tag{3.24}$$

Moreover, $\overline{u'w'}$ can be also estimated using the wave parameters:

$$\overline{u'w'} = -\frac{k}{m}\overline{{u'}_h{}^2}, \tag{3.24}$$

where ${u'}_h$ is a wind component parallel to the wavenumber vector. When the wave amplitude becomes large enough to satisfy the convective instability limit:

$$a = \left|\frac{{u_h}'}{\hat{c}}\right| \sim 1.0, \tag{3.24}$$

gravity waves break and deposit their energy and momentum at the breaking height. The zonal wind acceleration by the wave breaking is estimated as:

$$X = \frac{1}{\overline{\rho_b}}\left(\frac{F_{px}}{\Delta z}\right), \tag{3.25}$$

where $\overline{\rho_b}$ is the density at the height where the wave breaking occurs and Δz denotes a vertical scale of the wave breaking.

Assuming the scale height of the density is about 7 km and the wave amplitude increases by $1/\sqrt{\rho_0(z)}$ during the vertical propagation, the heights where the packets (i) to (v) breaks were estimated using Eq. (3.24) and the wave parameters in Table 2. Results indicate that the wave breaking of packet (i) to (v) occurs at a height from 70 km to 80 km, which is consistent with the decrease of $\rho_0\overline{u'w'}$ in this height range shown in Fig. 3.22a. Moreover, assuming Δz ~ 3 km which is about one fourth width of the vertical scale of the wave packets (Fig. 3.10), the zonal momentum convergence is estimated by Eq. (3.25) at about 250 m s^{-1} day^{-1} are estimated for packet (i) to (v). This is comparable to or slightly larger than typical gravity wave forcing in the upper mesosphere estimated by general circulation models (e.g., Becker 2012), suggesting that the quasi 12 h inertia-gravity waves are quite important for the momentum balance in the mesosphere. However, other dynamical characteristics such as the intermittency and its longitudinal distribution need to be examined in order to quantitatively understand the contribution of these waves to the zonal momentum balances in the mesosphere.

3.6. Summary

The first observation with a complete system of the PANSY radar were successfully performed for March 16–24, 2015. During this period, large-amplitude disturbances with a period of 12 h in the mesosphere at heights of 70 km to 80 km were detected. Moreover, a numerical simulation for this time period is performed using the NICAM with a model

top of 87 km and with a fine vertical grid spacing. Our main results are summarized as follows:

(1) The observed wave period and vertical wavelength are about 12.3 h and 13.8 km, respectively. The estimated horizontal wavelength is longer than 1100 km. The wavenumber vectors tend to point northeastward or southwestward. A ratio of the Coriolis parameter to the intrinsic frequency ranges from 0.6 to 0.85.

(2) Using the non-hydrostatic numerical model with a model top of 87 km, the disturbances with a period of quasi 12 h in the mesosphere were successfully simulated. It was shown that disturbances with a period of 12 h are not attributable to semi-diurnal migrating tides as considered in many previous studies, but to large-scale inertia-gravity waves with horizontal wavelengths longer than 1400 km. Wavenumber vectors simulated in the NICAM point northeastward. The wave parameters directly estimated using the NICAM agree quite well with those estimated by the PANSY radar observation.

(3) One of quasi 12 h inertia-gravity wave packets is likely generated by the spontaneous radiation mechanism of the mid-latitude upper tropospheric jet. Inertia-gravity waves generated near the mid-latitude tropopause propagate laterally and vertically to the polar mesosphere.

(4) Another quasi 12 h inertia-gravity wave packet is likely generated around the core of the polar night jet. A new spontaneous radiation mechanism associated with the semi-diurnal migrating tides is proposed for such quasi 12 h inertia-gravity waves. The horizontal shear of the background wind including the migrating tides deforms the horizontal wavelength of the

radiated quasi 12 h inertia-gravity waves and let it be much shorter than that of the semi-diurnal migrating tide.

(5) A distribution of vertical fluxes of the zonal and meridional momentum associated with quasi 12 h inertia-gravity waves has a slanted structure from the mid-latitude lower stratosphere to the polar mesosphere, suggesting that quasi 12 h inertia-gravity waves propagate from the mid-latitude lower stratosphere. Moreover, the distribution of the vertical flux of the zonal momentum has a strong negative peak in the mesosphere, suggesting the generation of quasi 12 h inertia-gravity waves in the upper stratosphere.

The present study made a quantitative discussion based on high-resolution observations and numerical models. Statistical analyses of quasi 12 h inertia-gravity waves in the real atmosphere will be of interest as future studies using observations and numerical simulations in the different seasons.

Chapter 4

Gravity wave characteristics in the winter Antarctic mesosphere by a long-term numerical simulation using a non-hydrostatic general circulation model

In this chapter, a long-term simulation using the high-top non-hydrostatic general circulation model is carried out to examine mesospheric gravity waves observed by the PANSY radar in five months from April to August 2016. Successive runs lasting 7 days are made from the MERRA reanalysis data with an overlap of two days between each run. The data for analyses are prepared by extracting the last five days of each simulation. The simulated wind fields are closely compared to the PANSY radar observations and the MERRA reanalysis data. Moreover, statistical characteristics of the mesospheric disturbances simulated by NICAM such as ω spectra of each variable, kinetic and potential energies, momentum and energy fluxes of gravity waves are examined.

本章については、5 年以内に雑誌等で刊行される予定であるため、以降の節について、非公開。

「Gravity wave characteristics in the winter Antarctic mesosphere by a long-term numerical simulation using a non-hydrostatic general circulation model」Atmospheric Chemistry and Physics に投稿予定

Chapter 5

Summary and concluding remarks

本章の一部について、5 年以内に雑誌等で刊行される予定であるため、本章については非公開。

「Gravity wave characteristics in the winter Antarctic mesosphere by a long-term numerical simulation using a non-hydrostatic general circulation model」Atmospheric Chemistry and Physics に投稿予定

Acknowledgements

I would particularly like to express my gratitude to the supervisor Prof. K. Sato. I also thank Profs. M. Satoh, H. Nakamura, K. Iga, T. Hibiya, M. Koike and H. Miura for their many useful comments and discussions. I also thank Prof. T. Sato at Kyoto University and T. Nakamura, M. tsutsumi, Y. Tomikawa and K. Nishimura at National Institute of Polar Research for their useful comments and discussions. I appreciate suggestive comments by Dr. N. Sugimoto at Keio University and Dr. T. Kinoshita at Japan Agency for Marine-earth Science and TECnology. Special thanks are given to colleagues in the atmospheric dynamics laboratory: Dr. M. Kohma, Mr. A. Amemiya, Mr. S. Hirano, Mr. R. Yasui, Mr. Y. Hayashi, Mr. Y. Minamihara, Mr. D. Koshin and Mr. S. Nakajima.

The PANSY multi-institutional project operated by the University of Tokyo and the National Institute of Polar Research (NIPR), and the PANSY radar system was operated by the Japanese Antarctic Research Expedition. All figures shown in this paper were created using the Dennou Club Library (DCL). This study was supported by the Program for Leading Graduate Schools, MEXT, Japan. The study was also supported through the Japan Society for the Promotion of Science (JSPS) Grant-in-Aid Scientific Research (A) 25247075 (Kaoru Sato) and Grant-in-Aid for Research Fellow (26-9257) (Ryosuke Shibuya) programs. This work was partly supported by CREST, JST.

References

Aghedo. A. M., S. Rast and M. G. Schultz, 2010: Sensitivity of tracer transport to model resolution, prescribed meteorology and tracer lifetime in the general circulation model ECHAM5. *Atmos. Chem. Phys.*, **10**, 3385-3396.

Akmaev, R. A., J. M. Forbes, F.-J. Lübken, D. J. Murphy, and J. Höffner, 2016: Tides in the mesopause region over Antarctica: Comparison of whole atmosphere model simulations with ground-based observations, *J. Geophys. Res. Atmos.*, **121**, 1156–1169, doi:10.1002/ 2015JD023673.

Alexander, M. J., and Dunkerton, T. J., 1999: A spectral parameterization of mean-flow forcing due to breaking gravity waves. *Journal of the Atmospheric Sciences*, **56(24)**, 4167-4182.

Alexander, M. J., and C. Barnet, 2007: Using satellite observations to constrain parameterizations of gravity wave effects for global models, *J. Atmos. Sci.*, **64,** 1652-1665.

Alexander, M. J. and Teitelbaum, H., 2007: Observation and analysis of a large amplitude mountain wave event over the Antarctic peninsula. *Journal of Geophysical Research: Atmospheres*, **112(D21)**.

Alexander, M. J., M. Geller, C. McLandress, S. Polavarapu, P. Preusse, F. Sassi, K. Sato, S. Eckermann, M. Ern, A. Hertzog, Y. Kawatani, M. Pulido, T. Shaw, M. Sigmond, R. Vincent, S. Watanabe, 2010: Recent developments in gravity wave effects in climate models, and the global distribution of gravity wave momentum flux from observations and models, *Q. J. Roy. Meteorol. Soc.*, **136**, 1103-1124.

Amemiya, A. and Sato, K., 2016: A new gravity wave parameterization including three-

dimensional propagation. *Journal of the Meteorological Society of Japan. Ser. II*, **94(3)**, 237-256.

Arnold, K. S., and She, C. Y., 2003: Metal fluorescence lidar (light detection and ranging) and the middle atmosphere. *Contemporary Physics*, **44(1)**, 35-49.

Aso, T., 2007: A note on the semidiurnal non-migrating tide at polar latitudes, *Earth Planets Space,* **59**, e21–e24.

Baldwin, M. P., and Coauthors, 2003: The Quasi-Biennial Oscillation, *Rev. Geophys.*, **39,** 179-229.

Baumgaertner, A. J. G., A. J. McDonald, R. E. Hibbins, D. C. Fritts, D. J. Murphy, and R. A. Vincent, 2008: Short-period planetary waves in the Antarctic middle atmosphere, *J. Atmos. Sol. Terr. Phys*., **70(10)**, 1336–1350, doi:10.1016/j.jastp.2008.04.007.

Becker, E., 2009: Sensitivity of the upper mesosphere to the Lorenz energy cycle of the troposphere, *J. Atmos. Sci.*, **66**, 647–666, doi: 10.1175/2008JAS2735.1.

Becker, E., 2012: Dynamical control of the middle atmosphere. *Space Sci. Rev.*, 168, 283–314, doi:10.1007/s11214-011-9841-5.

Beres, J. H., Alexander, M. J. and Holton, J. R., 2004: A method of specifying the gravity wave spectrum above convection based on latent heating properties and background wind. *Journal of the atmospheric sciences*, **61(3)**, 324-337.

Blackman, R. B., and J. W. Tukey, 1958: *The Measurement of Power Spectra from the Point of View of Communications Engineering*, Dover,New York.

Bloom, S., L. Takacs, A. DaSilva, and D. Ledvina, 1996: Data assimilation using incremental analysis updates. *Mon. Wea. Rev.*, **124**, 1256–1271.

Butchart, N., et al., 2010: Chemistry–climate model simulations of twenty-first century

stratospheric climate and circulation changes. *Journal of Climate, 23*(20), 5349-5374.

Butchart, N., et al., 2011: Multimodel climate and variability of the stratosphere, *J. Geophys. Res.*, **116**, D05102, doi:10.1029/2010JD014995.

Bühler, O., and M. E. McIntyre, 2005: Wave capture and wave-vortex duality. *J. Fluid. Mech.,* **534,** 67-95.

Cámara, A., Lott, F. and Hertzog, A., 2014: Intermittency in a stochastic parameterization of nonorographic gravity waves. *Journal of Geophysical Research: Atmospheres,* **119(21)**.

Charron, M. and Manzini, E., 2002: Gravity waves from fronts: Parameterization and middle atmosphere response in a general circulation model. *Journal of the atmospheric sciences*, **59(5)**, 923-941.

Chen, C., X. Chu, A. J. McDonald, S. L. Vadas, Z. Yu, W. Fong, and X. Lu, 2013: Inertia‐gravity waves in Antarctica: A case study using simultaneous lidar and radar measurements at McMurdo/Scott Base (77.8° S, 166.7° E). *Journal of Geophysical Research: Atmospheres*, **118**(7), 2794-2808.

Cherniak I and I. Zakharenkova, 2016: High-latitude ionospheric irregularities: differences between ground- and space-based GPS measurements during the 2015 St. Patrick's Day Storm. Earth Planets Space 68:136. doi:10.1186/s40623-016-0506-1

Chu, X., W. Huang, F. Fong, Z. Yu, Z. Wang, J. A. Smith, and C. S. Gardner, 2011: First lidar observations of polar mesospheric clouds and Fe temperatures at McMurdo (77.8°S, 166.7°E), Antarctica, *Geophys. Res. Lett.*, **38**, L16810, doi:10.1029/2011GL048373.

Cohen, N. Y., E. P. Gerber and O. Bühler, E. P., 2013: Compensation between resolved and unresolved wave driving in the stratosphere: Implications for downward control. *Journal of the Atmospheric Sciences*, **70(12)**, 3780-3798.

Cohen, N. Y., Gerber, E. P. and Bühler, O., 2014: What drives the Brewer–Dobson circulation?. *Journal of the Atmospheric Sciences*, **71(10)**, 3837-3855.

Collins, R. L., D. C. Senft, and C. S. Gardner, 1992: Observations of a 12 H wave in the mesopause region at the South Pole, *Geophys. Res. Lett.*, **19**(1), 57–60, doi:10.1029/91GL02780.

Dowdy, A. J., R. A. Vincent, M. Tsutsumi, K. Igarashi, Y. Murayama, W. Singer, and D. J. Murphy, 2007: Polar mesosphere and lower thermosphere dynamics: 1. Mean wind and gravity wave climatologies, *J. Geophys. Res.*, **112**, D17104, doi:10.1029/2006JD008126.

Durran, D.R. 1990. Mountain waves and downslope winds. *In*: Atmospheric Processes over Complex Terrain. W. Blumen, (Ed), *Meteorol. Monogr. Am. Meteorol. Soc.* **23 (45)**: 59–81.

Eckermann, S. D., and P. Preusse, 1999: Global measurements of stratospheric mountain waves from space, *Science*, **286**, 1534–1537.

Eckermann, S. D., and C. J. Marks, 1996: An idealized ray model of gravity wave-tidal interactions, *J. Geophys. Res.*, **101(D16)**, 21195–21212, doi:10.1029/96JD01660.

Ern, M., Preusse, P., Alexander, M. J., & Warner, C. D., 2004: Absolute values of gravity wave momentum flux derived from satellite data. *Journal of Geophysical Research: Atmospheres*, **109(D20)**.

Ern, M., P. Preusse, J. C. Gille, C. L. Hepplewhite, M. G. Mlynczak, J. M. Russell III, and M. Riese, 2011: Implications for atmospheric dynamics derived from global

observations of gravity wave momentum flux in stratosphere and mesosphere. *J. Geophys. Res.*, **116**, D19107, doi:10.1029/2011JD015821.

Eyring, V., T. G. Shepherd, and D. W. Waugh, Eds., 2010: SPARC CCMVal report on the evaluation of chemistry-climate models. *SPARC Rep.*, **5**, WCRP-132, WMO/TD-No. 1526, 434 pp.

Fetzer, E. J., and J. C. Gille, 1994: Gravity wave variance in LIMS temperatures, part I, Variability and comparison with background winds, *J. Atmos. Sci.*, **51**, 2461–2483.

Fetzer, E. J., and J. C. Gille, 1996: Gravity wave variance in LIMS temperatures, part II, Comparison with the zonal-mean momentum balance, *J. Atmos. Sci.*, **53**, 398–410.

Fisher, G. M., R. J, Niciejewski, T. L. Killeen, W. A. Gault, G. G. Shepherd, S. Brown, and Q. Wu, 2002: Twelve‐hour tides in the winter northern polar mesosphere and lower thermosphere. *Journal of Geophysical Research: Space Physics*, **107**(A8).

Fraser, G. J. and U. Khan, 1990: Semidiurnal variations in the time scale of irregularities near the Antarctic summer mesopause. *Radio science*, **25**(5), 997-1003.

Forbes, J. M., N. A. Makarov, and Y. I. Portnyagin, 1995: First results from the meteor radar at south pole: A large 12-hour oscillation with zonal wavenumber one, *Geophys. Res. Lett.*, **22,** 3247– 3250.

Forbes, J. M., Y. I. Portnyagin, N. A. Markov, S. E. Palo, E. G. Merzlyakov and X. Zhang, 1999: Dynamics of the lower thermosphere over South Pole from meteor radar windmeasurements. *Earth Planets Space,* **51**, 611–620.

Fritts, D. C., & Vincent, R. A., 1987: Mesospheric momentum flux studies at Adelaide, Australia: Observations and a gravity wave–tidal interaction model. *Journal of the Atmospheric Sciences*, **44(3)**, 605-619.

Fritts, D. C., D. M. Riggin, B. B. Balsley, and R. G. Stockwell, 1998: Recent results with an MF radar at McMurdo, Antarctica: Characteristics and variability of motions near 12-hour period in the mesosphere, *Geophys. Res. Lett.*, **25**(3), 297–300, doi:10.1029/97GL03702.

Fritts, D. C., 2000: Errant inferences of gravity wave momentum and heat fluxes using airglow and lidar instrumentation: Corrections and cautions. *Journal of Geophysical Research: Atmospheres*, **105(D17)**, 22355-22360.

Fritts , D. C. and M. J. Alexander, 2003: Gravity wave dynamics and effects in the middle atmosphere. *Rev. Geophys.*, **41**, 1003, doi:10.1029/2001RG000106.

Fritts and Coauthors, 2016: The Deep Propagating Gravity Wave Experiment (DEEPWAVE): An airborne and ground-based exploration of gravity wave propagation and effects from their sources throughout the lower and middle atmosphere. *Bull. Amer. Meteor. Soc*., doi:10.1175, **97(3)**, 425-453, doi:10.1175/BAMS-D-14-00269.1.

Garcia, R. R., T. J. Dunkerton, R. S. Lieberman, and R. A. Vincent (1997), Climatology of the semiannual oscillation of the tropical middle atmosphere, *J. Geophys. Res*., **102(D22)**, 26019–26032, doi:10.1029/97JD00207.

Garcia, F. J., M. C. Kelley, J. J. Makela, and C.-S. Huang,2000: Airglow observations of mesoscale low-velocity traveling ionospheric disturbances at midlatitudes, *J. Geophys. Res.*, **105(A8)**, 18407–18415, doi:10.1029/1999JA000305.

Gardner, C. S., T. J. Kane, D. C. Senft, J. Qian, and G. C. Papen, 1993: Simultaneous observations of sporadic *E*, Na, Fe, and Ca^+ layers at Urbana, Illinois: Three case studies, *J. Geophys. Res.*, **98(D9**), 16865–16873, doi:10.1029/93JD01477.

Geller, M. A. and J. Gong, 2010: Gravity wave kinetic, potential, and vertical

fluctuation energies as indicators of different frequency gravity waves. *Journal of Geophysical Research: Atmospheres*, **115**(D11).

Geller, M. A., M. Alexander, P. T. Love, J. Bacmeister, M. Ern, A. Hertzog, T. Zhou, 2013: A Comparison between Gravity Wave Momentum Fluxes in Observations and Climate Models. *Journal of Climate*, **26**(17).

Gille, J., and Coauthors, 2008: High Resolution Dynamics Limb Sounder: Experiment overview, recovery, and validation of initial temperature data. *J. Geophys. Res.*, **113,** D16S43, doi:10.1029/2007JD008824.

Guest, F. M., M. J. Reeder, C. J. Marks, and D. J. Karoly, 2000: Inertia-gravity waves observed in the lower stratosphere over Macquarie Island, *J. Atmos. Sci.*, **57**, 737–752.

Hagan, M. E., and J. M. Forbes, 2003: Migrating and nonmigrating semidiurnal tides in the upper atmosphere excited by tropospheric latent heat release, *J. Geophys. Res.*, **108(A2)**, 1062, doi:10.1029/2002JA009466.

Hamilton, K., 1991: Climatological statistics of stratospheric intertiagravity waves deduced from historical rocketsonde wind and temperature data, *J. Geophys. Res.*, **96**, 20,831–20,839.

Haynes, P. H., 1998: The latitudinal structure of the quasi-biennial oscillation. *Quart. J. Roy. Meteor. Soc.*, **124,** 2645-2670.

Heikes, R. and D. A. Randall, 1995: Numerical integration of the shallow-water equations on a twisted icosahedral grid. Part I: Basic design and results of tests. *Mon. Wea. Rev.*, **123**, 1862-1880.

Hernandez, G., G. J. Fraser, and R. W. Smith, 1993: Mesospheric 12-hour oscillation near South Pole, Antarctica, *Geophys. Res. Lett.*, **20**(17), 1787–1790,

doi:10.1029/93GL01983.

Hertzog, A., G. Boccara, R. A. Vincent, F. Vial, and P. Cocquerez, 2008: Estimation of gravity wave momentum flux and phase speeds from quasi-Lagrangian stratospheric balloon flights. Part II: Results from the Vorcore campaign in Antarctica. *Journal of the Atmospheric Sciences*, **65**(10), 3056-3070.

Hibbins, R. E., O. J. Marsh, A. J. McDonald, and M. J. Jarvis, 2010: A new perspective on the longitudinal variability of the semidiurnal tide, *Geophys. Res. Lett.*, **37**, L14804, doi:10.1029/2010GL044015.

Hibbins, R.E., Espy, P.J., Jarvis, M.J., Riggin, D.M., Fritts, D.C., 2007. A climatology of tides and gravity wave variance in the MLT above Rothera, Antarctica obtained by MFradar. *J. Atmos. Solar-Terr. Phys*. **69 (4–5)**, 578–588.

Hindley, N. P., Wright, C. J., Smith, N. D. and Mitchell, N. J. (2015). The southern stratospheric gravity wave hot spot: individual waves and their momentum fluxes measured by COSMIC GPS-RO. *Atmospheric Chemistry and Physics*, *15*(14), 7797-7818.

Hines, C. O., 1997: Doppler-spread parameterization of gravity-wave momentum deposition in the middle atmosphere. Part 1: Basic formulation. *Journal of Atmospheric and Solar-Terrestrial Physics*, **59(4)**, 371-386.

Hitchman, M. H., Gille, J. C., Rodgers, C. D., and Brasseur, G., 1989: The separated polar winter stratopause: A gravity wave driven climatological feature. *Journal of the atmospheric sciences*, **46(3)**, 410-422.

Hirota, I. and T. Niki, 1986: Inertia-gravity waves in the troposphere and stratosphere observed by the MU radar. *J. Meteor. Soc. Japan*, **64**, 995−999.

Hoffmann, L., Xue, X., and Alexander, M. J., 2013: A global view of stratospheric

gravity wave hotspots located with Atmospheric Infrared Sounder observations, *J. Geophys. Res.-Atmos.*, **118**, 416–434, doi:10.1029/2012JD018658.

Holton, J. R. and M.J. Alexander. 1999: Gravity waves in the mesosphere generated by tropospheric convection. *Tellus*, **51A-B**: 45–58.

Hook, J. L., 1970: Winds at the 75–110 km level at College, Alaska, *Planetary Space Science*, **18**, 1623-1638

Iga, S., 2015: Smooth, seamless, and structured grid generation with flexibility in resolution distribution on a sphere based on conformal mapping and the spring dynamics method. *J. Comp. Phys.*, **297**, 381-406.

Jacobsen, K. S., and M. Dähnn, 2014: Statistics of ionospheric disturbances and their correlation with GNSS 338 positioning errors at high latitudes, *J. Space Weather Space Clim.*, **4**, A27, doi:10.1051/swsc/2014024.

Jiang, J. H., Eckermann, S. D., Wu, D. L., Hocke, K., Wang, B., Ma, J., and Zhang, Y., 2005: Seasonal variation of gravity wave sources from satellite observation. *Advances in Space Research*, **35(11)**, 1925-1932.

Kataoka, R., D. Shiota, E. Kilpua, and K. Keika, 2015: Pileup accident hypothesis of magnetic storm on 17 March 2015, *Geophys. Res. Lett.*, **42**, 5155–5161, doi:10.1002/2015GL064816.

Kawatani, Y. and Hamilton, K., 2013: Weakened stratospheric quasibiennial oscillation driven by increased tropical mean upwelling. *Nature*, **497(7450)**, 478.

K-1 Model Developers, 2004: K-1 coupled GCM (MIROC) description, *K-1 Tech. Rep.*, 1, pp. 1 –34, Univ. of Tokyo, Tokyo, Japan.

Kim, Y.-J., S. Eckermann, and H.-Y. Chun, 2003: An overview of the past, present and future of gravity-wave drag parametrization for numerical climate and weather

prediction models. *Atmos.–Ocean*, **41**, 65–98, doi:10.3137/ao.410105.

Kirkwood, S., 2007: Polar mesosphere winter echoes: A review of recent results, *Adv. Space Res.*, **40**, 751–757, doi:10.1016/j.asr.2007.01.024.

Kitamura, Y., and I. Hirota, 1989: Small-scale disturbances in the lower stratosphere revealed by daily rawin sonde observations, *J. Meteorol. Soc. Jpn.*, **67,** 817–830.

Kohma, M. and K. Sato, 2011: The effects of atmospheric waves on the amounts of polar stratospheric clouds. *Atmos. Chem. Phys.*, **11**, 11535-11552, doi:10.5194/acp-11-11535-2011.

Kovalam, S., and R. A. Vincent, 2003: Intradiurnal wind variations in the midlatitude and high-latitude mesosphere and lower thermosphere, *J. Geophys. Res.*, **108**, 4135, doi:10.1029/2002JD002500, D4.

Lane, T. P., J. D. Doyle, R. Plougonven, M. A. Shapiro, and R. D. Sharman, 2004: Observations and numerical simulations of inertia-gravity waves and shearing instabilities in the vicinity of a jet stream. *J. Atmos. Sci.*, **61,** 2792-2706.

Leovy, C., 1964: Radiative equilibrium of the mesosphere. *Journal of the Atmospheric Sciences*, **21(3)**, 238-248.

Li, T., C.-Y. She, H.-L. Liu, T. Leblanc, and I. S. McDermid, 2007: Sodium lidar–observed strong inertia-gravity wave activities in the mesopause region over Fort Collins, Colorado (41°N, 105°W), *J. Geophys. Res.*, **112**, D22104, doi:10.1029/2007JD008681.

Liu, H. L., J. M. McInerney, S. Santos, P. H. Lauritzen, M. A. Taylor, and N. M. Pedatella, 2014: Gravity waves simulated by high‐resolution Whole Atmosphere Community Climate Model. *Geophysical Research Letters*, **41(24)**, 9106-9112.

López-Valverde, M. A., D. P. Edwards, M. López-Puertas, and C. Roldán, 1998: Non-

local thermodynamic equilibrium in general circulation models of the Martian atmosphere 1. Effects of the local thermodynamic equilibrium approximation on thermal cooling and solar heating, *J. Geophys. Res.*, **103(E7)**, 16799–16811, doi:10.1029/98JE01601.

Lu, X., A. Z. Liu, G. R. Swenson, T. Li, T. Leblanc, and I. S. McDermid, 2009: Gravity wave propagation and dissipation from the stratosphere to the lower thermosphere, *J. Geophys. Res.*, **114**, D11101, doi:10.1029/2008JD010112.

Manson , A. H., 1990: Gravity wave horizontal and vertical wave lengths; An update of measurements in the mesopause region ˜ 80-100 km, *J. Atmos. Sci.*, **47**, 2765– 2773.

Manzini, E., M. A. Giorgetta, M. Esch, L. Kornblueh, and E. Roeckner, 2006: The influence of sea surface temperatures on the northern winter stratosphere: Ensemble simulations with the MAECHAM5 model. *J. Climate*, **19**,3863–3881.

Matsuda, T. S., T. Nakamura, M. K. Ejiri, M. Tsutsumi, and K. Shiokawa, 2014: New statistical analysis of the horizontal phase velocity distribution of gravity waves observed by airglow imaging, *J. Geophys. Res. Atmos.*, **119**, 9707–9718, doi:10.1002/2014JD021543.

Mayr, H. G., J. G. Mengel, E. R. Talaat, H. S. Porter, and K. L. Chan, 2005a: Mesospheric non-migrating tides generated with planetary waves: I. Characteristics, *J. Atmos. Sol. Terr. Phys.*, **67**, 959– 980.

Mayr, H. G., J. G. Mengel, E. R. Talaat, H. S. Porter, and K. L. Chan, 2005b: Mesospheric non-migrating tides generated with planetary waves: II. Influence of gravity waves, *J. Atmos. Sol. Terr. Phys.*, **67**, 981–991.

McDonald, A. J., S. E. George, and R. M. Woollands, 2009: Can gravity waves

significantly impact PSC occurrence in the Antarctic?, *Atmos. Chem. Phys.*, **9**, 8825–8840, doi:10.5194/acp-9-8825-2009.

McFarlane, N. A.,1987: The effect of orographically excited gravity wave drag on the general circulation of the lower stratosphere and troposphere. *Journal of the atmospheric sciences*, **44(14)**, 1775-1800.

McLandress, C., T. G. Shepherd, S. Polavarau, S. R. Beagley, 2012: Is Missing Orographic Gravity Wave Drag near 60°S the Cause of the Stratospheric Zonal Wind Biases in Chemistry–Climate Models?. *J. Atmos. Sci.,* **69**, 802–818, 2012.

McFarlane, N. A., 1987: The effect of orographically excited wave drag on the general circulation of the lower stratosphere and troposphere. *J. Atmos. Sci.*, **44**, 1775–1800.

McIntyre, M. E., 2009: Spontaneous imbalance and hybrid vortex–gravity structures. *Journal of the Atmospheric Sciences*, **66(5)**, 1315-1326.

McKinnell, L.-A., and M. Friedrich, 2007: A neural network-based ionospheric model for the auroral zone, *J. Atmos. Sol. Terr. Phys.*,**69**, 1459–1470, doi:10.1016/j.jastp.2007.05.003.

Mihalikova, M., Sato, K., Tsutsumi, M., and Sato, T, 2016.: Properties of inertia-gravity waves in the lowermost stratosphere as observed by the PANSY radar over Syowa Station in the Antarctic, *Ann. Geophys.*, **34**, 543-555, doi:10.5194/angeo-34-543-2016.

Miyakawa, T., M. Satoh, H. Miura, H. Tomita, H. Yashiro, A. T. Noda, Y. Yamada, C. Kodama, M. Kimoto and K. Yoneyama, 2014: Madden-Julian Oscillation prediction skill of a new-generation global model. *Nature Commun.*, **5**, 3769.

Miura, H. and M. Kimoto, 2005: A comparison of grid quality of optimized spherical

hexagonal-pentagonal geodesic grids. *Mon. Wea. Rev.*, **133**, 2817-2833.

Moffat-Griffin, T., M. J. Jarvis, S. R. Colwell, A. J. Kavanagh, G. L. Manney, and W. H. Daffer, 2013: Seasonal variations in the lower stratospheric gravity wave energy above the Falkland Islands, *J. Geophys. Res. Atmos*., **118**, 10,861–10,869, doi:10.1002/jgrd.50859.

Muraoka, Y., S. Fukao, T. Sugiyama, M. Yamamoto, T. Nakamura, T. Tsuda, and S. Kato, 1990: Frequency-spectra of mesospheric wind fluctuations observed with the MU radar, *Geophys. Res. Lett.*, **17(11)**, 1897–1900, doi:10.1029/Gl017i011p01897.

Murphy, D. J., et al., 2006: A climatology of tides in the Antarctic mesosphere and lower thermosphere, *J. Geophys. Res*., **111**, doi:10.1029/2005JD006803.

Murphy, D.J., French, W.J.R., Vincent, R.A., 2007. Long-Period Planetary Waves in the mesosphere and lower thermosphere above Davis, Antarctica. *Journal of Atmospheric and Solar-Terrestrial Physics*, doi:10.1016/j.jastp.2007.06.008.

Murphy, D. J., T. Aso, D. C. Fritts, R. E. Hibbins, A. J. McDonald, D. M. Riggin, M. Tsutsumi, and R. A. Vincent, 2009: Source regions for Antarctic MLT non-migrating semidiurnal tides, *Geophys. Res. Lett*., **36**, L09805, doi:10.1029/2008GL037064.

Murphy, D. J., S. P. Alexander, A. R. Klekociuk, P. T. Love, and R. A. Vincent, 2014: Radiosonde observations of gravity waves in the lower stratosphere over Davis, Antarctica. *J. Geophys. Res. Atmos.*, **119**, 11 973–11 996, doi:10.1002/ 2014JD022448.

Nakamura, T., T. Tsuda, M. Yamamoto, S. Fukao, and S. Kato, 1993: Characteristics of gravity waves in the mesosphere observed with the middle and upper atmosphere

radar 2. Propagation direction, *J. Geophys. Res.*, **98**(D5), 8911–8923, doi:10.1029/92JD03030.

Nakanishi M. and H. Niino, 2004: An Improved Mellor–Yamada Level-3 Model with Condensation Physics: Its Design and Verification. *Boundary-Layer Meteorol.* **112**,1–31.

Nastrom, G. D., and F. D. Eaton, 2006: Quasi-monochromatic inertiagravity waves in the lower stratosphere from MST radar observations, *J. Geophys. Res.*, **111**, D19103, doi:10.1029/2006JD007335.

Nasuno, T., 2013: Forecast skill of Madden-Julian Oscillation events in a global nonhydrostatic model during the CINDY2011/DYNAMO observation period, *SOLA*, **9**, 69-73.

Neale, R. B., and Coauthors, 2010: Description of the NCAR Community Atmospheric Model (CAM 4.0). *NCAR Tech. Note*, **485**, 212 pp.

Nicolls, M. J., R. H. Varney, S. L. Vadas, P. A. Stamus, C. J. Heinselman, R. B. Cosgrove, and M. C. Kelley, 2010:, Influence of an inertia-gravity wave on mesospheric dynamics: A case study with the Poker Flat Incoherent Scatter Radar, *J. Geophys. Res.*, **115**, D00N02, doi:10.1029/2010JD014042.

Nozawa, T., T. Nagashima, T. Ogura, T. Yokohata, N. Okada, and H. Shiogama, 2007: Climate change simulations with a coupled ocean-atmosphere GCM called the Model for Interdisciplinary Research on Climate: MIROC, *CGER Supercomput. Monogr. Rep.*, 12, Cent. For Global Environ. Res., Natl. Inst. for Environ. Stud., Tsukuba, Japan.

Okamoto, K., K. Sato, and H. Akiyoshi, 2011: A study on the formation and trend of the Brewer-Dobson circulation. *J. Geophys. Res.*, **116,** D10117,

doi:10.1029/2010JD014953.

O'Sullivan, D. J., and T. J. Dunkerton, 1995: Generation of inertia-gravity waves in a simulated life cycle of baroclinic instability. *J. Atmos. Sci.*, **52,** 3695-3716.

Pavelin, E. G., J. A. Whiteway, and G. Vaughan, Observation of gravity wave generation and breaking in the lowermost stratosphere, 2001: *J. Geophys. Re*s., **106**, 5173 – 5179.

Plougonven, R., and C. Snyder, 2007: Inertia-gravity waves spontaneously generated by jets and fronts. Part I: Different baroclinic life cycles. *J. Atmos. Sci.*, **64**, p2502-2520.

Plougonven, R., A. Hertzog and L. Guez, 2013: Gravity waves over Antarctica and the Southern Ocean: consistent momentum fluxes in mesoscale simulations and stratospheric balloon observations. *Quarterly J. Roy. Meteor. Soc.*, **139**, 101-118.

Plumb, R. A., 2002: Stratospheric transport. *J. Meteor. Soc. Japan*, **80,** 793-809.

Portnyagin, Y. I., J. M. Forbes, N. A. Makarov, E. G. Merzlyakov, and S.Palo, 1998: The summertime 12-h wind oscillation with zonal wavenumber s =1 in the lower thermosphere over the South Pole, *Ann. Geophys.*, **16**,828– 837.

Preusse, P., Schaeler, B., Bacmeister, J. T., & Offermann, D., 1999: Evidence for gravity waves in CRISTA temperatures. *Advances in Space Research*, **24(11)**, 1601-1604.

Preusse, P., S. D. Eckermann, M. Ern, J. Oberheide, R. H. Picard, R. G. Roble, M. Riese, J. M. Russell, III, and M. G. Mlynczak, 2009: Global ray tracing simulations of the SABER gravity wave climatology, *J. Geophys. Res.*, **114**, D08126, doi:10.1029/2008JD011214.

Rapp, M., and F. J. Lübken, 2003: On the nature of PMSE: Electron diffusion in the vicinity of charged particles revisited, *J. Geophys. Res.*,**108(D8)**, 8437,

doi:10.1029/2002JD002857.

Rapp, M., I. Strelnikova, R. Latteck, P. Hoffmann, U. P. Hoppe, I. Haggstrom, and M. T. Rietveld, 2008: Polar mesosphere summer echoes (PMSE) studied at Bragg wavelengths of 2.8 m, 67 cm, and 16 cm, *J. Atmos. Sol. Terr. Phys.*, **70(7)**, 947–961, doi:10.1016/j.jastp.2007.11.005.

Reid, I. M., and R. A. Vincent, 1987: Measurements ofmesospheric gravity wave momentum fluxes and mean flow accelerations at Adelaide, Australia, *J. Atmos. Terrest. Phys*. **49**, 443-460.

Richter, J. H., F. Sassi, and R. R. Garcia, 2010: Toward a physically based gravity wave source parameterization in a general circulation model, *J. Atmos. Sci.*, **67**, 136–156.

Rienecker, M., and Coauthors, 2011: MERRA: NASA's ModernEra Retrospective Analysis for Research and Applications. *J. Climate*, **24**, 3648–3624.

Riggin, D. M., D. C. Fritts, M. J. Jarvis, G. O. L. Jones, 1999: Spatial structure of the 12-hour wave in the Antarctic as observed by radar. *Earth Planets and Space*, **51**, 621–628.

Sadourny, R., A. Arakawa and Y. Mintz, 1968: Integration of the nondivergent barotropic vorticity equation with an icosahedral-hexiagonal grid for the sphere. *Mon. Wea. Rev.*, **96**, 351–356.

Sato, K. 1990: Vertical wind disturbances in the troposphere and lower stratosphere observed by the MU radar, *J. Atmos. Sci.*, **47,** 2803-2817.

Sato, K., 1994: A statistical study of the structure, saturation and sources of inertio-gravity waves in the lower stratosphere observed with the MU radar. *J. Atmos. Terr. Phys.*, **56,** 755-774.

Sato, K., T. Kinoshita, and K. Okamoto, 2013: A new method to estimate three-

dimensional residual mean circulation in the middle atmosphere and its application to gravity-wave resolving general circulation model data, *J. Atmos. Sci.,* **70**, 3756–3779. doi: http://dx.doi.org/10.1175/JAS-D-12-0352.1.

Sato, K., D. J. O'Sullivan, and T. J. Dunkerton, 1997: Low-frequency inertia-gravity waves in the stratosphere revealed by three-weak continuous observation with the MU radar. *Geophys. Res. Lett.,* **24,** 1739-1742.

Sato, K., and T. J. Dunkerton, 1997: Estimates of momentum flux associated with equatorial Kelvin and gravity waves. *J. Geophys. Res.,* **102**, 26,247-26,261.

Sato, K., K. Yamada, and I. Hirota, 2000:Global characteristics of medium-scale tropopausal waves observed in ECMWF operational data, *Mon. Wea. Rev.,* **128,** No.11, 3808-3823.

Sato, K., M. Tsutsumi, T. Sato, T. Nakamura, A. Saito, Y. Tomikawa, K. Nishimura, M. Kohma, H. Yamagishi, and T. Yamanouchi, 2014: Program of the Antarctic Syowa MST/IS Radar (PANSY), *J. Atmos. Solar-Terr. Phys*., **118A**, 2-15.

Sato, K., S. Watanabe, Y. Kawatani, Y. Tomikawa, K. Miyazaki, and M. Takahashi, 2009: On the origins of mesospheric gravity waves, *Geophys. Res. Lett.,* **36,** L19801, doi:10.1029/2009GL039908.

Sato, K., S. Tateno S. Watanabe, and Y. Kawatani, 2012: Gravity wave characteristics in the Southern Hemisphere revealed by a high-resolution middle-atmosphere general circulation model. *J. Atmos. Sci.,* **69**, 1378–1396, doi:10.1175/JAS-D-11-0101.1.

Sato, K., and M. Yoshiki, 2008: Gravity wave generation around the polar vortex in the stratosphere revealed y 3-houly radiosonde observations at Syowa Station. *J. Atmos. Sci.,* **65,** 3719-3735.

Sato, K., and M. Yamada, 1994: Vertical structure of atmospheric gravity waves

revealed by the wavelet analysis. *Journal of Geophysical Research: Atmospheres (1984–2012)*, **99**(D10), 20623-20631.

Sato, K., M. Kohma, M. Tsutsumi, and T. Sato, 2017: Frequency spectra and vertical profiles of wind fluctuations in the summer Antarctic mesosphere revealed by MST radar observations. *Journal of Geophysical Research: Atmospheres* **122**:1, 3-19.

Satoh, M., T. Matsuno, H. Tomita, H. Miura, T. Nasuno, and S. Iga, 2008: Nonhydrostatic icosahedral atmospheric model (NICAM) for global cloud resolving simulations. *J. Comput. Phys.*, the special issue of Predicting Weather, Climate and Extreme Events, **227**, 3486−3514, doi: 10.1016/j.jcp.2007.02.006.

Satoh, M., Tomita, H., Yashiro, H., Miura, H., Kodama, C., Seiki, T., Noda, A. T., Yamada, Y., Goto, D., Sawada, M., Miyoshi, T., Niwa, Y., Hara, M., Ohno, T., Iga, S., Arakawa, T., Inoue, T., Kubokawa, H., 2014: The Non-hydrostatic Icosahedral Atmospheric Model: Description and Development. *Progress in Earth and Planetary Science,* 1, **18**. doi:10.1186/s40645-014-0018-1

Scinocca, J. F., 2003: An accurate spectral nonorographic gravity wave drag parameterization for general circulation models. *J. Atmos. Sci.*, **60,** 667-682.

Schmidt, G. A., and Coauthors, 2006: Present-day atmospheric simulations using GISS ModelE: Comparison to in situ, satellite, and reanalysis data. *J. Climate*, **19**, 153–192.

Shepherd, T. G., 2014: Atmospheric circulation as a source of uncertainty in climate change projections. *Nature Geoscience*, **7(10)**, 703.

Shibata, T., K. Sato, H. Kobayashi, M. Yabuki, and M. Shiobara, 2003: The Antarctic polar stratospheric clouds under the temperature perturbation by nonorogaphic inertia-gravity waves observed by micropulse lidar. *J. Geophys. Res.*, **108,** 4105,

doi:10.1029/2002JD002713.

Shibuya R., H. Miura and K. Sato, 2016: A grid transformation method for a quasi-uniform, circular fine region using the spring dynamic, *Journal of the Meteorological Society of Japan*, 94, doi:10.2151/jmsj.2016-022.

Shibuya, R., K. Sato, Y. Tomikawa, M. Tsutsumi and T. Sato, 2015: A study of multiple tropopause structures caused by inertia-gravity waves in the Antarctica, *J. Atmos. Sci.*, **72**, 2109–2130.

Shibuya R., K. Sato, M. Tsutsumi, T. Sato, Y. Tomikawa, K. Nishimura, and M. Kohma, 2017: Quasi-12h inertia-gravity waves in the lower mesosphere observed by the PANSY radar at Syowa Station (39.6 °E ,69.0 °S), *Atmos. Chem. Phys.*, **17**, 6455-6476, doi:10.5194/acp-17-6455-2017.

Shine, K. P.,1987: The middle atmosphere in the absence of dynamical heat fluxes. *Quarterly Journal of the Royal Meteorological Society*, **113(476)**, 603-633.

Sigmond, M. and Shepherd, T. G.,2014: Compensation between resolved wave driving and parameterized orographic gravity wave driving of the Brewer–Dobson circulation and its response to climate change. *Journal of Climate*, **27(14)**, 5601-5610.

Song, I. S. and Chun, H. Y., 2005: Momentum flux spectrum of convectively forced internal gravity waves and its application to gravity wave drag parameterization. Part I: Theory. *Journal of the atmospheric sciences*, **62(1)**, 107-124.

Song, I. S. and Chun, H. Y., 2008: A Lagrangian spectral parameterization of gravity wave drag induced by cumulus convection. *Journal of the Atmospheric Sciences*, **65(4)**, 1204-1224.

Stolarski, R. S., A. R. Douglass, M. Gupta, P. A. Newman, S. Pawson, M. R. Schoeberl,

and J. E. Nielsen, 2006: An ozone increase in the Antarctic summer stratosphere: A dynamical response to the ozone hole. *Geophys. Res. Lett.*, **33,** L21805, doi:10.1029/2006GL026820.

Sugimoto, N., and R. Plougonven, 2016: Generation and backreaction of spontaneously emitted inertia-gravity waves, *Geophys. Res. Lett.*, **43**, 3519–3525, doi:10.1002/2016GL068219.

Talaat, E. R., and H.G. Mayr, 2011: Model of semidiurnal pseudo tide in the high-latitude upper mesosphere, *Journal of Atmospheric and Solar-Terrestrial Physics*, **73**, 2386–2391.

Theon, J. S., W. Nordberg, L. B. Katchen and J. J. Horbath, 1967*:* Some observations on the thermal behavior of the mesosphere, *J. Atmos. Sci*., **24,** 428–438.

Tomikawa, Y., K. Sato, S. Watanabe, Y. Kawatani, K. Miyazaki, and M. Takahashi, 2012: Growth of planetary waves and the formation of an elevated stratopause after a major stratospheric sudden warming in a T213L256 GCM, *J. Geophys. Res.*,**117,** D16101, doi:10.1029/2011JD017243.

Tomikawa, Y., and K. Sato, 2003: Trapped waves in the edge region of stratospheric polar vortices, *J. Geophys. Res.,* **108(D2),** 4047, doi:1029/2002JD002579.

Tomita, H., M. Tsugawa, M. Satoh and K. Goto, 2001: Shallow water model on a modified icosahedral geodesic grid by using spring dynamics. *J. Comp. Phys.*, **174**, 579-613.

Tomita, H., M. Satoh and K. Goto, 2002: An optimization of icosahedral grid by using spring dynamics. *J. Comp. Phys.*, **183**, 307-331.

Tomita, H. and M. Satoh, 2004: A new dynamical framework of nonhydrostatic global model using the icosahedral grid. *Fluid Dyn. Res.*, **34**, 357-400.

DOI:10.1016/j.fluiddyn.2004.03.003

Tomita, H., 2008: A stretched grid on a sphere by new grid transformation. *J. Meteor. Soc. Japan.*, **86A**, 107-119.

Tsuda, T., Inoue, T., Kato, S., Fukao, S., Fritts, D. C., and VanZandt, T. E., 1989: MST radar observations of a saturated gravity wave spectrum. *Journal of the Atmospheric Sciences*, **46(15)**, 2440-2447.

Tsuda, T., Y. Murayama, M. Yamamoto, S. Kato, and S.Fukao, 1998: Seasonal variation of momentum flux in the mesosphere observed with the MU radar, *Geophys. Res. Lett.*, **17**, 725–728.

Tsutsumi, M., T. Tsuda, T. Nakamura, and S. Fukao, 1994: Temperature fluctuations near the mesopause inferred from meteor observations with the middle and upper atmosphere radar, *Radio Sci*., **29(3)**, 599–610, doi:10.1029/93RS03590.

Tsutsumi, M., K. Sato, T. Sato, M. Kohma, T. Nakamura, K. Nishimura and Y. Tomikawa, 2017: Characteristics of mesosphere echoes over Antarctica obtained using PANSY and MF radars, *SOLA*, in press.

Uchida, J., M. Mori, H. Nakamura, M. Satoh, K. Suzuki, and T. Nakajima, 2016: Error and energy budget analysis of a nonhydrostatic stretched-grid global atmospheric model. *Mon. Wea. Rev.*, **144**, 1423–1447, doi:10.1175/MWR-D-15-0271.1.

Vaughan, G., and R. M. Worthington 2007: Inertia-gravity waves observed by the UK MST radar, *Q. J. R. Meteorol. Soc.*, **133**: (S2) 179–188.

VanZandt, T. E., 1982: A universal spectrum of buoyancy waves in the atmosphere. *Geophysical Research Letters*, **9(5)**, 575-578.

Vincent, R. A., I. M. Reid, 1983: HF Doppler Measurements of Mesospheric Gravity Wave Momentum Fluxes. *J. Atmos. Sci.*, **40**, 1321–1333. doi: 10.1175/1520-0469(1983)040<1321:HDMOMG>2.0.CO;2.

Vincent, R. A., & Fritts, D. C., 1987: A climatology of gravity wave motions in the mesopause region at Adelaide, Australia. *Journal of the atmospheric sciences*, **44(4)**, 748-760.

Walters, D. N., and Coauthors, 2011: The Met Office Unified Model Global Atmosphere 3.0 and JULES Global Land 3.0/3.1 configurations. *Geosci. Model Dev.*, **4**, 919–941.

Walterscheid, R. L., G. G. Sivjee, G. Schubert and R. M. Hamwey, 1986: Large-amplitude semidiurnal temperature variations in the polar mesopause: evidence of a pseudotide. *Nature*, **324**(6095), 347-349.

Wang, L., M. A. Geller, and M. J. Alexander 2005: Spatial and temporal variations of gravity wave parameters. Part I: Intrinsic frequency, wavelength, and vertical propagation direction, *J. Clim.*, **62,** 125**–**142.

Warner, C. D. and McIntyre, M. E., 1996: On the propagation and dissipation of gravity wave spectra through a realistic middle atmosphere, *J. Atmos. Sci*., **53**, 3213–3235.

Watanabe, S., K. Sato, and M. Takahashi, 2006: A general circulation model study of the orographic gravity waves over Antarctica excited by katabatic winds. *J. Geophys. Res.,* **111**, D18104, doi:10.1029/2005JD006851.

Watanabe, S., K. Sato, Y, Kawatani, and M. Takahashi, 2015: Vertical resolution dependence of gravity wave momentum flux simulated by an atmospheric general circulation model, *Geosci. Model Dev.*, **8,** 1637-1644, doi:10.5194/gmd-8-1637-2015.

Williamson, D.L., 1968: Integration of the barotropic vorticity equation on a spherical geodesic grid. *Tellus*, **20**, 642−653.

Wu, D. L. and Waters, J. W., 1996: Satellite observations of atmospheric variances: A possible indication of gravity waves. *Geophysical Research Letters*, **23(24)**, 3631-

3634.

Wu, W.-S., R. J. Purser, and D. F. Parrish, 2002: Three-dimensional variational analysis with spatially inhomogeneous covariances. *Mon. Wea. Rev.*, **130,** 2905–2916.

Wu, Q., Killeen, T. L., Nozawa, S., McEwen, D., Guo, W., & Solomon, S. C.,2003: Observations of mesospheric neutral wind 12-hour wave in the Northern Polar Cap. *Journal of atmospheric and solar-terrestrial physics*, **65**(8), 971-978.

Wu, D. L., Preusse, P., Eckermann, S. D., Jiang, J. H., de la Torre Juarez, M., Coy, L. and Wang, D. Y., 2006: Remote sounding of atmospheric gravity waves with satellite limb and nadir techniques, *Advances in Space Research*, **37(12)**, 2269-2277.

Yamashita, K., S. Miyahara, Y. Miyoshi, K. Kawano, and J. Ninomiya, 2002: Seasonal variation of non-migrating semidiurnal tide in the polar MLT region in a general circulation model, *J. Atmos. Solar-Terr. Phys.*, **64**, 1083–1094.

Yamashita, C., England, S. L., Immel, T. J., & Chang, L. C., 2013: Gravity wave variations during elevated stratopause events using SABER observations. *Journal of Geophysical Research: Atmospheres*, **118(11)**, 5287-5303.

Yasuda, Y., K. Sato, and N. Sugimoto, 2015: A Theoretical Study on the Spontaneous Radiation of Inertia-gravity Waves Using the Renormalization Group Method. Part I: Derivation of the Renormalization Group Equations, *J. Atmos. Sci*., **72**, 957–983, doi:10.1175/JAS-D-13-0370.1

Yasuda, Y., K. Sato, and N. Sugimoto, 2015: A Theoretical Study on the Spontaneous Radiation of Inertia-gravity Waves Using the Renormalization Group Method. Part II: Verification of the Theoretical Equations by Numerical Simulation, *J. Atmos. Sci*., **72**, 984–1009, doi:10.1175/JAS-D-13-0371.1

Yasui, R., K. Sato and M. Tsutsumi, 2016: Seasonal and interannual variation of mesospheric gravity waves based on MF radar observations over 15 years at Syowa Station in the Antarctic., *SOLA*, **12**, 46-50, doi:10.2151/sola.2016-010.

Yoshiki, M., and K. Sato, 2000:A statistical study of gravity waves in the polar regions based on operational radiosonde data, *J. Geophys. Res.*, **105**(D14), 17,995–18,011.

Zhang, F., S. E. Koch, C. A. Davis, and M. L. Kaplan, 2001: Wavelet analysis and the governing dynamics of a large-amplitude mesoscale gravity-wave event along the East Coast of the United States. *Quart. J. Roy. Meteor. Soc.*, **127,** 2209-2245.

Zeller, O., M. Zecha, J. Bremer, R. Latteck, and W. Singer, 2006: Mean characteristics of mesosphere winter echoes at mid- and high-latitudes, *J. Atmos. Sol. Terr. Phys.*, **68**, 1087–1104, doi:10.1016/j.jastp.2006.02.015.